THE UNIVERSITY OF HULL

A SHAPE ANALYSIS APPROACH TO PREDICTION OF BONE STIFFNESS USING FEXI

being the Thesis submitted for the Degree of

Doctor of Philosophy

in the University of Hull

by

Sandhya Pisharody B.E(Comp. Sc.)

October 2007

“It is the theory that decides what we can observe.
If the facts don’t fit the theory, change the facts.”
- Albert Einstein

Abstract

The preferred method of assessing the risk of an osteoporosis related fracture is currently a measure of bone mineral density (BMD) by dual energy X-ray absorptiometry (DXA). However, other factors contribute to the overall risk of fracture, including anatomical geometry and the spatial distribution of bone. Finite element analysis can be performed in both two and three dimensions, and predicts the deformation or induced stress when a load is applied to a structure (such as a bone) of defined material composition and shape. The simulation of a mechanical compression test provides a measure of whole bone stiffness (N mm^{-1}).

A simulation system was developed to study the sensitivity of BMD, 3D and 2D finite element analysis to variations in geometric parameters of a virtual proximal femur model. This study demonstrated that 3D FE and 2D FE (FEXI) were significantly more sensitive to the anatomical shape and composition of the proximal femur than conventional BMD. The simulation approach helped to analyse and understand how variations in geometric parameters affect the stiffness and hence strength of a bone susceptible to osteoporotic fracture.

Originally, the FEXI technique modelled the femur as a thin plate model of an assumed constant depth for finite element analysis (FEA). A better prediction of tissue depth across the bone, based on its geometry, was required to provide a more accurate model for FEA. A shape template was developed for the proximal femur

to provide this information for the 3D FE analysis.

Geometric morphometric techniques were used to procure and analyse shape information from a set of CT scans of excised human femora. Generalized Procrustes Analysis and Thin Plate Splines were employed to analyse the data and generate a shape template for the proximal femur. 2D Offset and Depth maps generated from the training set data were then combined to model the three-dimensional shape of the bone. The template was used to predict the three-dimensional bone shape from a 2D image of the proximal femur procured through a DXA scan. The error in the predicted 3D shape was measured as the difference in predicted and actual depths at each pixel. The mean error in predicted depths was found to be 1.7mm compared to an average bone depth of 34mm.

3D FEXI analysis on the predicted 3D bone along with 2D FEXI for a stance loading condition and BMD measurement were performed based on 2D radiographic projections of the CT scans and compared to bone stiffness results obtained from finite element analysis of the original 3D CT scans. 3D FEXI provided a significantly higher correlation ($R^2 = 0.85$) with conventional CT derived 3D finite element analysis than achieved with both BMD ($R^2 = 0.52$) and 2D FEXI ($R^2 = 0.44$).

Acknowledgements

The research described in this document was a collaborative project between the Department of Computer Science at the University of Hull and the Centre for Metabolic Bone Diseases, Hull and East Yorkshire Hospitals NHS Trust and was jointly funded.

Prof. Christian Langton at the Centre for Metabolic Bone Diseases who pioneered the FEXI (Finite Element analysis of X-ray Images) technique has been an inspirational and supportive supervisor and provided invaluable guidance with the understanding of bone anatomy as well as the FEXI methodology.

Prof. Roger Phillips as the lead supervisor has provided excellent guidance on the approaches and mechanisms to ensure the project progresses smoothly and on schedule.

Dr. Michael Fagan from the Department of Engineering has been very helpful with the understanding of finite element analysis procedures for 2D and 3D FE models using ANSYS. The guidance from Prof. Paul O'Higgins of Hull York Medical School has been invaluable in the understanding of Geometric Morphometric concepts.

I would also like to thank Dr. Joyce Keyak at the University of California for sharing with us her CT datasets of human proximal femurs for the development of the shape template and the results of her mechanical and CT-based finite element analysis studies for 3D-FEXI validation.

Contents

Abstract **i**

Acknowledgements **iii**

1 Introduction **1**

1.1 Hypothesis 2

1.2 Context & Scope 3

1.3 Aims & Objectives 4

1.3.1 Aims 4

1.3.2 Objectives 5

1.4 Overview of thesis content 5

2 Background **7**

2.1 Osteoporosis 7

2.2 Osteoporosis assessment 10

2.3 Measuring Bone Quantity 10

2.3.1 Direct measurement of bone density 11

2.3.2 Dual energy X-ray Absorptiometry (DXA) 12

2.3.3 Quantitative Computed Tomography (QCT) 13

2.3.4 Quantitative Ultrasound (QUS) 13

2.3.5 Clinical interpretation of Bone Mineral Density 15

2.4 Measuring Bone Quality 17
2.4.1 Histomorphometry 17
2.4.2 Markers 18
2.4.3 Mechanical Testing 18
2.4.4 Finite Element Analysis 20

3 The Hypothesis **24**
3.1 Background 24
3.2 The justifications 26
3.2.1 Bone geometry variations 27
3.2.2 FEXI Validation 34
3.3 Summarising the hypothesis 37

4 Simulation Study **39**
4.1 Introduction 39
4.2 System description 40
4.3 Results & Discussion 49
4.4 Conclusions 59

5 Shape Analysis and Reconstruction **60**
5.1 3D Reconstruction Techniques 61
5.1.1 Using Multiple Projections 61
5.1.2 Statistical Shape Analysis 65
5.2 Preliminary analysis 66
5.2.1 Depth prediction using grey levels 66
5.2.2 Regression techniques 67
5.2.3 Morphometrics 75
5.3 Summary 76

6 3D reconstruction from a radiographic image 77

6.1 Overview . . . 77

6.2 Shape Template: The Concept . . . 78

6.3 Methodology . . . 79

6.3.1 Building the bone database . . . 79

6.3.2 2D Mappings . . . 81

6.3.3 Input Registration . . . 83

6.3.4 Thin Plate Splines . . . 88

6.3.5 Applying the template . . . 92

6.4 Results & Discussion . . . 93

7 Shape Atlas Application to FEXI 99

7.1 Introduction . . . 99

7.2 Methodology . . . 101

7.2.1 Conversion of 2D Grey Level into BMD . . . 101

7.2.2 3D FEXI . . . 102

7.2.3 2D FEXI and 2.5D FEXI . . . 103

7.3 Comparison Study . . . 104

7.3.1 Samples . . . 104

7.3.2 Mechanical Test . . . 105

7.3.3 3D FEA . . . 106

7.3.4 FEXI implementation . . . 107

7.4 Results & Discussion . . . 109

8 Conclusions 114

8.1 Summary . . . 114

8.2 Limitations & Future Work . . . 116

Appendices **120**

A. Additional FEXI Modules **121**

A.1 Femur contour extraction from hip radiograph 121

A.2 Improved BMD assessment 122

A.3 Fall loading scenario 124

B. Glossary **125**

References **128**

Publications **149**

List of Figures

2.1 Cross-section of the proximal end of a femur model 8
2.2 Normal bone 9
2.3 Osteoporotic bone 9
2.4 A DXA system 12
2.5 QUS device 14
2.6 FEXI Mechanical test setup 23

3.1 PCA scree plot 28
3.2 PCA scatter plot 29
3.3 PCA biplot 31
3.4 Plot of PLS scores 33
3.5 FEXI correlation plot 36

4.1 Virtual System Overview 41
4.2 Virtual Femur Design 42
4.3 Virtual femur 43
4.4 3D FEA element 44
4.5 Simulated radiographic image 45
4.6 2D FEA element 46
4.7 FE models 47
4.8 Displacement plots for 2D FEXI & 3D FEA 47

4.9 Plot of aBMD & FE analysis with varying trabecular density 50
4.10 Plot of aBMD & FE analysis with varying cortical shell thickness . . 50
4.11 Plot of aBMD & FE analysis with varying neck length 51
4.12 Plot of aBMD & FE analysis with varying neck width 52
4.13 Plot of aBMD & FE analysis with varying neck-shaft angle 52
4.14 Plot of aBMD & FE analysis with varying head radius 53
4.15 Plot of aBMD & FE analysis with varying neck anteversion angle . . 54
4.16 Sensitivity of modes 55
4.17 Relative sensitivity to parameter variations analysed separately for aBMD, 2D-FEXI & 3D-FEA 56
4.18 Relative sensitivity to parameter variations, analysed with all measurement and geometric parameters pooled together 57

5.1 Pelvic radiograph 67
5.2 Regression similarity measure 70
5.3 Multivariate regression similarities 72
5.4 NIPALS regression similarities 74

6.1 The shape template concept 79
6.2 Overview of shape template application 80
6.3 Offset and Depth maps 82
6.4 Offset and depth mapping 82
6.5 Landmarks on a femur radiograph 84
6.6 Input and GPA-aligned landmarks 87
6.7 Thin Plate Spline sample 89
6.8 3D grid formed by merging offset and depth maps 91
6.9 Template offset and depth maps 92
6.10 Overview of training template creation 93
6.11 Overview of the transformation process 94

6.12 2D similarity 95
6.13 Offset and depth error maps 96
6.14 Original (light) and Predicted (dark) bones 97

7.1 The mechanical test setup 105
7.2 The 'Stance' loading condition 108
7.3 Displacement plot for 3D FEXI in stance loading 109
7.4 FEXI and BMD correlation with 3D FEA stiffness 110
7.5 FEXI, 3D FEA and BMD correlation with mechanical strength . . . 111

A.1 The contour extraction process 122
A.2 BMD regions 123
A.3 BMD regression 123
A.4 The 'Fall' loading condition 124

List of Tables

2.1 WHO-defined criteria for diagnosis of Osteoporosis 15

3.1 Eigenvalues and % variances for the PCs 30
3.2 Singular values and % variances for the SAs 33

4.1 Proximal femur model parameters 43
4.2 Relative sensitivity of parameters - Analysed separately 56
4.3 Relative sensitivity of parameters - Pooled Analysis 57

6.1 Mean and standard deviation for depth and offset errors 96

B.1 Glossary 125

Chapter 1

Introduction

Osteoporosis is a wide-spread medical condition that mostly affects the elderly and is characterized by bone fragility. It affects the quality of life for the patient as well as being a major financial burden for national health authorities (National Institute of Health, 2003). According to the International Osteoporosis Foundation (International Osteoporosis Foundation, 2006), osteoporosis-related fractures affect up to one in three women and one in five men over the age of 50 worldwide. The costs for the health services in the EU were estimated to total up to approximately 3 billion euros annually.

Bone mineral density (BMD) assessment by dual-energy x-ray absorptiometry (DXA) scans is currently the most widely used technique for osteoporosis assessment. The bone density value quantifies the bone mass at the particular measurement site. However, osteoporosis is, primarily, a decrease in bone strength. Bone mass is the most significant component in bone strength, but not the only one. It does not reflect the distribution of bone trabeculae, which represent the internal bone

architecture. Various studies have shown the importance of trabecular architecture on bone strength (Kleerekoper et al., 1985; Siffert et al., 1996). As the WHO definition of osteoporosis states (Consensus Development Conference, 1991),

> Osteoporosis is a systemic skeletal disease characterized by low bone mass and micro architectural deterioration of bone tissue, with a consequent increase in bone fragility and susceptibility to fracture.

Thus, the assessment of bone quality, and hence structure, along with bone density is required to better predict a risk of osteoporotic fracture.

1.1 Hypothesis

The finite element method is a widely used engineering technique used for analysing complex structural problems. It was first used in the study of bone structural mechanics by Brekelmans et al. back in 1972. Finite element analysis can predict the deformation or induced stress when a load is applied to a structure (such as a bone) of defined shape and material composition (Pao, 1986). A finite element approach to assess bone stiffness will provide a measure of the structural quality of the bone.

Computed Tomography (CT) scans have been used to build 3D models of bones for finite element analysis (Cody et al., 1999; Keyak, 2001; Lotz et al., 1991). However, because of the high costs and high doses of radiation exposure, CT scans are not routinely used in clinical assessment. 2D radiographic imaging such as DXA, on

the other hand, are more readily available. Finite Element analysis of X-ray Images (FEXI) (Langton et al., 2004, 2005) uses a radiographic image for simulation of a mechanical compression test to provide a measure of whole bone stiffness (N mm^{-1}). The FEXI technique models the femur as a thin plate finite element model of an assumed constant depth. A better prediction of tissue depth across the bone, based on its 2D geometry, should provide a more accurate 3D model for FEA, and hence a better estimation of bone strength. This thesis proposes that a shape atlas for the proximal femur can be used to provide 3D shape information for a bone from a simple 2D radiograph.

A shape atlas may be considered as a set of rules and relationships defining the spatial characteristics of an object. The shape atlas for the proximal femur may be defined by studying a set of real bones and identifying relationships between various landmarks identified along the surface of the bone. These relationships will make it possible to represent the shape of a bone in 3D based upon its 2D planar projection (radiograph). A predicted 3D model of the femur will be reconstructed from a single 2D radiograph using a shape atlas for the proximal femur.

1.2 Context & Scope

The research described in this thesis addresses questions regarding performance of FEXI with two- and three-dimensional bone images as well as techniques for reconstruction of the three-dimensional shape of a bone given a single two-dimensional projection (such as a radiograph). It also looks at the performance of FEXI with these reconstructed predicted 3D femur models.

The sensitivity of the FEXI approach for measuring bone stiffness to variations in the femur geometry was studied using a simulated bone model. This tested the FEXI hypothesis of being significantly sensitive to overall bone architecture as well as bone mineral density. The measure of FEXI-derived stiffness was compared to bone strength results from bone mineral density (BMD) analysis using DXA scans. BMD analysis is currently considered the gold-standard for bone strength estimation and any new technique for bone strength assessment must be at least as accurate as BMD. The performance of FEXI with 2D radiograph images was also compared to finite element analysis using 3D bone models.

Techniques (described in Chapter 5) for reconstruction of 3D shape from 2D images were studied to assess their advantages and drawbacks with respect to the current research problem, i.e., reconstruction of bone shape from a single radiograph.

1.3 Aims & Objectives

1.3.1 Aims

1. To investigate the sensitivity of Finite Element analysis of X-ray Images (FEXI) to variations in the anatomical parameters of the proximal femur.

2. To investigate the use of a shape atlas for improving prediction of bone stiffness using FEXI.

1.3.2 Objectives

1. Analyse the sensitivity of FEXI and BMD to changes in anatomical parameters using simulated femur models.

2. Analyse changes in the 3D shape of the proximal femur and identify the main sites of variation.

3. Study available techniques for 3D reconstruction of shape from 2D projections. Analyse advantages and drawbacks of the techniques with respect to current research problem and identify the technique most suited for the current research problem.

4. Use chosen shape analysis method to build a Shape Atlas for femora using shape information gathered from CT scan images. Validate the Shape Atlas using radiographic images to obtain predicted 3D femur models.

5. Analyse performance of FEXI with predicted 3D femora with respect to BMD, 2D FEXI on radiographs and mechanical bone strength analysis.

1.4 Overview of thesis content

The relevant background for the research is discussed in Chapter 2. This chapter discusses various osteoporosis assessment techniques and describes the FEXI concept and methodology.

The research hypothesis and justification are submitted in Chapter 3. This chapter attempts to provide an overall picture of the various components of this research

and how they tie in with each other.

Chapter 4 gives a detailed description of the simulation system used to test the sensitivity of FEXI to femur geometry. It discusses the development of a virtual femur with variable geometric and bone density parameters as well as the sensitivity analysis for BMD and FEXI-derived stiffness with these varying parameters.

The various approaches for shape analysis are considered in Chapter 5, with details of the options tested for the development of the femoral shape template.

The concept of a shape atlas for bones and the application of shape analysis techniques for building a shape template for the human proximal femur is examined in Chapter 6. This chapter also examines the choice of methodology for building a shape model for the proximal femur and takes a closer look at the use of geometric morphometrics for shape reconstruction.

Chapter 7 describes the application of the shape atlas for FEXI analysis with results from these analysis for a CT dataset for which strength had been computed both mechanically and using finite element analysis.

An analysis and discussion of these results along with limitations of the proposed technique are presented in Chapter 8. This chapter concludes this thesis by giving an overview of the research findings and the direction of future work.

Chapter 2

Background

2.1 Osteoporosis

Osteoporosis literally means 'porous bones' and is a skeletal disease characterised by a progressive weakening of bone. Continuous loss of bone during life is the main causes of osteoporosis. Lower peak bone mass, gender, nutrition, lifestyle, medications and physical characteristics of the bone are among other risk factors contributing towards osteoporosis (Cowin, 2001).

Bone is a living tissue made up of a thick outer shell called the cortex and an inner mesh-like structure called the cancellous bone (see Figure 2.1). The cancellous bone is made up of a network of collagen fibres, calcium salts and other minerals interspersed with bone marrow (Cowin, 2001). The shaft of a long bone, such as the femur, typically consists of a thick cylinder of cortical bone, known as the diaphysis. The head and the trochanter on the other hand, have a thin cortical outer shell enclosing a region of cancellous bone.

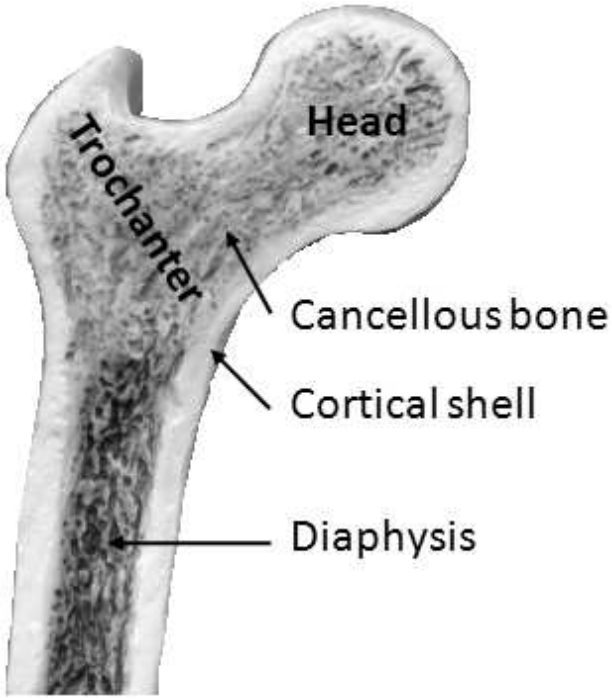

Figure 2.1: Cross-section of the proximal end of a femur model showing cortical and cancellous bone and the main sections of the bone - the shaft (diaphysis), trochanter (metaphysis) and the head (epiphysis)

Bones undergo continual remodelling to maintain the geometry and internal structure of the bone. Two distinct bone cell types, osteoblasts and osteoclasts, govern the bone remodelling process (Gray, 2000). The osteoclasts are bone-resorbing agents which excavate a resorption cavity on the bone surface. The osteoblasts are bone-building agents which balance this deterioration process by filling the resorbed cavities with new bone. This remodelling process is responsible for maintaining the bone geometry and inner architecture. Osteoclast activity exceeds bone resorption by osteoblasts during growth, peaks in young adult life and starts to decline after about 30.5 years and by the age of 70, bone mass dwindles to less than 70% of the young adult mass (Cowin, 2001).

A negative balance between the bone rebuilding and bone resorption processes causes a gradual thinning of the internal bone architecture, thereby leading to a loss of bone strength. Figures 2.2 and 2.3 show the difference in the trabecular architecture in case of a normal and osteoporotic subject respectively.

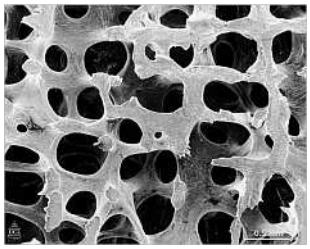

Figure 2.2: Low-power scanning electron microscope image of normal bone architecture in the 3rd lumbar vertebra of a 30 year old woman marrow and other cells have been removed to reveal thick, interconnected plates of bone. *By kind permission of Tim Arnett, University College London, UK*

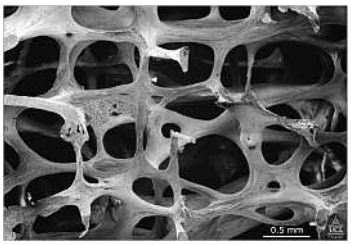

Figure 2.3: Low-power scanning electron microscope image of osteoporotic bone architecture in the 3rd lumbar vertebra of a 71 year old woman marrow and other cells have been removed to reveal eroded, fragile rods of bone. *By kind permission of Tim Arnett, University College London, UK*

Both cortical and cancellous bone are affected by osteoporosis. Trabecular bone is found in high percentages in the hip, spine and wrist and is more vulnerable because it is more metabolically active and has a higher turnover rate. Men as well as women suffer from osteoporosis. Early detection of bone loss is critical in preventing osteoporotic fractures.

2.2 Osteoporosis assessment

The gold standard measurement of bone strength and hence fracture risk is a destructive test, such as a mechanical compressive testing of either a sample of the bone or the whole bone. Bone mineral content (BMC) and density (BMD) measurements for a defined volume (volumetric, gcm^{-3}) or projected area (areal, gcm^{-2}) are often considered as surrogate physical measurement techniques for predicting mechanical integrity. Bone densitometry measurements are generally accepted as accounting for approximately 60-70% of bone strength with 'bone quality', typically bone geometry and cancellous structure, explaining the remainder (Langton and Njeh, 2004).

2.3 Measuring Bone Quantity

Currently, there is no accurate non-invasive measure of overall bone strength. However, the most commonly used measurement to diagnose osteoporosis is based on assessment of Bone Mineral Density (BMD). Various researchers have observed significant correlations for bone mineral density with fracture-risk (Hui et al., 1988; Wasnich et al., 1989; Cummings et al., 1993) and with failure load (Beck et al., 1998; Bouxsein et al., 1999). Cummings et al. (2002) gives a detailed review of the clinical use of bone densitometry using the various techniques available and finds bone mineral density to be a good indicator of bone strength for routine clinical use. Some common BMD measurement methods are described below.

2.3.1 Direct measurement of bone density

One of the earliest methods for measuring bone density was based on Archimedes' law of buoyancy (Robinson and Elliott, 1957; Dickerson, 1962; Gong et al., 1964; Keenan et al., 1997). Using this principle, the density of a bone sample was computed from the weights of the bone in dry and submerged states as (Cowin, 2001):

$$\rho_{bone} = \rho_{fluid}\frac{W}{W-S} \tag{2.1}$$

where W and S are the dry and submerged weights respectively and ρ_{fluid} is the density of the fluid in which the bone is submerged. Distilled water or pure ethyl alcohol may be used as the fluid for submerging the bone sample. The density value as measured by this technique falls in the range of 1.8 - 2.3 gcm^{-3} and is the mineralized bone tissue (i.e. material) density, calculated as dry weight of the specimen divided by the volume of bone matrix excluding marrow space (Ding, 2000).

Such a measurement of bone density, however, cannot be performed in-vivo. Imaging modalities such as X-ray absorptiometry, computed tomography and ultrasound have hence been proposed to estimate bone density values. A point to be noted here is that the bone density as measured from these imaging modalities is the apparent (i.e. structural) density (Ding, 2000), i.e. the density of the mineralized bone matrix and is calculated as dry weight of the specimen divided by the volume of specimen, including the marrow space.

2.3.2 Dual energy X-ray Absorptiometry (DXA)

Dual energy X-ray Absorptiometry (DXA) is the most commonly used technique for BMD measurement. Routine X-ray images can only verify advanced bone loss and bone fractures. DXA scans produce high-resolution images of the targeted site, such as the hip, spine, or wrist. The fundamental principle behind DXA is the measurement of the transmission of X-rays of two different photon energies through the body (Genant et al., 1996). Since the attenuation coefficient depends on atomic number and photon energy, measurement of the transmission factors at two energies enables the 'areal' densities (i.e. the mass (g) per unit projected area (cm^2)) of two different types of tissue to be inferred. In DXA scans these are taken to be bone mineral and soft tissue respectively. The BMD measurements are used by the physician to assess osteoporotic fracture risk. The radiation levels for DXA are low and the scan takes less than 5 minutes. This testing also helps to monitor the effectiveness of treatment.

Figure 2.4: A DXA system

2.3.3 Quantitative Computed Tomography (QCT)

Computed Tomography (CT) scanning uses X-rays to generate cross-sectional slice-by-slice views of body parts. For this, a large series of X-ray slice data is obtained about a single axis of rotation around the object. Data scans are progressively generated using X-ray sensors positioned opposite to the X-ray source. The numerical value assigned to each pixel in a CT slice is based on the differential absorption of ionizing radiation by calcified tissue and is expressed in Hounsfield Units (HU) (Jackson, 2004).

Quantitative computed tomography (QCT) utilises a calibration phantom to convert Hounsfield number into a measure of volumetric bone density (gcm^{-3}) of the hip and spine. The potential advantage of QCT is that it measures volumetric rather than areal density. Also, the bone density of cancellous bone alone may be measured, separate from the cortical shell, by selecting a region of interest (ROI). Clinical QCT offers quite high spatial resolution of typically 0.15 mm compared to approximately 1mm for DXA. However, the radiation dose to a patient subjected to QCT is significantly higher (25 - 360 μSv) than in DXA (0.08 - 4.6 μSv) (Njeh et al., 1999).

2.3.4 Quantitative Ultrasound (QUS)

Ultrasound velocity is related to the elasticity and density of cancellous bone, whereas BUA is related to the density and structure of cancellous bone. As the structural variability decreases, the relationship between BUA and density increases. Clinical studies have shown that QUS parameters are sensitive to age-

related changes, may discriminate osteoporotic subjects and exhibit a prospective fracture risk prediction comparable to axial DXA. QUS offers the potential to serve 2 major clinical roles, viz., to predict fracture risk independent of established bone densitometry or to be a case-finding referral tool for subsequent conventional densitometry.

The clinical application of Quantitative ultrasound (QUS) for the assessment of osteoporosis was first demonstrated in Hull by Dr Chris Langton via the measurement of broadband ultrasound attenuation (BUA) at the calcaneus (Langton, 1984). QUS has been scientifically validated both in terms of fundamental in-vitro and clinical in-vivo studies. Figure 2.5 is an image of a portable BUA measurement device. Due

Figure 2.5: The McCue CUBAclinical QUS device for measuring BUA at the human calcaneous (heel)

to technical difficulties, Quantitative Ultrasound measurements cannot routinely be performed at the common anatomical sites affected by osteoporosis (spine, hip and wrist). However, it has been clinically demonstrated that ultrasound measurement of the calcaneous (heel) provides an accurate indication of osteoporosis fracture risk, particularly for hip fracture (Njeh et al., 1997b; He et al., 2000; Damilakis et al., 2004).

2.3.5 Clinical interpretation of Bone Mineral Density

In 1994, the World Health Organization (WHO) selected BMD measurements to establish criteria for the diagnosis of osteoporosis. BMD measurements are specified in terms of T-score and Z-score (Fogelman et al., 2002):

- T-score: standard deviation compared to average BMD value for young healthy adults.
- Z-score: standard deviation compared to average BMD value for age- and gender-matched young healthy adults.

The T-score is calculated by taking the relative standard deviation of the patient's measured BMD from the mean BMD of healthy young adults at the age of peak bone mass, matched for gender and ethnic group, with respect to the standard deviation for young adult population:

$$T - score = \frac{(Measured\ BMD\ -\ Young\ adult\ mean\ BMD)}{(Young\ adult\ standard\ deviation)} \tag{2.2}$$

A T-score result indicates the difference between the patient's BMD and the ideal peak bone mass achieved by a young adult. Changes in T-score reflect in fracture-risk. The WHO defined criteria for diagnosis of osteoporosis (WHO Study Group, 1994) is summarized in Table 2.1.

Category	T-score	Risk of fracture
Normal	$T - score \geq -1$	Low
Osteopenic	$-1 > T - score > -2.5$	Intermediate
Osteoporotic	$T - score \leq -2.5$	High

Table 2.1: WHO-defined criteria for diagnosis of Osteoporosis

A patient is considered osteoporotic if the areal Bone Mineral Density (aBMD) or areal Bone Mineral Content (aBMC) is over 2.5 standard deviations below the mean. Osteopenia indicates increased fracture-risk and risk of developing osteoporosis in the future. Presence of fractures lead to a classification of 'severe osteoporosis'. The T-score is a linear transformation of the bone density, and depends on the mean and standard deviation at peak bone mass.

An alternative BMD measurement index to the T-score is the Z-score which is also expressed in units of the population standard deviation (SD) and is calculated by comparing the standard deviation of the patient's BMD from the mean BMD for a healthy normal adult matched for age, gender and ethnic origin, to the standard deviation for a similarly matched healthy normal adult.

$$Z - score = \frac{(Measured\ BMD\ -\ Reference\ mean\ BMD)}{(Reference\ standard\ deviation)} \tag{2.3}$$

Z-scores are not as widely used as T-scores, but they provide a useful means of expressing a patient's osteoporotic fracture-risk with respect to their peers. The Z-score may be computed from a T-score by subtracting the T-score of an age-, gender-, race- and skeletal site-matched reference from the T-score of the patient.

A point to note is that these bone densitometry measures reflect the status of the scanned bone at a particular time. Repeat BMD measurements at regular intervals of one or two years may be required to assess the changes in bone density over time.

2.4 Measuring Bone Quality

Put simply, the bone density value is the ratio of bone mass to bone volume. The bone density value, therefore, does not reflect the condition of the bone structure in terms of the distribution of bone trabeculae. However, primarily, osteoporosis is a problem of the bone strength which in turn depends on its structural integrity. Hence along with quantitative measurements of bone density, qualitative measures of bone structure are required for an accurate assessment of osteoporotic fragility fracture risk.

2.4.1 Histomorphometry

Histomorphometry is a quantitative study of the shape and structure of body tissue, in this case of bone. It is used to assess the condition of the bone structure by measuring its porosity and trabecular connectivity. Stereological point-counting techniques on cross-sections of bone under a microscope have been used to express porosity in terms of percentage of total area or volume of bone (Vesterby, 1993). This however, is an in-vitro approach.

The node-strut analysis technique (Ohkubo, 2002) proposed a means of analysing the continuity of trabecular structure in a sample of bone tissue in-vivo using morphological operations performed on a radiographic image of the bone. The condition of the bone tissue structure is expressed as a quantitative index value for osteoporosis assessment.

2.4.2 Markers

Parfitt (1993); Reeve et al. (1993) have found independent effects of bone turnover on fracture risk based on the loss of trabecular integrity due to increase in bone resorption. Bone remodelling can be assessed by the measurement of surrogate markers of bone turnover in the blood or urine. The level of these markers may identify changes in bone remodelling within a relatively short time interval (several days to months) before changes in BMD can be detected.

Levels of biochemical markers of bone metabolism have been found to correlate with rates of bone remodelling as measured by histomorphometry and also with lower and accelerated bone loss (Chesnut et al., 1997; Bauer et al., 2001). Higher levels of bone markers have been associated with increased risk of fracture after adjustment for bone mass (Garnero et al., 1996, 2000; Akesson et al., 1995). Typically the main use of biochemical markers is in assessing response to treatments in osteoporosis rather than diagnosis of osteoporosis (Looker et al., 2000).

2.4.3 Mechanical Testing

Seeman (2003) referred to bone fragility as a '*problem in biomechanics*'. He described the contrasting features of the bone's material and structural properties requiring the bone to resist bending during load bearing and to deform during impact to avoid fracture. Bone strength may thus be computed using the biomechanical characteristics of the bone, typically by studying the relationship between an applied load and the resulting structural displacement. Stiffness is determined from the slope of the elastic region of the load-displacement curve (Sato et al., 1999).

The basic mechanical test setup consists of a mechanical testing machine and strain/ displacement measurement transducers. Tensile or compressive testing may be used to measure bone properties. Tensile tests are typically used for relatively large bone specimens and strain is measured across the midsection of the specimen. Compressive tests, however, better simulate in-vivo loading conditions for some skeletal regions such as the hip joint and the vertebrae.

Femoral neck fractures constitute up to 50% of osteoporosis-related fractures (Hosiet et al., 1987). Biomechanics at the femoral neck site are, hence, useful in assessing osteoporotic fracture-risk among patients. There are two loading scenarios commonly used to measure femoral neck strength. The first referred to as 'stance condition', simulates the loading of the bone for a person in the standing position. The other loading scenario, referred to as 'fall condition' simulates a person falling sideways on their hip.

Keyak et al. (2005) used a stance loading scenario with the femoral shaft axis aligned at 20^o to the coronal plane with an axial load applied at the top of the femoral head. In the fall loading case, the femur was rotated so as to rest on its greater trochanter with the shaft oriented at an angle of 30^o to the ground. A femoral head anteversion of 15^o was also applied to simulate realistic loading conditions of a fall. The orientation angles used in these loading scenarios have varied. Dalen et al. (1976) applied the load parallel to the shaft axis in the stance configuration in his study to test correlation of bone mineral levels with fracture risk. Bouxsein et al. (1995) used a shaft orientation of 10^o for mechanical testing in the fall configuration for their test of correlation among femoral bone properties and fracture risk. The shaft was fixed distally but free to rotate and slide.

Mechanical testing, however, is a strictly ex-vivo technique for estimating bone strength. Finite element models provide a way of simulating mechanical testing using models generated using scans of the bone in-vivo.

2.4.4 Finite Element Analysis

Finite element analysis (FEA) is an effective and widely used computer-based simulation technique for modelling mechanical loading of various engineering structures, providing predictions of displacement and induced stress distribution due to the applied load.

In this technique, the object or system is represented by a geometrically similar model consisting of multiple, linked, simplified representations of discrete regions, i.e., finite elements (Pao, 1986). The behaviour of an individual element can be described with a relatively simple set of equations. These elements are joined together at nodes along edges. Complex models can be created as an assembly of elements to which loads and restraints may be applied. The equations describing the behaviours of the individual elements are joined into an extremely large set of simultaneous equations that describe the behaviour of the whole structure. The deformation of the nodes is calculated by solving inter-related simultaneous equations. Computer analysis of the model gives nodal displacements corresponding to the applied load. The strength of a bone depends on its material composition and structural integrity (Currey, 2002). Finite element analysis of a bone would therefore be dependent on the Young's modulus (a function of density) of each element, the overall shape of the bone (length and angle of neck, size and anteversion of head) and the internal structure of the bone.

Finite element analysis (FEA) of 3D femur models obtained from quantitative CT (QCT) has been utilised to assess the strength of the femur (Lotz et al., 1991; Cody et al., 1999; Keyak, 2001; Keyak et al., 2005), being inherently dependent upon both density and geometric parameters. By applying random uncertainties in the geometry, density and mechanical properties of the femur within a Monte Carlo method sensitivity analysis, Taddei have validated the robustness of mechanical behaviour prediction based upon finite element analysis models derived from computed tomography data (Taddei et al., 2006). However, because of the high costs and high doses of radiation exposure, CT scans are not routinely used in clinical assessment. DXA, on the other hand, is relatively easier to obtain and hence a finite element analysis technique using 2D radiographic images as input might prove more feasible and practical for routine analysis.

Finite Element Analysis of X-ray Images (FEXI)

Using a methodology fundamentally similar to Testi et al. (2004), 2D-FEXI (Finite Element Analysis of X-ray Images) (Langton et al., 2004, 2005) is a recently developed technique which uses a radiographic image of a bone to create a 2D plane stress model for finite element analysis. Simulation of a compressive mechanical loading resulting from a sideways fall to the ground is used to compute the stiffness of the bone. Stiffness (Nmm^{-1}) describes the resistance to deformation, being a standard and reliable experimental mechanical compression parameter, derived prior to the yield point and fracture of a sample under test. On the basis that stiffness is widely accepted to be a reliable surrogate for bone strength (Lochmuller et al., 1998), it was assumed that FEXI derived stiffness could serve as a reliable non-destructive, non-invasive surrogate for bone strength. Conventional bone densitometry by DXA

is similarly performed on the assumption that BMD is a reliable surrogate for bone strength. It should be noted however that the risk of a subject suffering an osteoporotic fracture, such as of the hip, is determined by factors in addition to material and geometric parameters of the proximal femur, these include the risk of falling along with the weight and soft-tissue protection of the subject.

FEXI Methodology

1. A DXA hip scan is performed, from which the image is exported as an 8-bit greyscale image. A previous DXA scan of an aluminium step-wedge is used to convert each pixel grey level into BMD via a derived regression equation.

2. The volumetric density for each pixel is computed by dividing the BMD by an assumed constant tissue depth of 25 mm. A Young's modulus is then attributed to each pixel using published regression data (Keyak et al. (2005)).

3. The proximal femur is segmented using a semi-automatic contour detection program thereby deleting adjacent surrounding tissue and other bones. It should be noted however that the acetabulum will still be present overlying the femoral head. The image is then rotated such that the femoral shaft is aligned at a defined angle.

4. Simulated support and loading platens to facilitate even loading across the bone surfaces are added to the bone image at the greater trochanter and femoral head respectively. The lower support platen is restrained in both vertical and horizontal directions; the upper loading platen is restrained in the horizontal direction only, thereby allowing vertical displacement. A known load is applied along the top of the loading platen.

5. A thin-plate FE analysis model is generated for the platened bone image thus simulating a mechanical compression test, shown in Figure 2.6. The stiffness (Nmm^{-1}) of the bone is calculated by dividing the applied load by the recorded displacement of the upper loading platen.

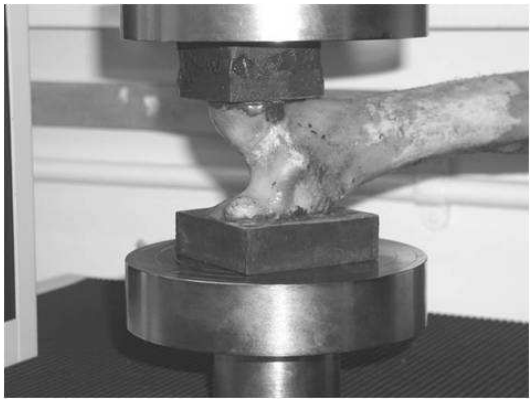

Figure 2.6: Mechanical test setup showing a compressive loading of a porcine femur

There are however, a number of fundamental limitations associated with the original 2D FEXI approach; no account is made for the variable thickness across the proximal femur, and it is not possible to simulate anteversion of the femoral neck as occurs when a subject falls on their hip.

The hypothesis behind this thesis was that the development and application of a Shape Model of the proximal femur would overcome these limitations, whereby the size and shape of a 2D DXA image of the proximal femur would be converted into a subject-specific and versatile 3D finite element model (3D FEXI) that is more realistic and could serve as a more accurate surrogate of bone strength than either BMD or 2D FEXI. This hypothesis is developed further in the following chapter.

Chapter 3

The Hypothesis

3.1 Background

As mentioned in the previous chapter, the most common clinical measurement for assessing bone strength associated with osteoporosis is a measure of bone mineral density by dual energy X-ray absorptiometry (DXA). Areal bone mineral density (aBMD) is utilised as a surrogate for bone strength, explaining between 70% and 85% of its variance (Dalen et al., 1976). We know however that other factors contribute to the overall risk of fracture including anatomical geometry and the spatial distribution of bone. Recent osteoporosis fracture-risk studies have been looking at methods to quantify bone quality along with bone quantity. Bone quality describes factors such as the anatomical geometry, rate of bone remodelling and the spatial distribution of bone.

Muller et al. (2003) compared DXA of the radius and phalanges, peripheralQCT of the 4% and 20% distal sites of the radius, radiogrammetry of the forearm and

quantitative ultrasound of the radius techniques to assess which would best predict failure load of the distal radius. It was seen that bone mineral content measures were generally better predictors of failure load ($r^2 = 0.53 - 0.85$) than the corresponding bone mineral density values ($r^2 = 0.22 - 0.69$) measured by either pQCT or DXA. QUS and radiogrammetry were found to be moderate predictors of fracture load (r^2=0.49 and 0.54 respectively). Measures of radial geometry at the 20% site by pQCT improved failure load prediction using bone mineral content by DXA and pQCT by up to 9%. Addition of porosity and trabecular connectivity indices were not found to significantly add to the prediction by the BMC- geometry combination.

Several studies have investigated the effects of femur geometry on bone strength and fracture risk. In 2003, 3D dual-energy x-ray absorptiometry (DXA) scan images were used by Armand et al. (2003) to study the geometry of the proximal femur and its effects on femoral neck strength. Hip axis length has been suggested to be a predictor of fracture risk by some (Bergot et al., 2002; Faulkner et al., 1993; Gnudi et al., 1999; Peacock et al., 1995) while others (Alonso et al., 2000; Calis et al., 2004; Michelotti and Clark, 1999; Partanen et al., 2001) have found no significant relationship. For femoral neck-shaft angle, there is both positive (Alonso et al., 2000; Calis et al., 2004; Gnudi et al., 1999; Partanen et al., 2001; Pulkkinen et al., 2004) and negative (Bergot et al., 2002; Faulkner et al., 1993) evidence for its predictive value. Cortical thickness (Calis et al., 2004; Partanen et al., 2001; Pulkkinen et al., 2004), femoral head diameter (Calis et al., 2004; Michelotti and Clark, 1999; Partanen et al., 2001), and anteversion (Cheng et al., 1997) are among the various other femoral geometric parameters measured and studied to identify associations with fracture risk. Pulkkinen et al. (2004) has suggested using a combination of several of these factors within a multiple linear regression model to predict fracture risk. The clinical fracture prediction performance of geometric parameters has also

been studied (Gluer et al., 1994; Karlsson et al., 1996). El-Kaissi et al. (2005) found alteration in hip geometry associated with fracture risk, with geometric characteristics like femoral neck width, shaft width, neck axis length and hip axis length to be significantly greater in hip fracture patients compared to healthy controls. Testi et al. (2004) used a statistical classifier on a combination of factors including BMD, femoral neck strain from a finite element analysis and patient-specific information, to be used as a predictor of fracture-risk. Other approaches have also been developed to supplement aBMD for the accurate prediction of bone strength including hip strength analysis-derived compressive stress values for falls on the greater trochanter (Crabtree et al., 2002) and active shape modelling to quantify femoral shape and discriminate between healthy and fracture-prone bones (Gregory et al., 2004).

3.2 The justifications

The basis for this research was that three-dimensional finite element analysis of a bone would provide a better prediction of bone stiffness compared to the finite element compressive stress analysis of a bone modelled as a 2D thin plate. Also, the bone for this 3D analysis would be predicted from a two-dimensional radiographic image under the assumption that the shape of the proximal human femur can be templated. This shape template would then be used to reconstruct the missing dimension in the input image and hence obtain a 3D bone model for finite element analysis.

The above described arguments were validated to ensure a good foundation for the research. The following subsections describe the methods used for the tests along

with their outcomes.

3.2.1 Bone geometry variations

The idea behind this study was to obtain a statistical analysis of the variations in the femoral geometry. There were two components to this analysis. The first, to determine the sites of geometric variation and the second, to determine the covariance between variations in bone length and breadth and variations in bone depth.

The sites of variation

Geometric variation was studied in a set of 11 excised human proximal femora using Principal Components Analysis (PCA). The geometric parameters considered were: shaft width, shaft depth, greater-trochanter width, greater-trochanter depth, shaft-head distance, head diameter, neck-axis length, neck width, neck depth and the neck-shaft angle. All measurements were performed using 0.05mm precision callipers. The variables were standardized to zero-mean and unit variance before the analysis.

Principal Component Analysis (PCA) is a way of identifying patterns in a given set of data and highlighting the similarities and differences within that set. For a given shape space where each shape is represented by a series of points, there exists some degree of inter-point correlation between shapes. If not, either the set does not contain any variations, or the points are totally random and do not represent

any landmarks. Principal Components Analysis uses this correlation between points to generate a shape representation with a reduced dimensionality. PCA transforms the data expressing the patterns between the original variables using a new set of variables called Principal Components (PCs). These principal components are linear combinations of the original variables but orthogonal to each other. Since there are typically fewer PCs than variables, it is easier to analyse a dataset using these PCs.

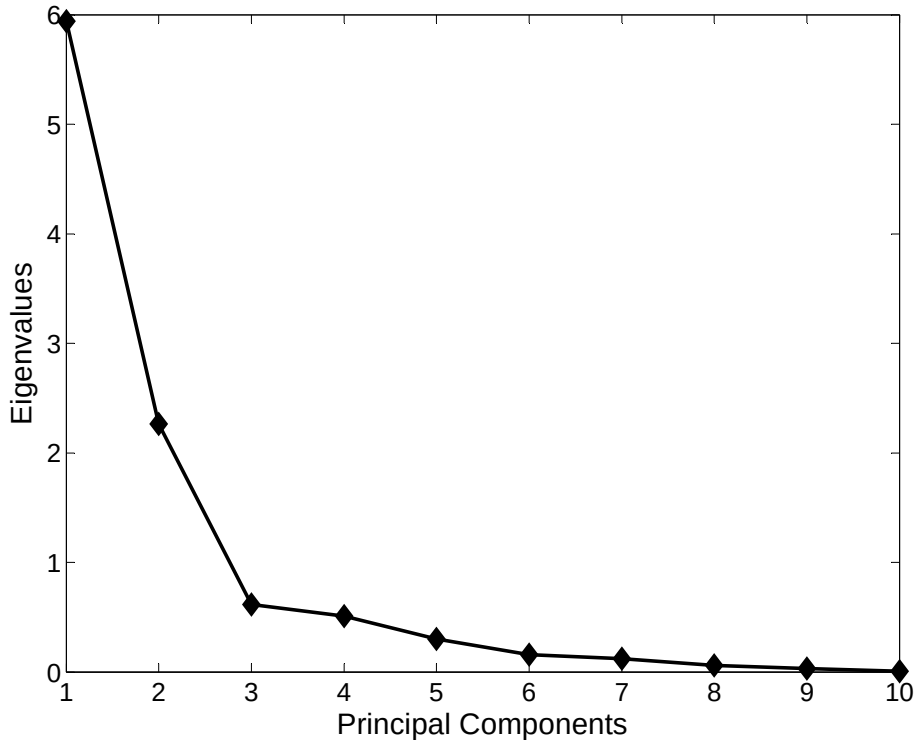

Figure 3.1: PCA scree plot

A scree plot is used to show the sorted eigenvalues, from large to small, as a function of the eigenvalue index. The above figure (Figure 3.1) shows a scree plot of the proportion of variance described by each PC for the dataset of 11 femora. From the scree plot and the cumulative percentage variances in Table 3.1, it was observed that the first three PCs together accounted for about 88% of the total

variance in geometry and hence considered to be the components with any biological significance. The scatter plot of the first 2 PCs for the above considered example (Figure 3.2) shows the difference in the range of variation described by these. PC1 describes a much larger proportion of variance between shapes compared to PC2.

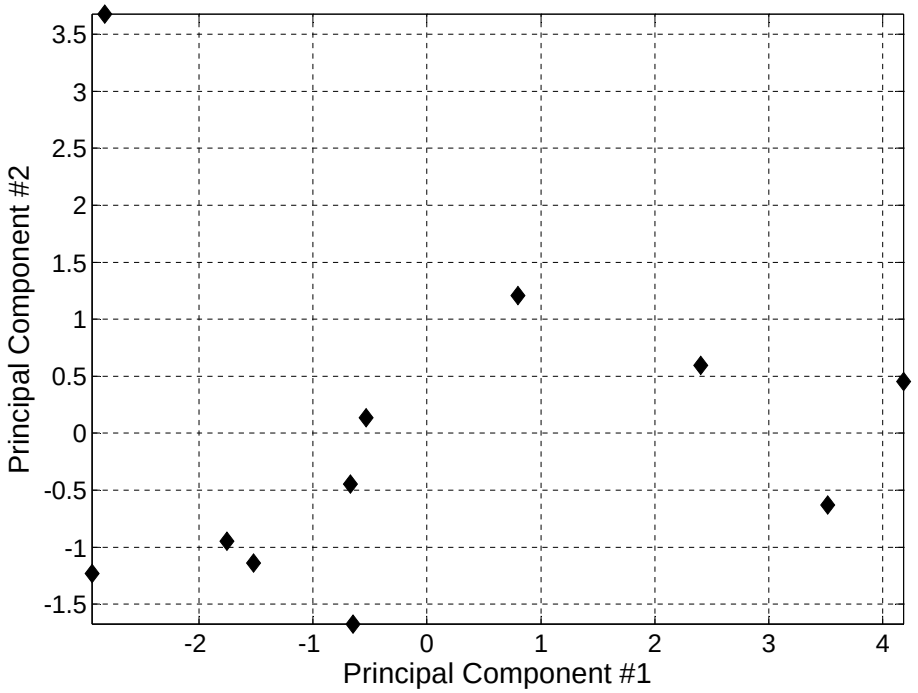

Figure 3.2: PCA scatter plot showing that the variability explained by PC1 is much higher than that explained by PC2.

Varimax rotation with Kaiser normalization (Kaiser, 1958) was applied to the principal components (PCs) to identify the key sites of variation in geometry. Varimax rotation is an orthogonal factor rotation method which is based on maximizing the variance of the squared factor loadings to improve the interpretability of each factor. The normalization step scales the rows of loadings to have norm 1 before rotation and then scales them back after rotation. For this study, the varimax rotation with Kaiser normalization was accomplished using MATLAB's built-in function for factor

rotation.

The contribution of each of the geometric parameters to the variations described by the PCs was depicted graphically using a biplot (see Figure 3.3). The variations in femur geometry were found to be due to: the greater-trochanter depth (GD), shaft-head distance (SH), neck axis length (NAL) and shaft width (SW) described by PC1; shaft depth (SD), greater-trochanter width (GW) and neck depth (ND) described by PC2; neck-shaft angle (NSA), neck width (NW) and head diameter (HD) described by PC3.

PC #	Eigenvalue	Unrotated components		Rotated components	
		% variance	Cum. Variance	% variance	Cum. Variance
1	5.9421	59.4215	59.4215	48.0433	48.0433
2	2.2637	22.6368	82.0583	34.2851	82.3284
3	0.6146	6.1463	88.2046	17.6716	100
4	0.5075	5.0746	93.2792		
5	0.2994	2.9942	96.2734		
6	0.1577	1.5771	97.8505		
7	0.1193	1.1926	99.0431		
8	0.0592	0.5916	99.6347		
9	0.0297	0.2973	99.932		
10	0.0068	0.0681	100.0001		

Table 3.1: Eigenvalues and % variances for the PCs

These results helped understand the geometric variations that needed to be considered for a bone quality analysis technique based on femoral shape. These variations may also be used with bone strength analysis to determine the extent to which bone strength has been affected by geometry.

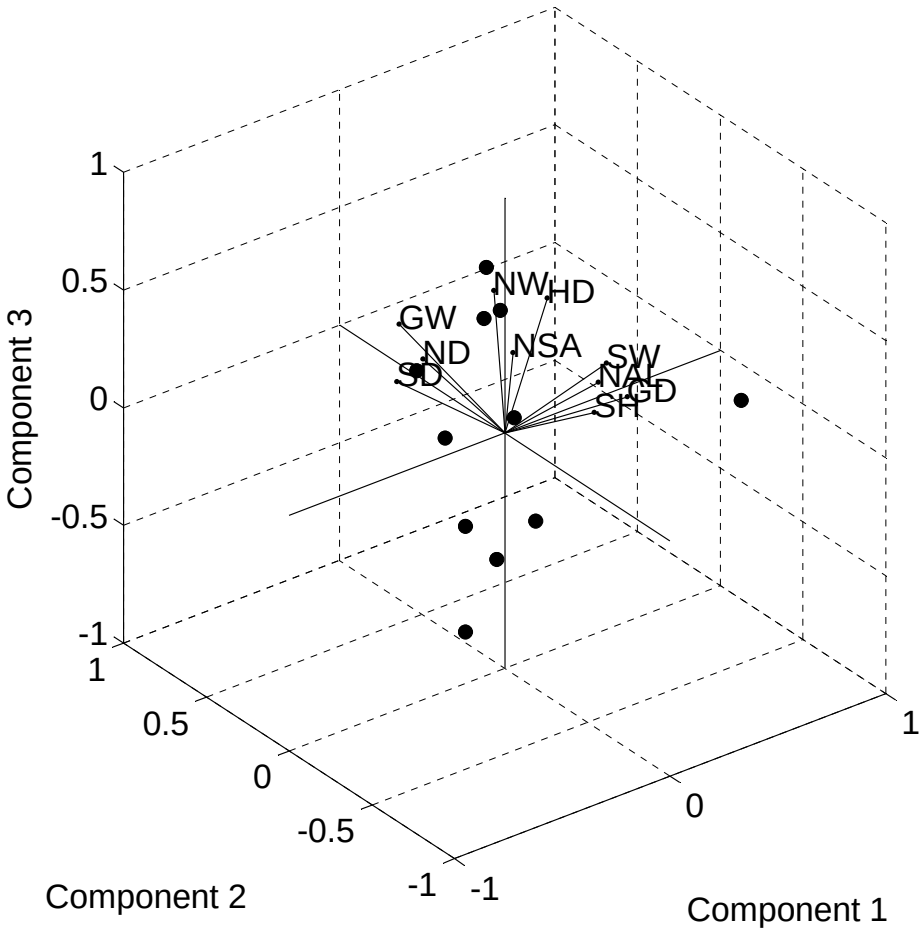

Figure 3.3: Biplot to visualize magnitude and sign of contribution of each variable to the first 3 PCs. The axes in the biplot represent the principal components, and the observed variables are represented as vectors. The points represent the PC scores for the observed variables.

The covariance between 2D and 3D geometry

Partial least squares (PLS) is used to study and analyse covariation between multiple blocks of variables. It generalizes and combines features from principal component analysis and multiple regression. It is particularly useful when we need to predict a set of dependent variables from a (very) large set of independent variables (i.e.,

predictors). Bookstein (1982) proposed a concept of partial least squares that centres around the interpretation of the singular values of a cross-block covariance matrix as the covariances of the linear combinations that use the singular vectors as coefficients. Bastir et al. (2005) used PLS morphological integration studies using covariation between two blocks of variables while Rohlf and Corti (2000) used it to study relationships between three-dimensional morphologies and their corresponding two-dimensional views.

Partial Least Squares (PLS) was applied to examine the pattern of covariance between the parameters that could be measured from a 2D image and those that were related to the 3rd dimension of bone geometry. The variables were split into two blocks accordingly with block X consisting of measurements in the X-Y plane such as shaft width, neck width, greater-trochanter width, shaft-head distance, neck axis length and neck-shaft angle, and block Y consisting of measurements along the Z-axis such as shaft depth, neck depth and greater-trochanter depth. The variance-covariance matrix R was computed as:

$$R = \begin{bmatrix} R_X & R_{XY} \\ R'_{XY} & R_Y \end{bmatrix} \tag{3.1}$$

Singular value decomposition (SVD) was used to extract the pairs of mutually orthogonal singular axes (SA) and associated singular values (SV) from this interblock variance-covariance matrix, R_{XY}.

$$R_{XY} = USV' \tag{3.2}$$

where the values along the diagonal of S gave the singular values and the columns of U and V formed the pairs of singular axes. The fraction of total variance described by each pair of singular axes was calculated (Table 3.2) and the first singular value (9.8079) was found to explain 91.52% of the total covariance between the blocks. The first 3 pairs of singular axes describing correlation between shaft width and depth

(SA1: r=0.9294,p=0), neck width and depth (SA2: r=0.7686,p=0.0057) and greater trochanter width and depth (SA3: r=0.7992,p=0.0032) were found to be significantly correlated ($p < 0.01$). It was hence argued that the missing dimension could be reconstructed to a reasonable degree from the known two-dimensional information.

The correlation between the X-block SA1 and Y-block SA1 is plotted in Figure 3.4. No significant ($p < 0.1$) correlation was found for these two singular axes with centroid size indicating that size was not responsible for this covariance between width and depth.

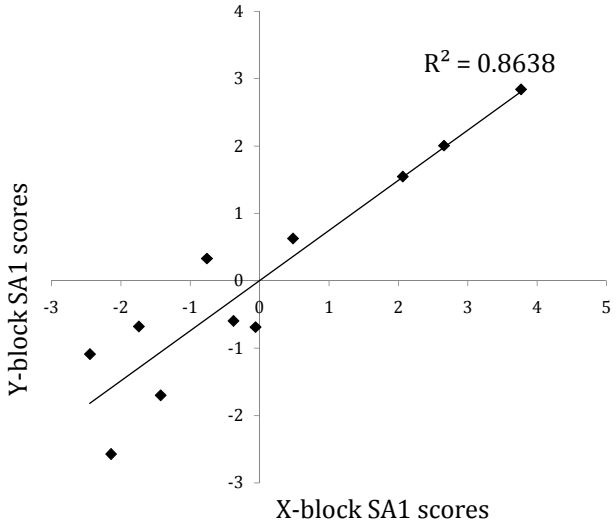

Figure 3.4: Plot of X-block SA1 vs Y-block SA1 scores for the human femur

SA #	Singular value	% variance	Cum. Variance
1	9.8079	91.5213	91.5213
2	0.8071	7.5312	99.0525
3	0.0985	0.919	99.9715
4	0.0031	0.0286	100.0001

Table 3.2: Singular values and % variances for the SAs

3.2.2 FEXI Validation

Finite element analysis (FEA) is an effective and widely used computer-based simulation technique for modelling mechanical loading of various engineering structures. In this technique, a series of linked discrete regions called finite elements are used to model the object (Pao, 1986). These elements are joined together at nodes along edges. Loads and restraints are applied to the assembly of elements. Specified loads and restraints are applied to the model and an array of simultaneous equations is constructed to describe the behaviour of the whole structure. Analysis of the model provides nodal displacements and induced stress distribution due to the applied load. Finite element analysis of a bone would therefore be dependent on the density of each element (cortical and cancellous), the overall shape of the bone (length and angle of neck, size and anteversion of head) and the internal structure of the bone.

As described in the previous chapter, Finite Element Analysis of X-ray Images (FEXI) (see section 2.4.4) is a recently developed technique which uses a radiographic image of a bone to create a 2D plane stress model for finite element analysis. This technique uses simulation of a compressive mechanical loading resulting from a sideways fall to the ground to compute the stiffness of the bone.

An initial experimental validation (Langton et al., 2004) was conducted to assess the performance of the FEXI technique with DXA and radiograph images compared with BMD to predict experimentally derived mechanical stiffness and yield load of the proximal porcine femur. A set of 23 porcine femora was used in this study as these were more easily available and also suitable since pig femurs are similar in shape and structure to the human femora in all except the femoral neck region - the

porcine femoral neck is shorter and thicker than the human one.

The head and shaft of the femora were platened with resin blocks. DXA and digital X-ray scans were performed for all of these femora. These were then subjected to mechanical compressive testing to determine yield loads. BMD was computed for each femur from the DXA scans. FEXI was performed for the DXA and radiograph images with the applied load being the same as the yield load obtained from mechanical testing. The stiffness values obtained from mechanical testing were taken as the gold standard for this study. The BMD and FEXI-derived stiffness values from the DXA and radiograph images were compared with this mechanical stiffness to assess the performance and accuracy of FEXI.

A good correlation was observed between FEXI-derived stiffness from DXA images with the experimentally derived mechanical stiffness and yield load ($R^2 = 0.56$ and $R^2 = 0.68$ respectively). This was better than the correlation of FEXI-derived stiffness from plain radiograph images with mechanical stiffness ($R^2 = 0.51$) and yield load ($R^2 = 0.61$).

The good correlation of FEXI (DXA)-derived stiffness with the yield load and the mechanical stiffness proves that FEXI provides a good estimate of bone strength, comparable to the results from BMD ($R^2 = 0.65$ for BMD with mechanical stiffness and $R^2 = 0.71$ for BMD with yield load). The poorer performance of FEXI with the radiograph images was attributed to the variability in exposure.

Graphs comparing the performance of FEXI and BMD for both the DXA and radiograph images with mechanical stiffness and yield load are shown in figure 3.5.

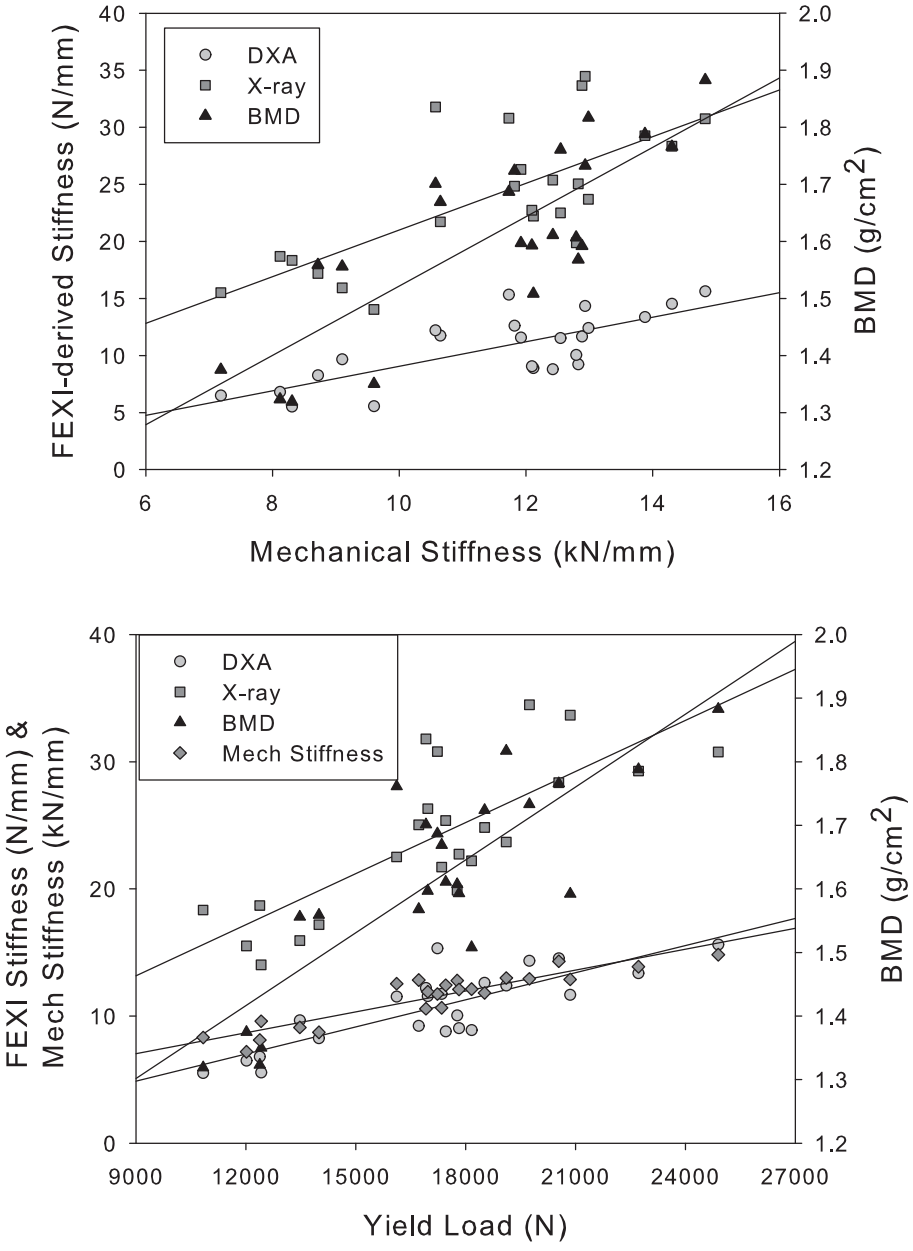

Figure 3.5: FEXI-derived stiffness compared with BMD, mechanical stiffness and yield load

3.3 Summarising the hypothesis

The observations from the above described case studies formed the basis for the research described in this thesis. The first study looked at determining the major sites of variation in the femoral geometry. It was found that over 60% of the variations in femoral geometry could be explained by characteristics that were measurable from a two-dimensional image. The Partial Least Squares analysis showed a high covariance between bone width and depth, thus lending weight to the hypothesis that the three-dimensional geometry of the bone may be predicted from corresponding information in two dimensions.

The porcine femur study was conducted to compare the bone stiffness prediction of 2D FEXI to bone mineral density analysis which is the current gold-standard for osteoporosis assessment. It was found that the correlation of 2D FEXI-derived stiffness with both mechanical stiffness and yield load was found to be comparable to BMD in this case.

In the above described study using 2D FEXI, the bone is considered as a thin plate of constant thickness. As described in the FEXI methodology, the material properties assigned to the finite element model are dependent on the computed volumetric density at each pixel of the input radiographic image. Assumption of a constant thickness across the bone introduces an inherent error in the stiffness calculation.

It was argued that an improved estimation of bone depth would reduce the error in volumetric density estimation and hence improve the accuracy of bone stiffness results. Also, three-dimensional shape information would allow the

spatial orientation of the bone to be considered under different loading conditions particularly anteversion of the femoral neck. This would, hypothetically, provide bone stiffness results comparable to stiffness analysis from CT scans and hence avoid the need for expensive CT scans as a possible means of bone quality assessments.

Carrying on with the development of the hypothesis, the following chapter looks at determining the sensitivity of FEXI to changes in the anatomical parameters using a simulated bone.

Chapter 4

Simulation Study

4.1 Introduction

The previous chapter looked at the main sites of variation in femoral geometry and also found that 2D FEXI derived bone stiffness was comparable to bone strength estimated by aBMD. In this chapter, the effect of the geometry variations on FEXI-derived stiffness and aBMD are analysed with a view to establishing the validity of the hypothesis that FEXI with shape information will provide a more accurate assessment of bone stiffness than either aBMD or 2D FEXI. This was accomplished using a simulation study using virtual models of the proximal femur as it would be difficult to create a compilation of clinical cases with such a specified range of variabilities.

The aim of this computer simulation study was to utilise a virtual proximal femur to examine whether 2D FEA (FEXI, finite element analysis of X-ray images) and 3D FEA computed stiffness of the proximal femur were more sensitive (defined

as relative change) than aBMD to changes in trabecular bone density and femur geometry. It is assumed that increased sensitivity will be indicative of an improved prediction of bone strength.

A virtual system was created to test the effects of the variations of the anatomical parameters of the proximal femur on the FEXI-derived stiffness. This knowledge will be useful when validating the 3D bone recreated from a radiograph.

4.2 System description

The virtual world component consisted of a virtual anatomy generator and a radiograph simulator. The FEXI technique was applied to the simulated radiograph to compute bone stiffness. ANSYS Finite Element solver was used to perform the FE analysis for all tests.

The FEXI computations were divided into two basic categories - 2D and 3D. 2D FEXI was performed on the radiograph using constant tissue depth to compute volumetric density. 3D FEXI was performed on the 3D femur models constructed from the virtual bone.

Multi Parametric Sensitivity Analysis (Choi et al., 1999) was used to study the relative importance of each parameter on the overall stiffness of the bone. In this technique, a range of variations is assigned to each input parameter to determine the relative importance of each parameter and analyse the sensitivity of the simulation results to these input parameters.

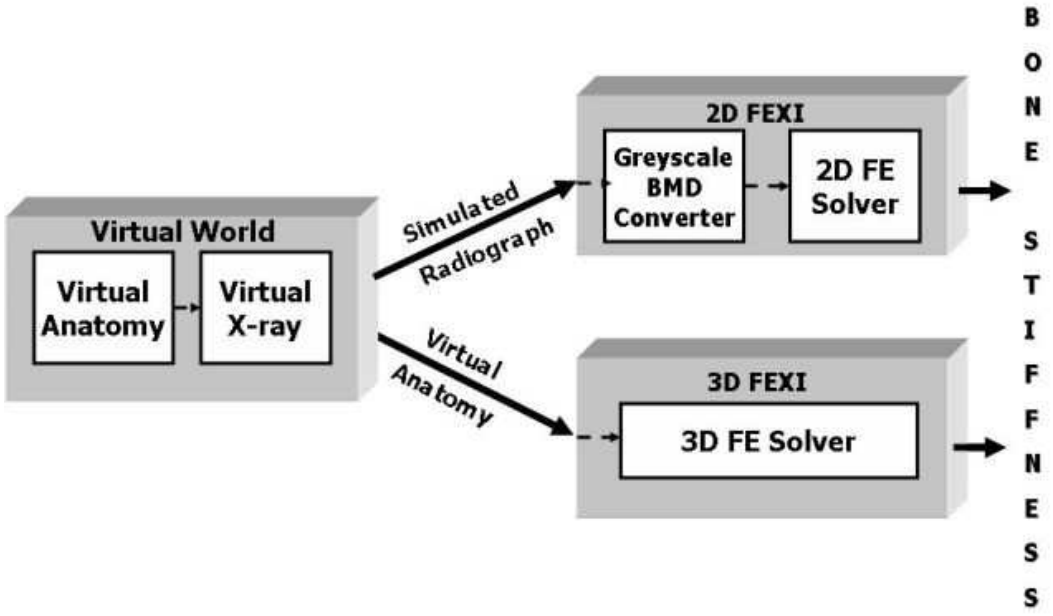

Figure 4.1: Virtual System Overview

Virtual World

A simplified virtual proximal femur was constructed as a voxel map using basic geometric shapes as shown in Figure 4.2; for example, the femoral head and diaphysis were represented by a sphere and a hollow tube respectively. This approach enabled the geometric parameters of the virtual proximal femur to be readily and independently varied.

Volume graphics techniques were used to model and manipulate the voxel data. The 'vxt' volume graphics class library written by Sramek and Kaufman (1999) was customized to build the voxel map for the proximal femur model, having a size of 192x192x192 voxels with each voxel being a cube with sides 1.3mm. Constructive Solid Geometry (CSG) operations and visualization techniques were applied to these

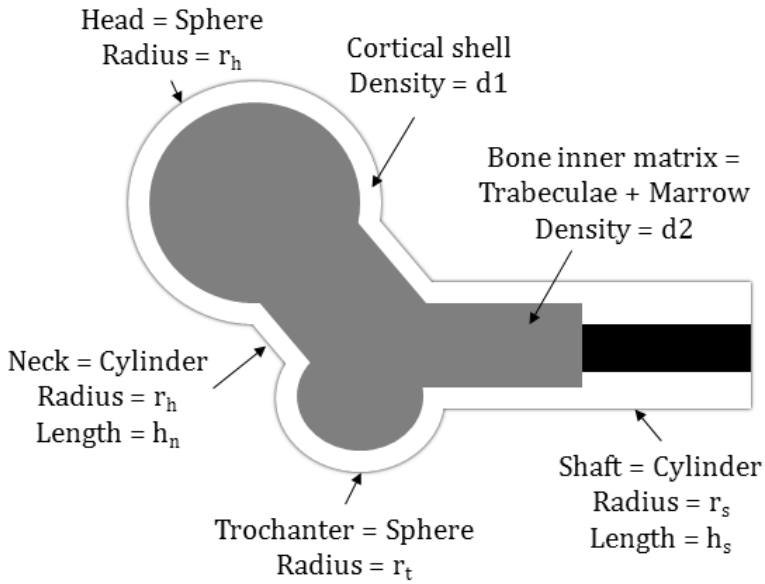

Figure 4.2: Virtual Femur Design

voxel-maps to achieve the desired femur model and visualize the results. The bone was modelled to have a cortical shell with density and thickness as given in Table 1 and the interior of the bone was simplified to have uniform density representing cancellous bone perfused with marrow. The relative dimensions of the geometric components of the virtual bone model were kept as close as possible to those for a typical femur (Gray, 2000). The reference values used for bone density and geometric parameters and parameter value ranges considered for the virtual bone model are described in Table 4.1.

The virtual femur was created and simulated support platens (with material properties of resin) were added to the femoral head and greater trochanter as shown in Figure 4.3.

Table 4.1: Proximal femur model parameters - reference values and parameter range considered for the simulation

Parameter	Reference Value	Parameter Range
Cortical bone density	$2gm/cm^3$	N/A
Trabecular bone density	25%	5 - 35%
Resin for support platen	255 (greyscale value)	N/A
Cortical shell thickness	1.45mm	0.725mm - 5.075mm
Radius of shaft	14.5mm	Not varied
Length of shaft	50.0mm	Not varied
Radius of greater trochanter	14.0mm	Not varied
Radius of neck	12.5mm	21.25 - 28.75mm
Length of neck	40.0mm	34 - 46mm
Neck-shaft angle	120^o	95^o - 125^o
Neck Anteversion	15^o	0^o - 15^o
Radius of head	24.0mm	20.4 - 27.6mm

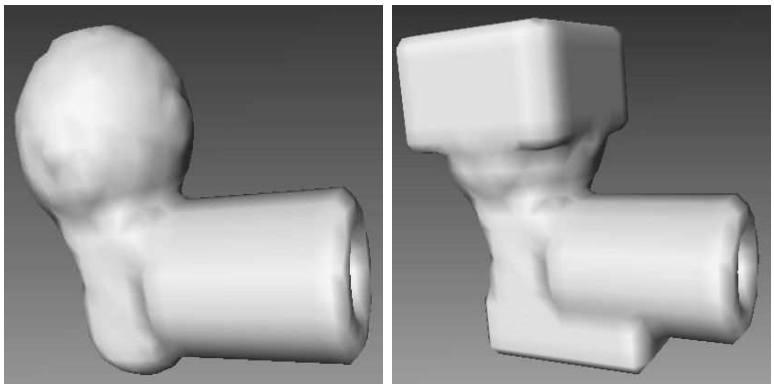

Figure 4.3: Virtual femur before and after platening

3D Finite Element Analysis

The three-dimensional femur model was stored as a discrete regular grid called a volume buffer or a voxel map, which is a large 3D array of volume elements known as voxels. A voxel is a cubic unit of volume centred at the integral grid-point and can be considered as the 3D equivalent of the 2D pixel that represents a unit of area.

Each voxel in the voxel-map contains a scalar value representing some property of the object occupying that unit of volume in the dataset. In the case of the femur model, each voxel contained the material density value for the bone at that position.

A finite element model is built up of discrete 'elements' formed by joining 'nodes' in a particular order. The material properties of the elements are defined in terms of the Young's modulus and the Poisson's ratio for the material. In 3D FEA, each element is made up of 8 ı

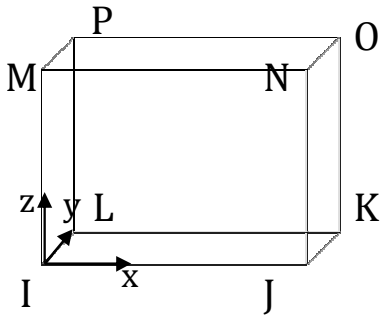

Figure 4.4: 3D ANSYS FEA element with nodes numbered from I to P as modelled for ANSYS

For 3D-FEA, each voxel in the voxel map of the virtual bone was considered to be a finite element. The material properties of the element were derived from the density at each voxel and the corresponding Young's modulus calculated using published regression data (Langton et al., 1996) for cancellous bone, noting that the portion of the proximal femur being loaded, between the femoral head and greater trochanter is predominantly cancellous with a thin cortical shell.

For the finite element analysis, a compressive mechanical loading was simulated, equivalent to a subject falling on their hip as described in the FEXI approach. Figure

2.6 shows the experimental arrangement that was being simulated. By applying a load between the femoral head and greater trochanter via support platens, the stiffness of the bone may be computed. The base support platen was restrained in both horizontal and vertical directions, with the load platen restrained in the horizontal direction. A vertical load of 2N was applied to the loading platen and its vertical displacement recorded. Dividing the applied load by the resultant platen displacement yielded the stiffness of the bone (Nmm^{-1}). A commercially available finite element analysis package, ANSYS (ANSYS Inc., PA), was used for solving the finite element models.

Radiographic Projection Simulation

Virtual radiographic images were generated using a ray-casting-based 2D projection algorithm. This algorithm used the number of bone voxels that a ray passes through divided by the voxel map depth in order to calculate the intensity (grey level) of each pixel on the image. Figure 3 shows a simulated radiograph for the virtual proximal femur detailing the cortical shell and medullary cavity and incorporating the support platens at the head and shaft.

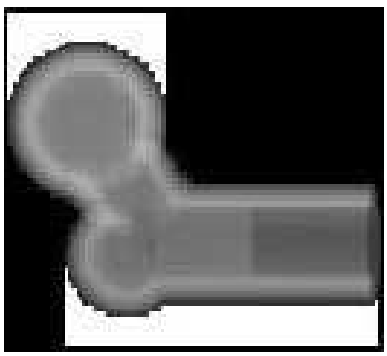

Figure 4.5: Simulated radiographic image for the virtual femur with support platens

2D FEXI and BMD

The 2D-FEXI technique (Langton et al., 2004, 2005) converts a conventional radiographic image, such as a DXA scan of a bone into a 2D plane stress model for finite element analysis. The finite element model was created using a bespoke software module (written in MATLAB (MATLAB Inc., MA)). In 2D finite element analysis, a plane element is used for modelling solid structures. Each plane element is made up of four nodes ordered from I to L.

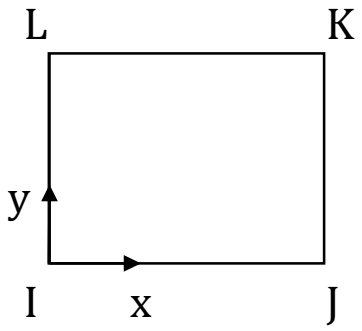

Figure 4.6: 2D FEA element

Each pixel in the image was considered to be a finite element. The grey level at each pixel was mapped directly to BMD using a regression equation derived from a DXA scan of a step wedge. The volumetric density at each pixel was then computed by dividing the areal density (BMD) by an assumed constant tissue thickness of 25mm (Langton et al., 2004). As for 3D FEA, Young's modulus for each element was derived from published regression data (Langton et al., 1996) and a compressive mechanical test was again simulated.

Apparent total hip BMD (aBMD) was calculated as the areal BMD for each 2D

projection image based upon the average grey level of the bone within the image.

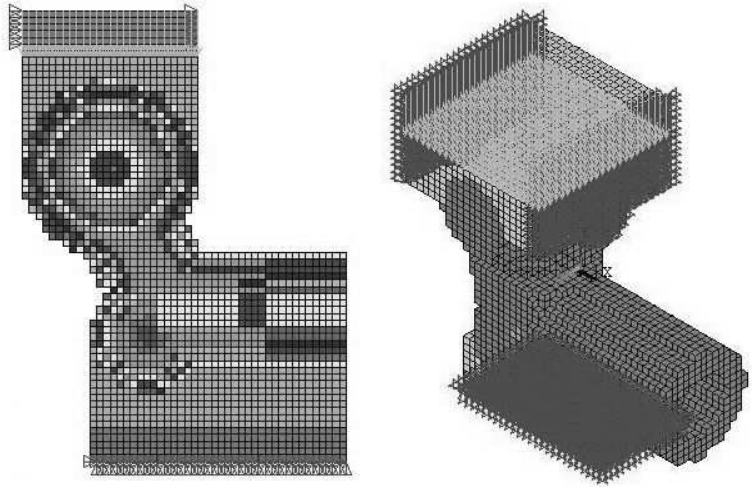

Figure 4.7: FE models generated from a 2D projection and the 3D model of the virtual femur

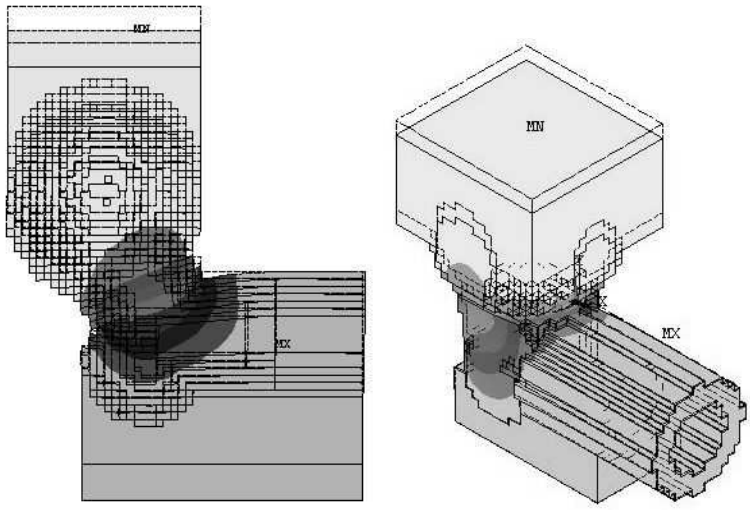

Figure 4.8: Displacement plots for 2D FEXI & 3D FEA

Anatomical Parameter Sensitivity

The sensitivities of stiffness derived from 3D-FEA and 2D-FEXI along with aBMD to variations in each anatomical parameter considered were plotted and trends set to best fit the data. The term sensitivity as used here was defined as the change in FEXI stiffness and aBMD from its baseline value for each value in the range assigned to each varied parameter (viz., trabecular density and the bone geometry parameters). For example, in the case of trabecular density, the sensitivity was computed as the change in FEXI stiffness and aBMD results for each change of $0.1 gcm^{-3}$ in trabecular density from the reference of $0.5 gcm^{-3}$ in the range 0.1 to $0.7 gcm^{-3}$.

Multi Parametric Sensitivity Analysis (Choi et al., 1999) was used to study the relative importance of each parameter on the overall stiffness of the bone. In this technique, a range of variations is assigned to each input parameter to determine the relative importance of each parameter and analyse the sensitivity of the simulation results to these input parameters. Table 1 describes the range of variation considered for each parameter in this study. For the MPSA analysis, an 'objective function' as defined by Choi et al. was computed using the equation

$$f_{h,m} = \sqrt{\frac{\sum_h (x_{o,h} - x_{i,h})^2}{k}} \tag{4.1}$$

which was the value of the function for a parameter h using a mode m, where we considered aBMD, 2D FEXI and 3D FEA as the 3 different modes of analysis. In the above equation, the term $x_{o,h}$ referred to the baseline stiffness and aBMD value and $x_{i,h}$ to the stiffness and aBMD values for the range (k) of values of parameter h. The baseline values were considered to be the stiffness and aBMD values obtained with the femur model parameters set to the references defined in Table 1. The relative

importance of each parameter for each mode, $\delta_{h,m}$ was then computed as

$$\delta_{h,m} = f_{h,m}/x_{o,h}. \tag{4.2}$$

Parameter sensitivity index value across all modes was computed as

$$\gamma_h = \sum_m \delta_{h,m} \tag{4.3}$$

(where m = aBMD, 2D FEXI, 3D FEA). Conversely, the sensitivity index of a mode to variations in parameters was computed as

$$\gamma_m = \sum_h \delta_{h,m} \tag{4.4}$$

(where h = trabecular bone density, cortical shell thickness, neck width, neck length, neck-shaft angle, femoral head radius, femoral neck anteversion). A 'relative sensitivity' index (S) was defined as the ratio of the relative importance of a parameter h for a mode m, $\delta_{h,m}$, to the sensitivity index γ. The relative sensitivity was computed both for individual parameters in each mode ($S_m = \delta_{h,m}/\gamma_m$) as well as for each parameter pooled across all modes ($S_h = \delta_{h,m}/\gamma_h$).

4.3 Results & Discussion

Both 3D-FEA and 2D-FEXI derived stiffness increased non-linearly with increasing trabecular density (Figure 4.9) with 2D-FEXI more sensitive (higher regression slope) than 3D-FEA; aBMD increased linearly and with low sensitivity (low regression slope).

There was a linear proportional increase with cortical shell thickness (Figure 4.10) for both 3D-FEA and aBMD; the sensitivity of 2D-FEXI was non-linear and slightly lower than 3D-FEA, both being significantly greater than aBMD.

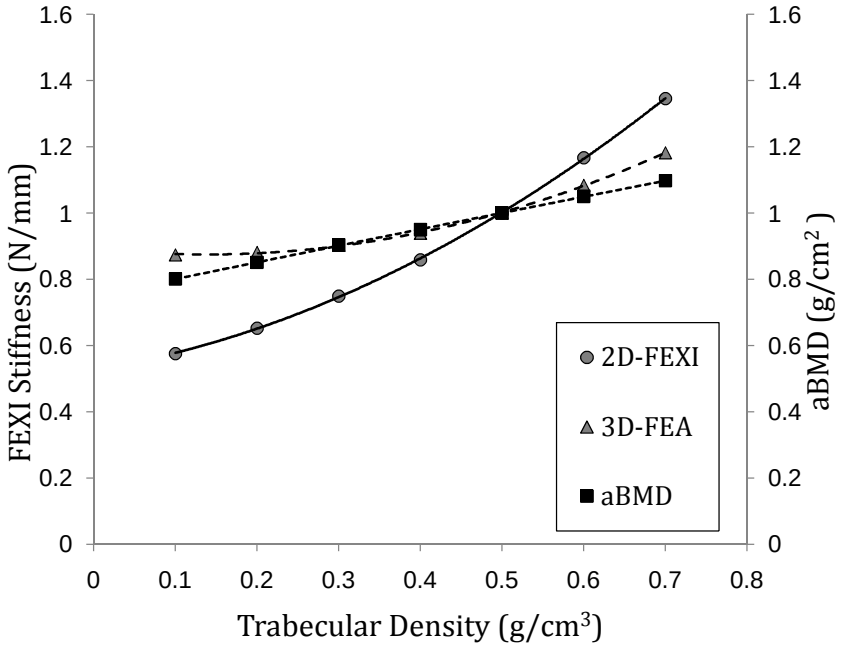

Figure 4.9: Plot of aBMD & FE analysis with varying trabecular density

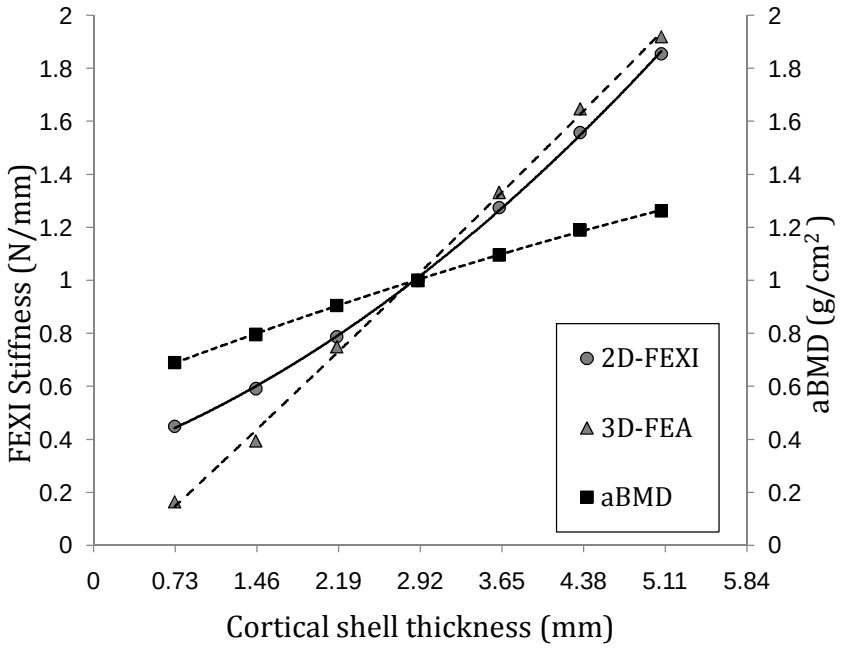

Figure 4.10: Plot of aBMD & FE analysis with varying cortical shell thickness

2D-FEXI demonstrated a slightly non-linear decrease with increasing neck length (Figure 4.11), being more sensitive than the linear sensitivity of 3D-FEA and aBMD. This agrees well with the findings of Faulkner (1995).

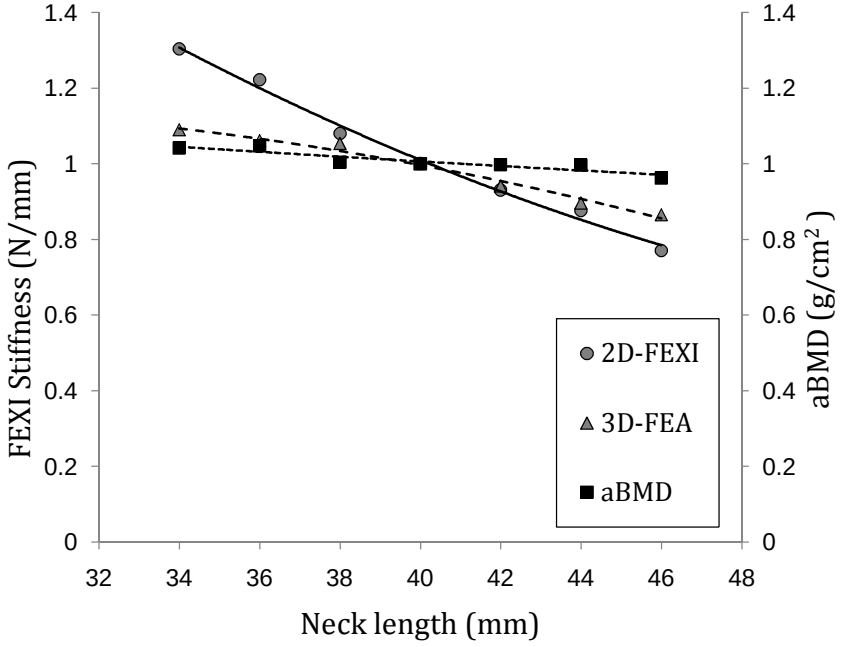

Figure 4.11: Plot of aBMD & FE analysis with varying neck length

All three measurement parameters demonstrated a linear sensitivity with both neck width (Figure 4.12) and neck-shaft angle (Figure 4.13). For neck width, 2D and 3D FE were similar and of higher sensitivity than aBMD. All three measurement parameters were insensitive to neck-shaft angle.

All three measurement parameters varied non-linearly with head radius (Figure 4.14); 3D FE demonstrated a positive trend whereas 2D FE and aBMD demonstrated a negative trend.

All three measurement parameters demonstrated non-linear behaviour with neck

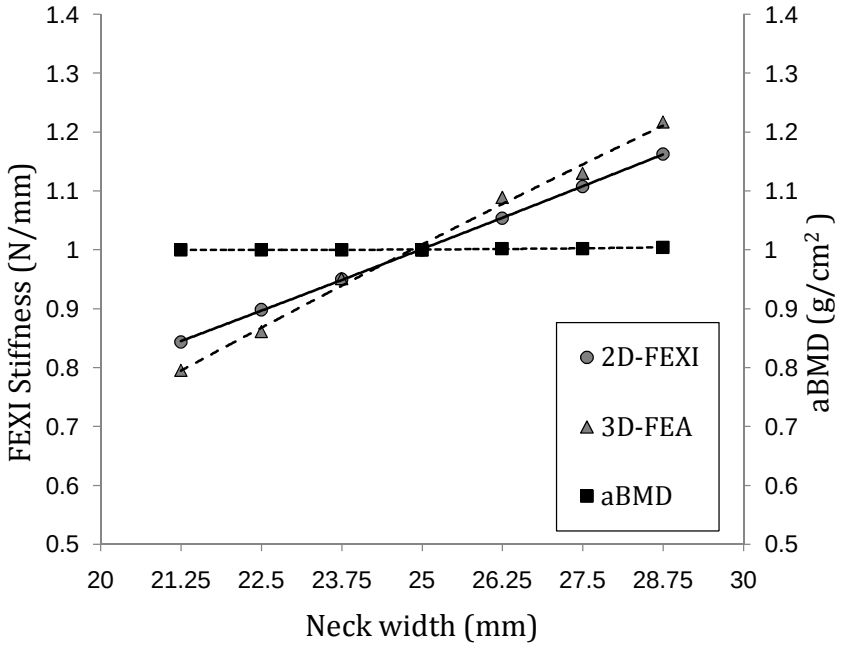

Figure 4.12: Plot of aBMD & FE analysis with varying neck width

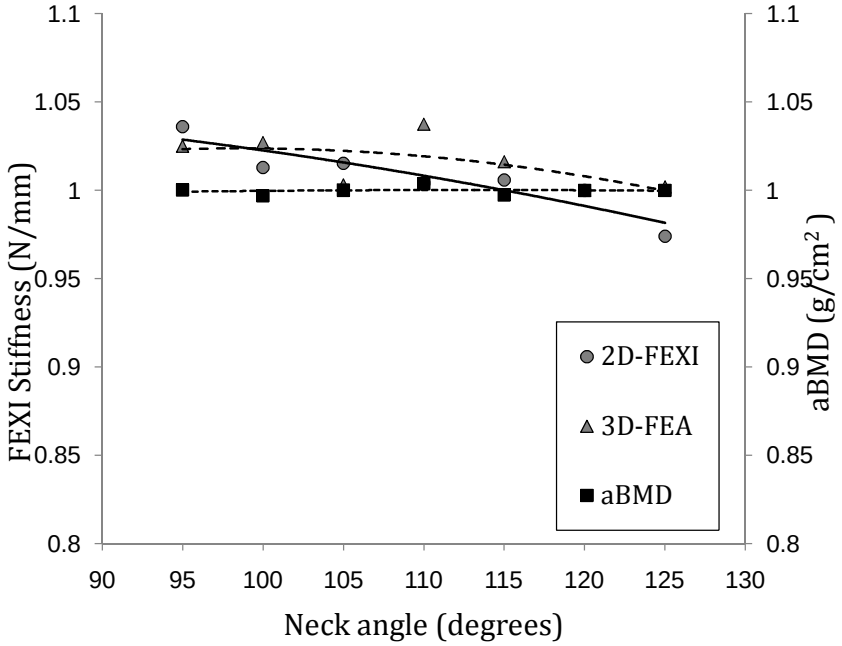

Figure 4.13: Plot of aBMD & FE analysis with varying neck-shaft angle

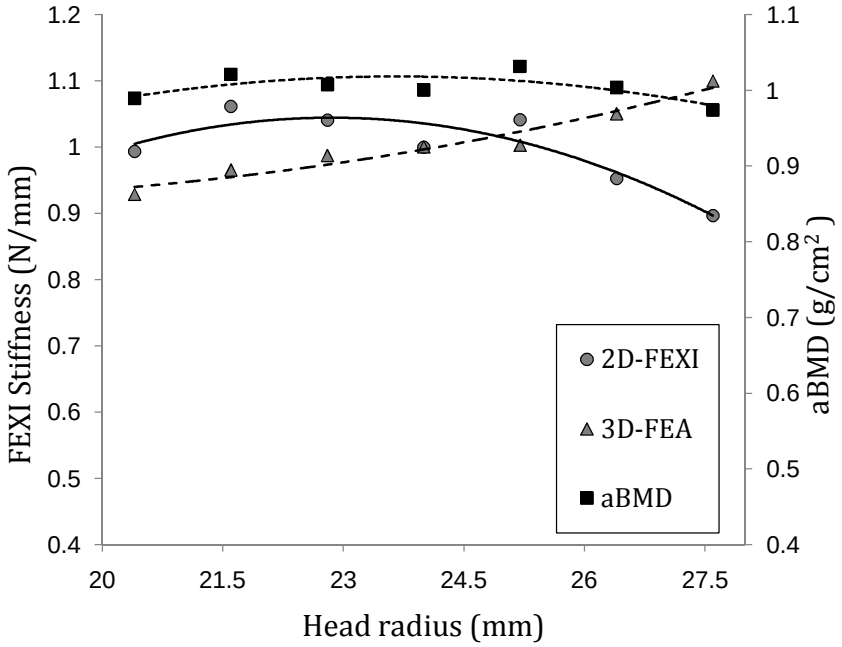

Figure 4.14: Plot of aBMD & FE analysis with varying head radius

anteversion angle (Figure 4.15), decreasing with increasing deviation either side of the reference value of 15^o; 3D FE was the most sensitive, followed by 2D FE and aBMD.

When trabecular density and all geometric parameters were considered simultaneously for each mode, 3D-FEA and 2D-FEXI had statistically equal ($\gamma_m = 0.41 \pm 0.20$ and $\gamma_m = 0.42 \pm 0.16$ respectively, p = ns) but significantly higher sensitivity indices than aBMD ($\gamma_m = 0.24 \pm 0.07$). The statistical significance level for 2D-FEXI against aBMD ($p = 0.002$) was higher than for 3D-FEA against aBMD ($p = 0.014$).

When the relative sensitivity of the three modes (aBMD, 3D-FEA and 2D-FEXI) was analysed separately against variation in trabecular density and the geometric parameters (S_h) (Figure 4.17), cortical thickness was found to have the most impact on derived bone strength among all three modes. As expected, trabecular density

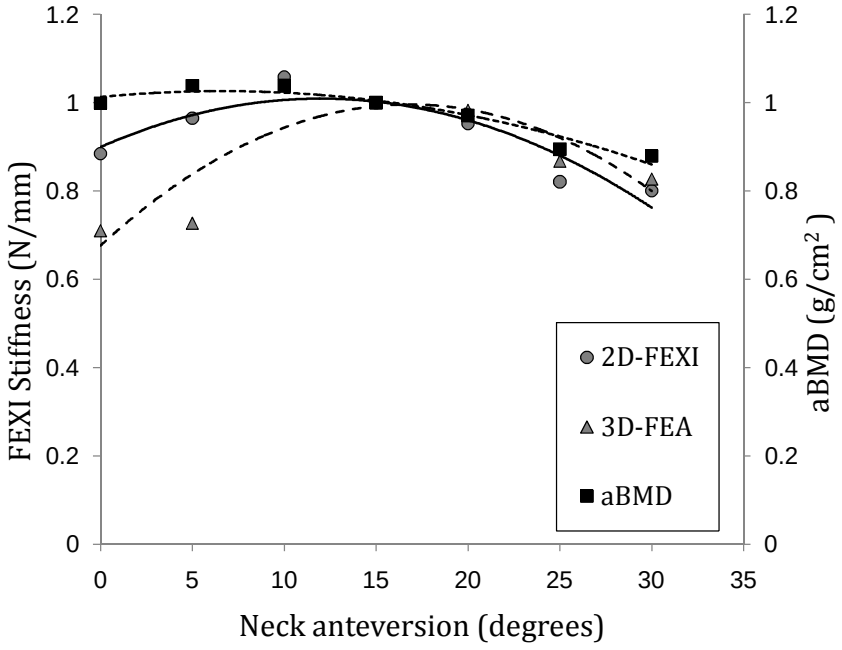

Figure 4.15: Plot of aBMD & FE analysis with varying neck anteversion angle

follows aBMD. Surprisingly, 2D-FEXI shows a significantly higher sensitivity to trabecular density and neck length than 3D-FEA. No scientific explanation could be found for this and was accepted for the time being as an anomaly to be analysed later if such a case arose with future clinical studies.

When all modes and anatomical parameters were pooled into a single analysis ($S_p = \delta_{h,m} / \sum_h \gamma_h$) (Figure 4.18), the highest sensitivity was achieved for cortical thickness variation using 3D-FEA ($S_p = 1.04$), closely followed by 2D-FEXI ($S_p = 0.84$) of this geometric parameter. Surprisingly, the next highest sensitivity was for trabecular density variation using 2D-FEXI ($S_p = 0.48$), with aBMD and 3D-FEA having significantly lower, and equal, sensitivities ($S_p = 0.19$).

Using relative sensitivity classification thresholds of $High >= 0.5$, $0.2 <= Moderate < 0.5$, and $Low < 0.2$, the results of the MPSA sensitivity analysis

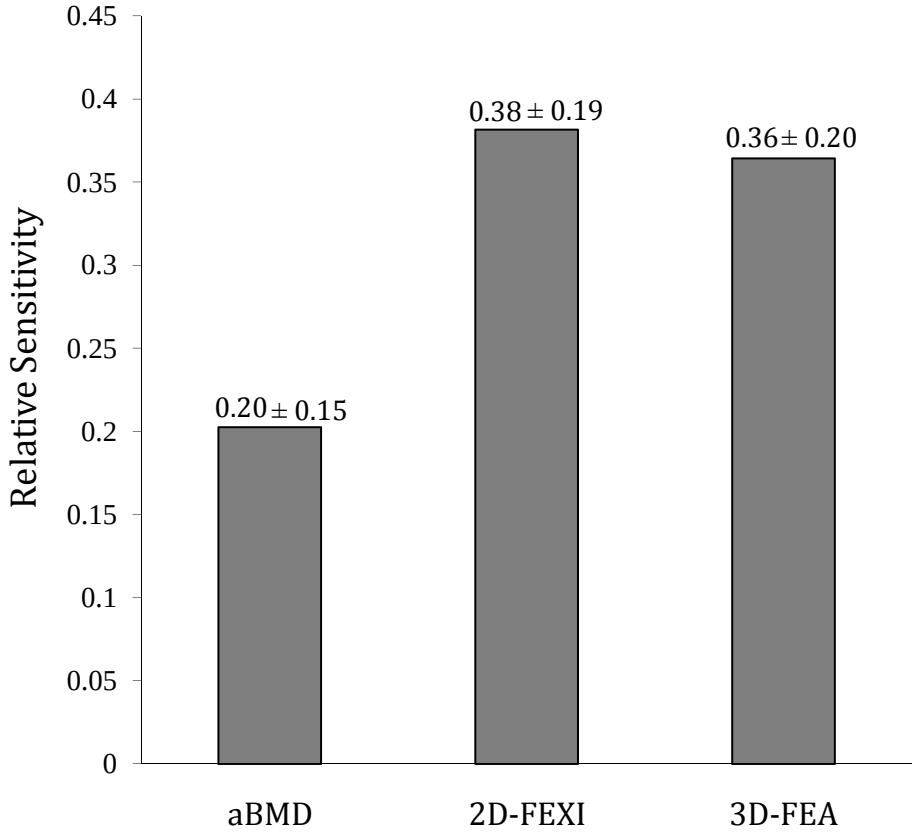

Figure 4.16: Mean and standard deviations in sensitivity of each measurement parameter with all parameters considered simultaneously for each mode

were summarized in Table 4.2. These results showed that both 3D FE and 2D FE were more sensitive to several geometrical parameters than aBMD.

This simulation study helped to analyse and understand how variations in geometric parameters affect the stiffness and hence strength of a bone susceptible to osteoporotic fracture. It suggested that finite element analysis of 2D radiographic images could provide an improvement in osteoporotic fracture risk assessment than currently provided by aBMD.

A simulation approach was useful for validating the performance of a computer based

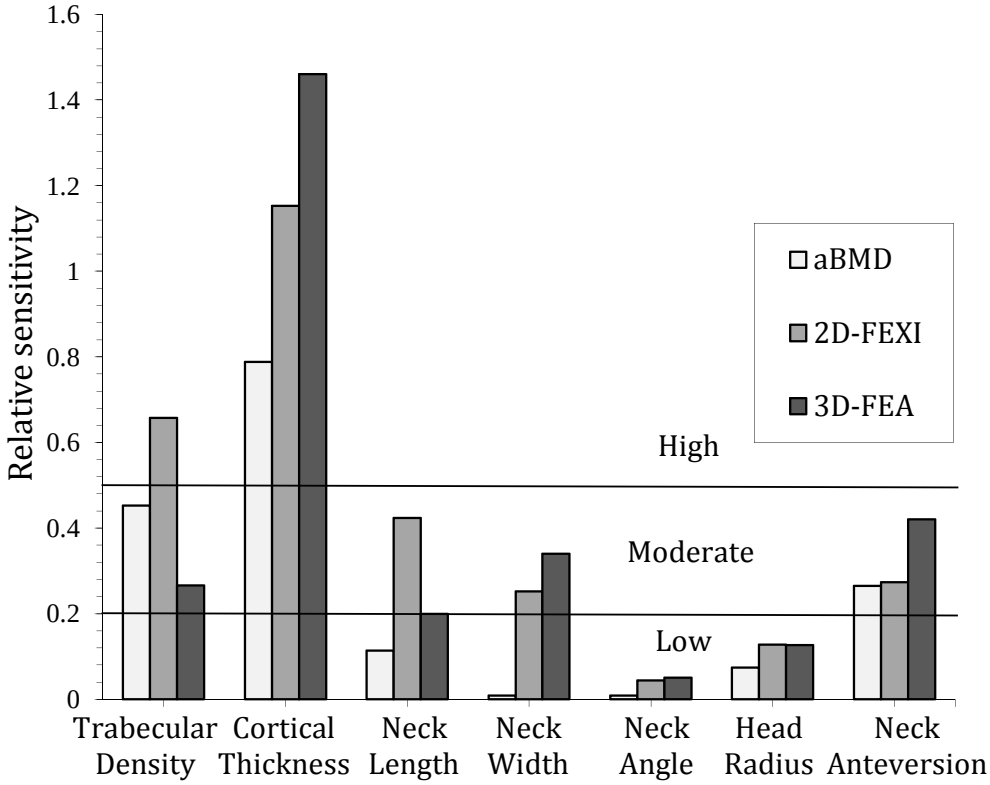

Figure 4.17: Relative sensitivity to parameter variations analysed separately for aBMD, 2D-FEXI & 3D-FEA

Table 4.2: Relative sensitivity of the various geometric parameters - Analysed separately

Parameter	aBMD	2D	3D
Trabecular density	Moderate	High	Moderate
Cortical shell thickness	High	High	High
Neck length	Low	Moderate	Moderate
Neck width	Low	Moderate	Moderate
Neck-shaft angle	Low	Low	Low
Head radius	Low	Low	Low
Neck anteversion	Moderate	Moderate	Moderate

analysis technique such as 3D and 2D finite element analysis, whereby geometric parameters could be readily varied, an onerous task if the study was performed ex

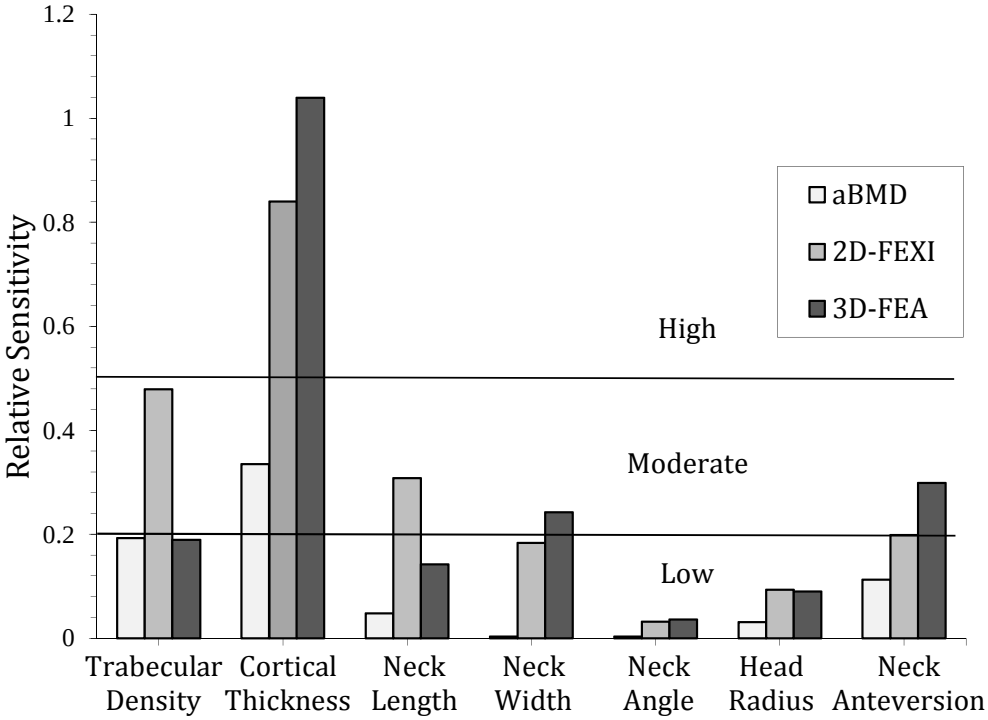

Figure 4.18: Relative sensitivity to parameter variations, analysed with all measurement and geometric parameters pooled together

Table 4.3: Relative sensitivity of the various geometric parameters - Pooled Analysis

Parameter	aBMD	2D	3D
Trabecular density	Low	Moderate	Low
Cortical shell thickness	Moderate	High	High
Neck length	Low	Moderate	Low
Neck width	Low	Low	Moderate
Neck-shaft angle	Low	Low	Low
Head radius	Low	Low	Low
Neck anteversion	Low	Moderate	Moderate

vivo. However, as this approach relied on simulated data from a simplified virtual bone model, the sensitivity results with actual data could be different due to the inherent complexity in the structure of bones. In order to minimise the effect of the model simplification, the basic dimensions and range of variations in parameters

of the virtual bone were set based on typical bone dimensions (Gray, 2000). Also, the basic shape and the ratio of cortical and cancellous bone of the model were modelled to correspond to those of real femurs. However, the actual inner trabecular architecture of the bone was not modelled and the interior was instead assumed to have uniform density. The incorporation of the internal structure modelled as a mesh structure is planned as a future enhancement to the simulation study. It is expected that a more detailed model would corroborate these results that show a better sensitivity to femoral geometry for the FEXI-derived stiffness compared to BMD.

As found ex vivo, the mechanical integrity of the proximal femur is most dependent upon cortical thickness (Calis et al., 2004; Partanen et al., 2001; Pulkkinen et al., 2004). The study demonstrated that 3D FE and 2D FE (FEXI) were significantly more sensitive to the anatomical shape and composition of the proximal femur than conventional BMD and may improve upon the prediction of bone strength and fracture-risk currently provided by conventional BMD assessment.

It was somewhat surprising to note that 2D FEXI provided a higher sensitivity than 3D FEA, as shown in Figure 4.18, for trabecular density and neck length. Although a scientifically based explanation cannot be offered at this stage, this may be related to the fact that in the derivation of volumetric density within 2D FEXI, a constant bone thickness of 25 mm was incorporated.

4.4 Conclusions

This simulation study indicated that FEXI-derived stiffness was indeed responsive to variations in bone geometry as well as changes in bone density. As bone strength depends on the physical characteristics of bone among other factors along with bone density, it was argued that FEXI with incorporated bone shape information would yield a better prediction of bone strength compared to aBMD alone. The case for this research was thus deemed to be established.

The following chapter looks at the various techniques for shape reconstruction from two-dimensional images and lays the foundation for the development of a shape template for the proximal femur.

Chapter 5

Shape Analysis and Reconstruction

As seen from the simulation study in the previous chapter, response of FEXI to variations in bone geometry correspond to results from clinical studies analysing effects of geometric parameters of the bone on fracture-risk. The basic objective of the shape analysis component of this research was to build a shape model to provide tissue depth information across the proximal femoral bone for use with FEXI with a view to prove the hypothesis that FEXI with shape information would provide a more accurate assessment of bone strength than 2D FEXI and also aBMD.

The first section of this chapter lists various reconstruction techniques developed and used by researchers for some common medical imaging modalities such as X-ray, Computed Tomography (CT) and Magnetic Resonance Imaging (MRI). These techniques have been grouped broadly into those that use multiple slices or projections for the reconstruction and those that use some combination of statistical analysis on a set of images and use this statistical information along with the input

image data to reconstruct the three-dimensional shape. The second section focuses entirely on the core concepts within the realm of geometric morphometrics and how they are relevant to the research described in this document. The final section describes the process of selecting the appropriate techniques for the application and how they fit together in this case.

5.1 3D Reconstruction Techniques

5.1.1 Using Multiple Projections

Three-dimensional modelling of anatomical features from medical images is not a new concept. A review of three-dimensional medical imaging algorithms and computer systems is given by Stytz et al. (1991). Computed Tomography (CT) and Magnetic Resonance Imaging (MRI) are two of the most common imaging modalities used to generate three dimensional views of an object, typically an anatomical structure.

Computed Tomography (CT)

CT scanning uses X-rays to generate cross-sectional slice-by-slice views of body parts. For this, a large series of X-ray slice data is obtained about a single axis of rotation around the object. Data scans are progressively generated using X-ray sensors positioned opposite to the X-ray source. The numerical value assigned to each pixel in a CT slice is expressed in Hounsfield Units (HU) and is computed as the average attenuation value of the tissues relative to the attenuation of water. Water

is assigned an attenuation value of 0HU, cancellous bone is typically displayed as +400HU and attenuation value for cortical bone is around +600HU (Jackson, 2004). The scanned CT slices are segmented using the appropriate HU range to isolate the anatomy under consideration.

Magnetic Resonance Imaging (MRI)

Magnetic Resonance Imaging uses radio frequency signals applied to an object in a magnetic field and hence avoids the side-effects of radiation exposure. When a body, which is approximately 70% water, is placed in a magnetic field, the hydrogen atoms in the water molecules align with or against the magnetic field depending on their energy state. Radio frequency signals are used to change the excitation state of these hydrogen atoms causing a change in the net magnetisation vector of the object (Puddephat, 2002). The image is created based on measuring the return of the atoms to their original alignment. As the RF pulses target the hydrogen atoms in the water molecules in tissues, this technique is better suited to studying soft tissues such as muscles and blood vessels rather than calcified tissues such as bone. Both MRI and CT are expensive procedures compared to two-dimensional imaging modalities such as X-ray and DXA scans and are not prescribed for routine assessment.

Reconstructing the slices

One of the simplest methods of 3D reconstruction from CT or MR slices is using multiplanar reconstruction. The series of contiguous axial slices are stacked to create the volume which can then be sliced through different planes (typically orthogonal)

to obtain different views of the object. Interpolation of identical rows from each transaxial image creates a coronal view and interpolation of identical columns creates a sagittal view.

Lorensen and Cline (1987) proposed the marching cubes algorithm for 3D surface reconstruction from multiple 2D slices of medical images. Ray-casting algorithms along with a combination of surface-rendering algorithms were used by Hohne et al. (1989) for visualization of 3D reconstructed surfaces from multiple 2D slices obtained from CT and MR scans. Subsol et al. (1994) proposed the development of an anatomical atlas for the human skull using data obtained from CT images by extracting and registering features along the surface of the object to be reconstructed. The deformations were explained with reference to a 'feature average' constructed after registration of all the specimens in the training set. Active contour models were employed by Safont and Marroqun (1999); Zhao et al. (2000) for reconstruction of the proximal femur from slices obtained from Computed Axial Tomography (CAT) and MRI scans respectively.

Another popular 3D surface reconstruction approach involves back projecting multiple 2D projections of an object. Sun et al. (1994) compared the performance of Lagrange-multiplier (LMA), conjugate gradient (CGA) and minimum voxel representation (MRA) algorithms for a '3-view reconstruction' of the coronary arteries. The surface error rate (SER) was computed as a measure of the percent difference of object voxels between the original shell structure and the reconstructed shell structure and found to be 5%, 4% and 8% for the three techniques respectively. The MRA was however concluded to be the most practical for clinical applications because of its fast convergence. Reconstruction of the spine, rib cage and pelvis was studied by Delorme et al. (1999) using three x-ray images taken at specific angles

to the object. A combination of Direct linear transformation (DLT) and free-form deformation using dual-kriging algorithms were used to generate the patient-specific 3D models from the x-rays. Overall accuracy of $3.5 \pm 4.1mm$ were reported for an in-vivo validation study of 40 scoliotic vertebrae.

Caponetti and Fanelli (1990) developed a 3D reconstruction algorithm from two mutually orthogonal X-ray views of the femur, which was later improved upon by (Nikkhade-Dehkordi et al., 1996). In both these cases, the femur was considered in sub-parts, each having a smooth, round surface. The 3D shape was estimated by median filtering and contour finding on different parts of the X-ray images and generating each sub-part using Hermite surface patches. Hermite surfaces are cubic parametric surface patches defined by four corner points and the tangent vectors to the surface at the corner points (Foley et al., 1990). The reconstructed femurs were compared to CT-scan models and 80% of the femur shaft was found to have less than 2mm error and 93% less than 4mm.

Mitton et al. (2000) and Mitulescu et al. (2002) developed a technique based on non-stereo corresponding points (NSCP) from two orthogonal radiographs for reconstruction of the 3D geometry of upper cervical vertebrae. Direct linear transformations along with NSCP and a kriging algorithm (Trochu, 1993) were used in the latter study. The accuracy of the technique was evaluated using point-to-surface distances and found mean errors of around 1.4mm and root mean square errors of nearly 4mm between the models obtained from this reconstruction and those modelled from CT scans for 58 scoliotic vertebrae in 14 patients. Laporte et al. (2003) later introduced the concept of non-stereo corresponding contours (NSCC) based on contours identification from biplanar radiographs for 3D reconstruction of the distal femur. These were used by Kolta et al. (2004) for reconstruction

of the proximal femur from orthogonal biplanar DXA scans. The reconstructed models showed good accuracy as compared with high-resolution (0.25mm pixel size, 1.25mm slice thickness) personalized CT-scan models for 25 cadaveric femurs (mean error= $0.8mm$ and 95% of errors $\leq 2.1mm$). Maximum errors of up to 7.8mm were obtained on the greater and lesser trochanters.

5.1.2 Statistical Shape Analysis

In the clinical setting, two shapes may be similar but are rarely identical. Moreover, there are various rotational and positional variations inherent to medical imaging modalities. The distance of the scanner from the object being scanned also has an effect on the size of the image obtained. Statistical shape analysis consider shapes invariant of its translational, rotational and scaling effects and hence would be able to model these variations better than traditional reconstruction techniques.

Cootes and Taylor (2004) presented the concept of Active Shape Models (ASM) to describe locations of features in a target shape with respect to a reference shape. Active Appearance Models (AAM) then synthesized images of new shapes using the ASM. Procrustes Analysis (see section 6.3.3) was used to align the shapes in a training set and Principal Components Analysis (PCA) (see section 3.2.1) employed to model the variation among the shapes. A probability density function of the principal components was defined to fit new images to the model shape. Statistical appearance models using texture maps then generated 'photo-realistic synthetic images'.

Blanz et al. (2004) used a training set generated using high resolution laser scans of 100 faces to reconstruct faces from photographs. They used a combination of probability density functions and regularized least squares fit for the reconstruction and obtained results with reconstruction errors ranging from 3.16mm (using 17 landmarks) to 2.24mm (using 1000 landmarks).

5.2 Preliminary analysis

5.2.1 Depth prediction using grey levels

Several techniques were considered for the prediction of the missing dimension in the input data. The simplest was the direct approach using a regression from the grey value at each pixel of the DXA image to the actual depth of the bone at that pixel. Figure 5.1 shows a typical pelvic radiograph image.

As can be seen from the figure, the interior of the bone is not solid and the projected grey value of a radiograph pixel depends on the trabecular structure at that point. This made it extremely difficult to generalize the relationship between the grey level and bone depth. Another problem with this approach was the presence of overlying features such as the pelvic bone, in the procured radiograph image. This affected the grey level and hence the predicted depth in the overlapping regions. Yet another drawback of this approach was its inability to identify protruding features such as the inter-trochanteric crest and the anteversion of the head with respect to the shaft.

Figure 5.1: Pelvic radiograph

5.2.2 Regression techniques

The term 'regression' is used to describe methods that attempt to quantify the relationship between two sets of variables by fitting one set to the other. Regression methods may be used to explain and estimate relationships between the two blocks of data or to predict one from the other. These two blocks of data are often referred to as 'predictor' and 'response' variables (Manly, 2000).

The measure of similarity

The measure of similarity between any two shapes was defined as a function of Euclidean distance (Manly, 2000). Considering d_{ik}, the Euclidean distance between

shapes i & k:

$$d_{ik}^2 = \sum {x_{ij} - x_{kj}}^2 = s_{ii} + s_{kk} - 2s_{ik} \tag{5.1}$$

where j = 1:p , p is the number of variables.

Similarity matrix was computed as: $S = XX'$
where s_{ik}, the element in the i^{th} row and k^{th} column of XX', gave the measure of the similarity between shapes i & k. As the distance between the shapes d_{ik} decreases, s_{ik} increases.

$$\%similarity = \frac{observed\ s_{ik}}{max\ s_{ik}} \tag{5.2}$$

$max\ s_{ik} = \frac{s_{ii}+s_{kk}}{2}\ when\ d_{ik} = 0$

Using multivariate regression

The simplest case of regression, known as univariate regression, involves only one predictor variable. Multivariate regression uses an entire set of predictor variables to explain or predict a response variable. When the multivariate regression involves multiple response variables, the analysis is known as multiple multivariate regression.

Multiple multivariate regression may be defined using the formula (Rohlf and Corti, 2000):

$$B = inv(X'X) * (X'Y) \tag{5.3}$$

$$Y1 = X1 * B \tag{5.4}$$

Multiple multivariate regression was used to predict a set of 3D landmarks defining key points on the bone surface from a set of 2D landmarks on the input DXA image.

The plan was to use a training set to define the co-efficients of regression between the 2D and 3D co-ordinates for these key points. If the 3D co-ordinates could be predicted with a significant level of accuracy, the bone surface was to be built by warping a template shape using these as control points.

A training set X_t of 3D landmarks was generated using a MicroScribe G2 digitizer (Immersion Corporation, CA) for 7 cadaveric femora. The landmarks were aligned using the Generalised Procrustes Analysis (see section 6.3.3) to get a mean landmark configuration $meanX_{3D}$. The regression was executed in two stages.

In the first stage, a subset of the 3D landmark configuration, X_{3D-sub}, was extracted based on the ease and reliability of their definition in a 2D projection. These formed the set of 2D landmarks, X_{2D}. For this subset, a regression from the known (x,y) to the unknown (z) dimension was computed using equation 5.4.

$$X_{2D} \rightarrow X_{3D-sub} \tag{5.5}$$

```
% get the z-coordinates for the subset of 2D landmarks
Z = Xt(size(X2D,1),3);

% find the regression co-efficients from (x,y) to z for the subset
B = inv(X2D' * X2D) * X2D' * Z;

for specimen = 1:samples
% For each specimen, the z co-ordinates for its 2D landmarks are computed
Z2D = [I X(specimen)] * B;

% The subset 3D landmarks for the specimen
```

```
X3(specimen) = [X(specimen) Z2D];
end
```

The similarity of this subset of 3D landmarks from their corresponding 2D coordinates was an impressive 99%.

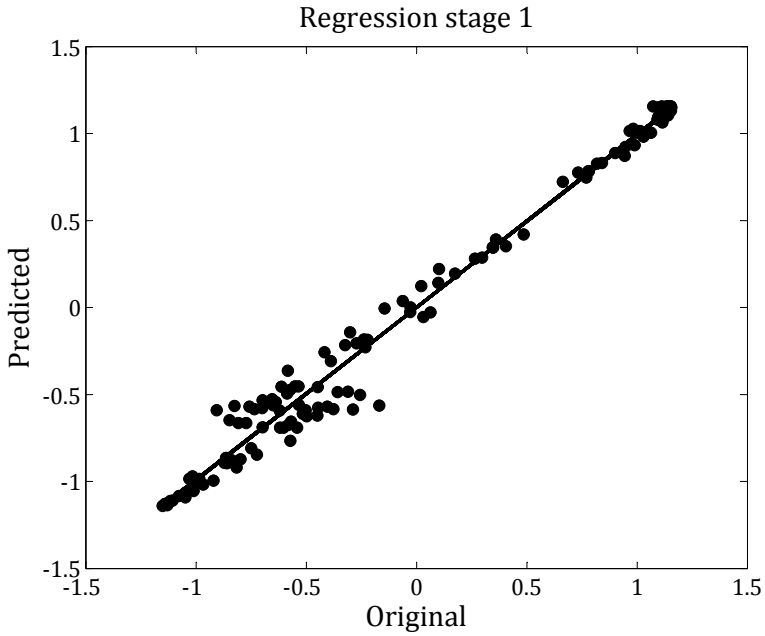

Figure 5.2: Similarity measure for regression model stage 1 - from 2D to 3D subset - for the entire specimen set

The full set of 3D landmarks was then regressed from this subset of 3D points using a similar multiple multivariate regression equation.

$$X_{3D-sub} \rightarrow X_{3D-full} \tag{5.6}$$

```
I = ones(size(Xt,1),1);
X_rem = ones(size(Xt,1)-size(X3D_sub,1),3);
```

```
% pad the 3D subset matrix with 1's for regression
Z1 = [X3;X_rem];

% pad the mean 3D subset matrix with 1's for regression
X1 = [Xt(1:size(X3,1),:);X_rem];
X1 = [I X1];

% get the regression co-efficents from 3D subset to full set
B = inv(X1' * X1) * X1' * X3D;

for specimen = 1:samples
% Apply to each specimen
X3_full(:,:,specimen) = [I Z1(:,:,specimen)] * B;
end
```

Using the above measure of similarity, the multivariate regression approach provided results of approximately 40% similarity between the actual and predicted shapes for the full set of 3D landmarks.

Using Partial Least Squares regression

Partial Least Squares (PLS) regression is a technique that combines features of Principal Components analysis (PCA) and multivariate regression. It is typically used in studies where the number of predictors is much larger than the number of response variables. While PCA finds a set of components that minimize correlations within a given block of variables, PLS searches for components that maximize the

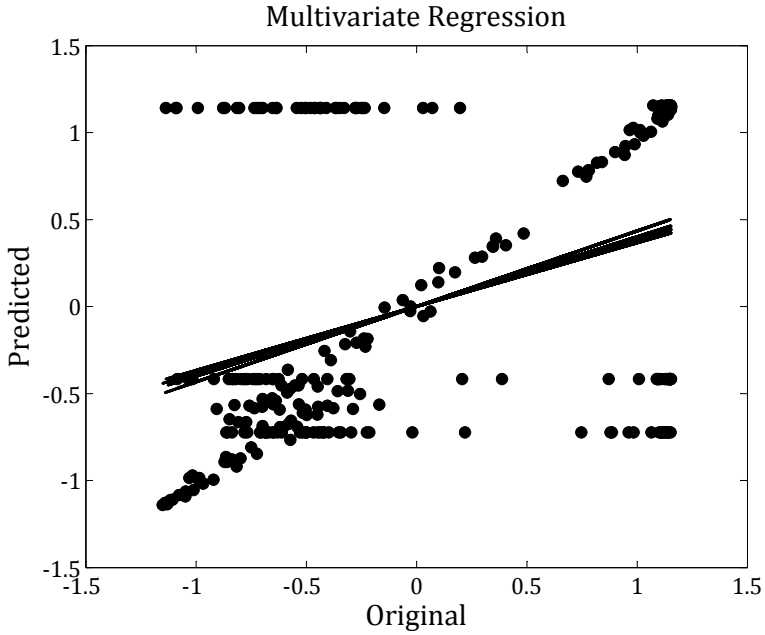

Figure 5.3: Similarity measure between full set of actual and predicted 3D landmarks for all the specimens using multivariate multiple regression at stage 2.

covariance between the predictor (X) and response (Y) blocks. In the context of PLS regression, these components are known as 'latent vectors' (Wold et al., 2004). This is achieved by a simultaneous decomposition of X and Y as a product of a common set of orthogonal factors and factor loadings. This decomposition is followed by a regression step to predict the Y block from the decomposition of X.

The predictor block X is decomposed as $X = TP'$ where T is the matrix of scores such that $TT' = I$ and P gives the loadings. Y is then estimated as $\widehat{Y} = TBC'$ where B is a diagonal matrix of regression weights and C is the weights matrix for the response variables. The columns of T represent the latent vectors. The NIPALS (Non-linear Iterative Partial Least Squares) algorithm was first proposed by Wold (1966). The NIPALS algorithm was applied to the subset 3D landmarks (X_{3D-sub}) to predict the full set of 3D landmarks $X_{3D-full}$ as given in the code snippet below.

```
% Initialise u to a random vector
u = Y(:,1);
% Error checking initialisations
t_old = 1;tol = 1e-3; err = 1;
E = X; F = Y;
while (err > tol)
% Estimate the X weights
w = (X' * u) / (u' * u);
w = w / norm(w);
% Estimate the X scores
t = X * w;
% Estimate the Y weights
c = (Y' * t) / (t' * t);
% Estimate the Y weights
u = (Y * c) / (c' * c);
% regression weights to predict Y from t
b = t' * u;
%compute factor loadings for X
p = (X' * t) / (t' * t);
% Partial out the effect of t from X & Y
E = E - (t * p')
F = F - (b * t * c');
% update the corresponding vectors
W = [W w];
P = [P p];
C = [C c];
% compute error
```

```
err = norm(t_old - t) / norm(t)
t_old = t;
end
% matrix of coefficients for multivariate regression
B = W * inv(P' * W) * C';
% Estimate value of Y
Y = X3D_sub * B + F;
```

This approach yielded similarity measures of about 39% for the predicted landmarks.

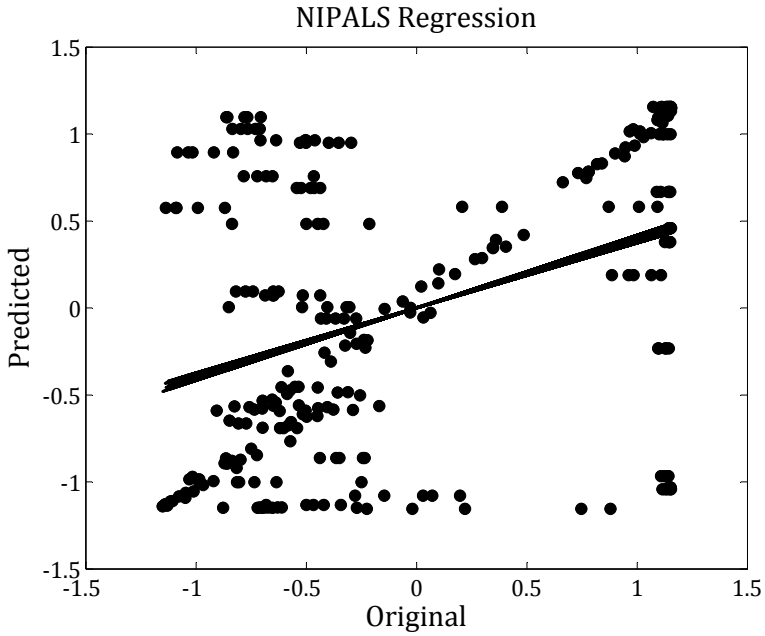

Figure 5.4: Similarity measure between full set of actual and predicted 3D landmarks for all the specimens using NIPALS regression at stage 2.

The large difference in the number of input and output variables in the second step of this method affected the predictive performance of both of these regression

techniques.

5.2.3 Morphometrics

Morphometrics is a branch of mathematical shape analysis that provides a quantitative representation of shape characteristics. Bookstein (1991); Dryden and Mardia (1998) defined morphometrics as the study of shape variation and its covariation with other variables. Traditional morphometrics (Marcus, 1990) was concerned with application of multivariate statistical analysis techniques to morphological datasets consisting of linear distance measurements such as length, width, height, etc. The analysis provided a quantitative measure of shape variation, typically as tables with lists of numbers that had to be analysed by domain specialists.

Geometric Morphometrics

Kendall (1977) defined shape as

> all the geometrical information that remains when location, scale and rotational effects are filtered out from an object.

The set of shapes, which differ only by one or more of these Euclidean transformations, are said to belong to a 'shape space'. A shape may be described by a set of landmark points that correspond to some identifiable features of the object. These landmark points match between and within populations for that object. A frame

of reference can be generated for comparison of objects within a shape space, by filtering out the translations, scaling and rotations for the objects.

Morphometric studies that focus on the geometry of a structure and the geometric properties of the co-ordinates of landmarks for quantifying and analysing shape are categorized as 'geometric morphometrics' (Rohlf and Marcus, 1993). Geometric morphometrics combine the use of multivariate statistics with visualization of the results from these analysis. These methods consider morphological data aligned to Kendall's shape space (Kendall et al., 1999) for multivariate analysis.

5.3 Summary

This chapter has looked at various concepts and methodologies involved in the estimation of the three-dimensional shape of an object given its 2-D projection. As discussed in the introduction of this chapter, several studies have used two or more projections either orthogonal or as slices, to reconstruct such a 3-D shape. The novelty of this research was to attempt the 3-D reconstruction using a single 2-D projection.

The following chapter discusses the use of geometric morphometrics as the chosen technique for the current research objective and the application of the same for building a shape template for the proximal human femur.

Chapter 6

3D reconstruction from a radiographic image: In search of the missing dimension

6.1 Overview

As discussed in the previous chapter (section 5.1), several studies have looked at reconstruction of anatomical structures from multiple CT slices as well as from multiple radiographic images. However, CT scans are expensive and involve high doses of radiation as compared to x-ray scans. The challenge for this research was the creation of a 3D shape model from a single 2D radiographic image.

It was hypothesised that a shape template could be generated for the bone, which could then be applied to a radiographic image in order to predict an approximation of its actual three-dimensional shape.

In 2006, Zheng et al. described a technique of 2D/3D reconstruction using a combination of statistical extrapolation and regularized shape deformation with an iterative non-rigid 2D point matching algorithm from input fluoroscopic images to the reconstructed model. The point matching algorithm involved symmetric nearest-neighbour mapping and 2D thin plate splines-based deformation to find best-matched pairs between the images and the model. 11 cadaveric femurs were used in the study and average reconstruction errors of 1.2mm and 1mm were obtained using 2 and 3 input fluoroscopic images respectively. Novosad et al. (2004) had used calibrated x-rays and a template 3D geometric model of the vertebrae for individual patients to reconstruct 3D models of the spine from a single x-ray image for quantitative testing of the lateral bending motion of the spine in scoliotic patients. Average root mean square errors of approximately 2.89mm were achieved using a case study of 15 patients and this error was deemed acceptable for their particular application.

6.2 Shape Template: The Concept

Consider a simple example of a cylindrical bone shaft as shown in figure 6.1:

A shape template provides the relationship between the measured dimension 'x' and the unknown depth dimension 'z' at a given slice 'i'. A set of statistical algorithms define the mapping from the 2D domain of the radiograph to the 3D domain of the bone (Figure 6.2). This makes it possible to describe the 2D projected image into a 3D voxel map using a predicted tissue depth 'z'.

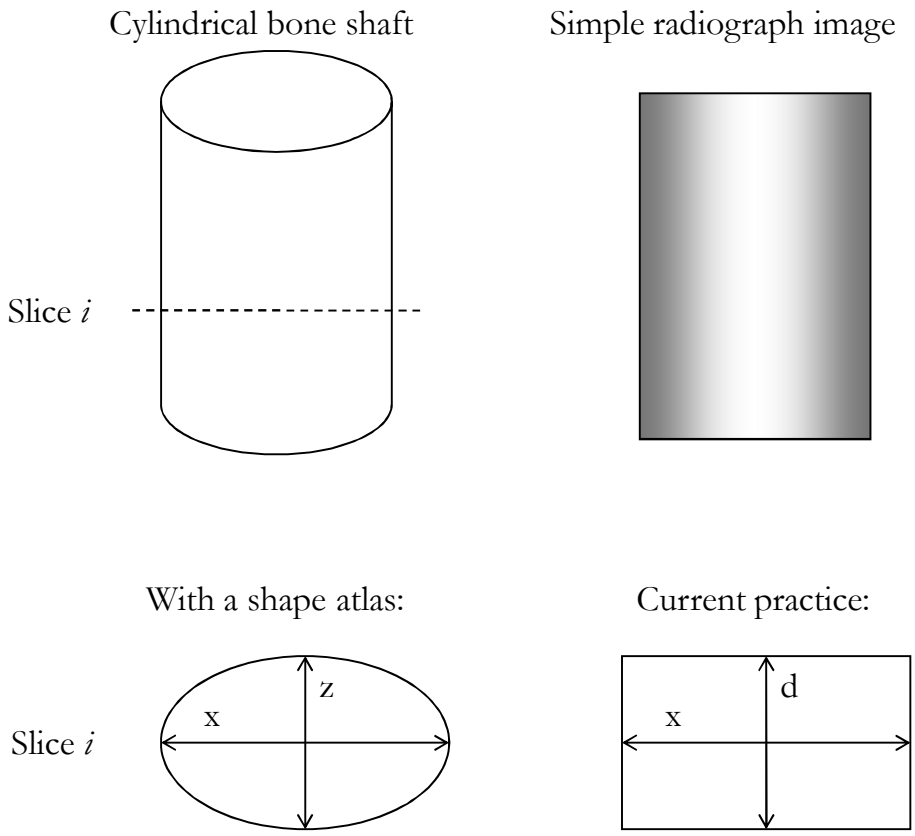

Figure 6.1: The shape template concept

6.3 Methodology

6.3.1 Building the bone database

Three sets of femora, each scanned by computed tomography (CT) on different machines (because of a change in location and equipment upgrade), were studied: one was examined as part of a previous study (Keyak et al., 2005) at the University of California, San Francisco (UCSF set: 18 femora from 8 males and 10 females; age, 52 - 92 years); and two were examined at the University of California, Irvine

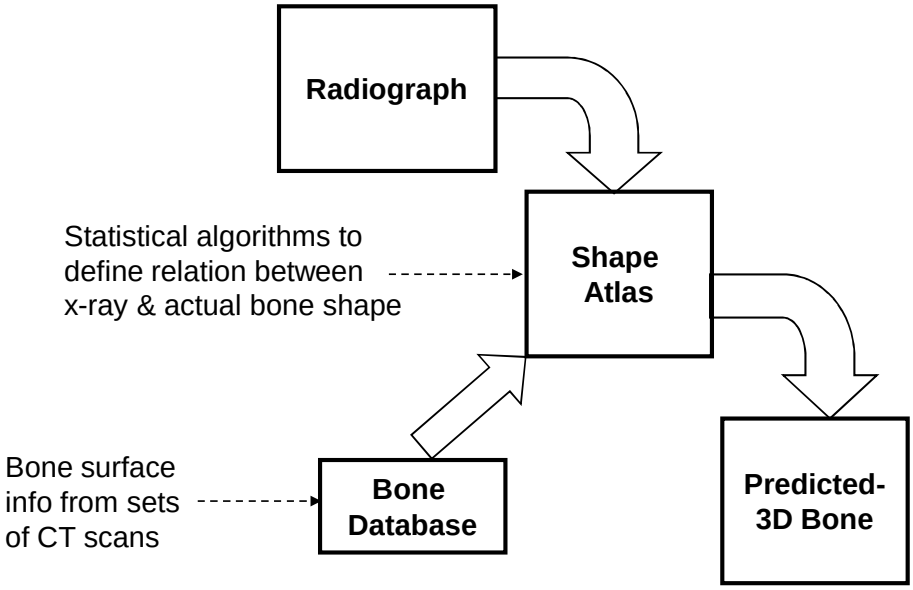

Figure 6.2: Overview of shape template application

(UCI1 set: 14 femora from 8 males and 4 females; age, 53 - 88 years; and UCI2 set: 11 femora from 11 female donors; age, 45 - 94 years).

Of these, UCI1 and UCI2 datasets had CT voxel resolutions of 0.67mm and the UCSF dataset had a voxel resolution of 1.06mm. The CT scans had 3mm slice thickness. For each femur, a virtual radiograph was generated as a simple axial projection of the object reconstructed from the CT slices. Two-dimensional projections describing 'offset' and 'depth' were also generated such that they described the 3D spatial arrangement of the bone surface voxels.

CT scanning (Keyak et al., 2005)

Preparation of femora for CT scanning was identical, regardless of data set. Each femur was immersed in water and placed atop a calibration phantom for CT scanning. Each set of femora was scanned on a different CT scanner and used slightly different scanning parameters.

The UCSF femora were scanned on a GE 9800 Research Scanner (GE Healthcare Technologies, Waukesha, WI) with a K_2HPO_4 (KHP) calibration phantom (Lang et al., 1991), 320 320 matrix, and 1.08mm pixels. The UCI1 femora were scanned on a GE HiSpeed Advantage CT scanner (GE Healthcare Technologies, Waukesha, WI) with a calcium hydroxyapatite (CHA) phantom (Image Analysis, Inc., Columbia, KY), 512 512 matrix, and 0.674mm pixels. The UCI2 femora were scanned on a GE CTI scanner (GE Healthcare Technologies, Waukesha, WI) with a CHA phantom, 512 512 matrix, and 0.674mm pixels. All scans were obtained using 80 kVp, 280 mAs, 3mm slices and standard reconstruction.

6.3.2 2D Mappings

A ray casting technique was applied to the CT scan data for each proximal femur thereby creating 2D mappings of 'BMD', 'offset' and 'depth'. The mappings express the data as 256 level grey-scale bitmaps, shown in Figure 6.3.

For a column in a slice of the CT scan, 'offset' was defined as the number of voxels from the edge of the slice to the first bone voxel in that column. 'Depth' was defined as the number of voxels from the edge of the slice to the last bone voxel along the

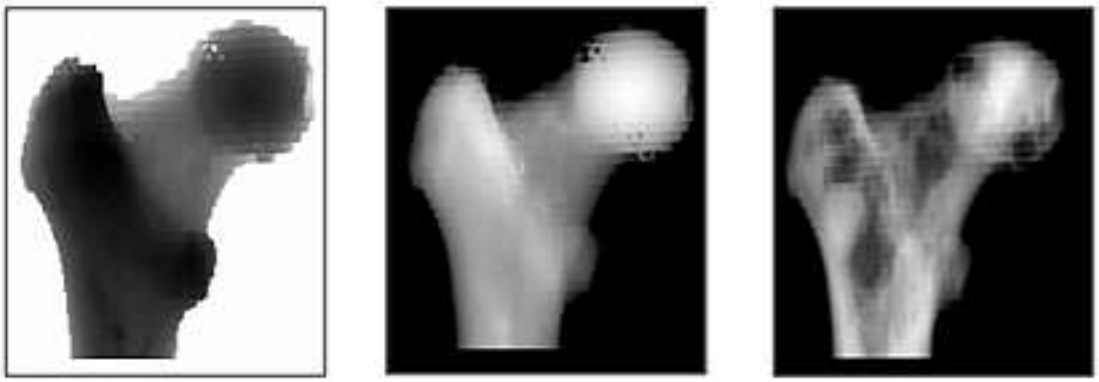

Figure 6.3: 2D ray casting mappings of offset and depth expressed as 256 level greyscale images. Note that the femoral head and greater trochanter correspond to minimum offset but maximum depth.

particular column (see Figure 6.4). The depth map provided information about bone thickness at each pixel of a projected 2D radiograph image and the offset map provided the relative position of each part of the bone in the 3^{rd} dimension, hence accounting for the protruding trochanteric section as well as the head anteversion.

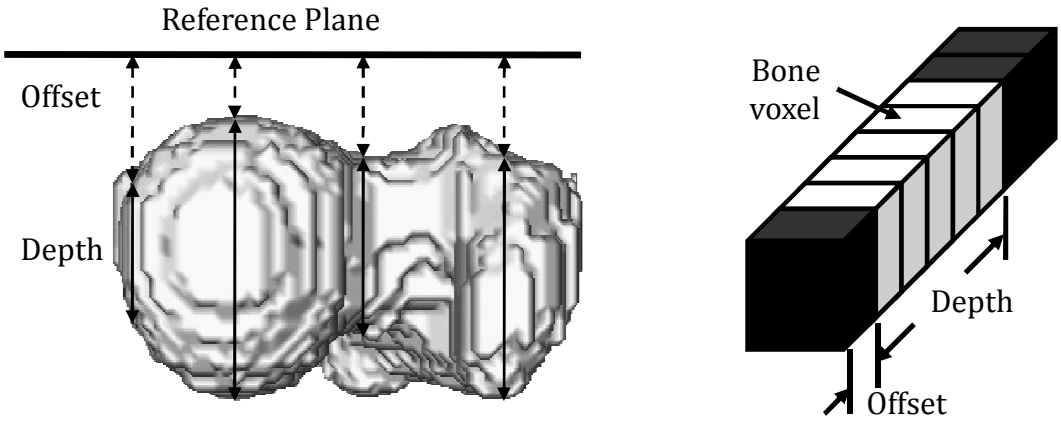

Figure 6.4: Offset and depth mapping

6.3.3 Input Registration

As discussed in the previous chapter, geometric morphometrics attempts to quantify the structure and geometric properties of a shape using a set of co-ordinates of landmarks on the shape. Hence the first step in geometric morphometrics is the acquisition of landmarks for the shapes being analysed. Landmarks have been defined (Zelditch et al., 2004) as

> discrete homologous anatomical loci that do not alter their topological positions relative to other landmarks, provide adequate coverage of the morphology, can be found repeatedly and reliably, and lie within the same plane.

Landmarks are typically chosen to quantify at least all the visible shape features required for analysis.

The figure 6.5 shows landmarks digitized along the outline of a radiograph image of the human proximal femur.

The landmarks in this case were chosen to provide an optimal number of visually recognizable points to describe the overall shape of the femur. Homology had to be ensured while selecting these landmarks for the various specimens and hence the landmarks had to be clearly distinguishable along the image outline. Each radiographic projection in the input dataset was described by a 'landmark configuration'.

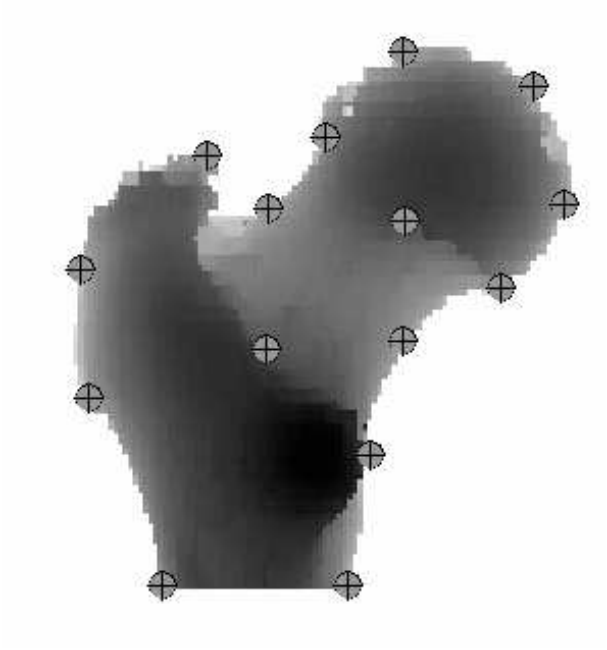

Figure 6.5: Landmarks on a femur radiograph

A 'landmark configuration' is a set of landmark co-ordinates for a particular specimen with 'K' landmarks and 'M' dimensions for each landmark.

$$X_i = \begin{bmatrix} x_{11} & x_{12} & ... & x_{1M} \\ x_{21} & x_{22} & ... & x_{2M} \\ ... & ... & ... & ... \\ x_{K1} & x_{K2} & ... & x_{KM} \end{bmatrix} \tag{6.1}$$

The set of all landmark configuration matrices having the same number of landmarks and co-ordinates (KxM) form the 'configuration space'.

Generalised Procrustes Analysis (GPA) was employed to filter out the Euclidean variations among the samples in the dataset and consider each projection invariant of its translational, rotational and scaling effects. This procedure was applied

simultaneously to the virtual radiographs as well as the offset and depth maps.

Generalised Procrustes Analysis (GPA)

In order to compare and study the variation in shape among various specimens, it is necessary to consider them in an aligned framework. Zelditch et al. (2004) discusses the various registrations techniques proposed and their limitations. The current widely accepted method for superimposition of landmarks is the Procrustes superimposition. Procrustes analysis is the name for the process of performing a shape-preserving Euclidean transformation to a set of shapes. This removes variations in translation, rotation and scaling across the data set in order to move them into a common frame of reference.

The name of the method comes from the story of Procrustes in Greek Mythology. Procrustes, a name that literally means 'one who stretches', was a bandit who invited passers-by to rest on a magical iron bed that would fit any guest. He then either stretched the guests or cut off their limbs to make them fit perfectly into the bed. Theseus, a traveller to Athens, cut off the evil-doer's head to make him fit into the bed in which many 'guests' had died (Encyclopdia Britannica, 2007).

The Procrustes superimposition in geometric morphometrics is based on alignment using simple operations such as translation, scaling and rotation, to minimize the partial Procrustes distance between corresponding landmarks. The partial Procrustes distance is calculated as the sum of the squared distances between corresponding landmarks after these operations have been performed. By definition (Kendall et al., 1999), this is the minimum distance between the shapes in the shape

space.

The steps for generalised Procrustes superimposition as proposed by Rohlf (1990) are summarized below:

1. **Translation**: First of all, the centroid for each landmark configuration is calculated as the mean of its co-ordinates.

$$C_j = \frac{1}{K}\sum_{i=1}^{K} x_{ij},\ j = 1 : M \tag{6.2}$$

where C_j is the j^{th} component of the centroid. Each configuration of landmarks is then centred by subtracting the co-ordinates of its centroid from the corresponding co-ordinates of each landmark.

$$Centred\ shape, X_c = \begin{bmatrix} (x_{11} - C_1) & (x_{12} - C_2) & ... & (x_{1M} - C_M) \\ (x_{21} - C_1) & (x_{22} - C_2) & ... & (x_{2M} - C_M) \\ ... & ... & ... & ... \\ (x_{K1} - C_1) & (x_{K2} - C_2) & ... & (x_{KM} - C_M) \end{bmatrix} \tag{6.3}$$

2. **Scaling**: Centroid size is calculated as the square root of the sum of the squared distances of the landmarks from the centroid.

$$CS(X) = \sqrt{\sum_{i=1}^{K}\sum_{j=1}^{M}(x_{ij} - C_j)^2} \tag{6.4}$$

Each landmark configuration is scaled to unit centroid size. These new configurations are called centred pre-shapes (Dryden and Mardia, 1998).

$$Centred\ pre - shape = \frac{1}{CS(X)}[X_c] \tag{6.5}$$

3. **Rotation**: To start with, one of the centred pre-shapes is chosen at random (generally the first one in the set) as the reference configuration. All other

configurations are rotated to minimize their individual partial Procrustes distance with the reference configuration. The rotation matrix is computed using singular value decomposition (Rohlf, 1990):

$$SVD(X_R^t X_T) \tag{6.6}$$

where X_R is the reference shape and X_T is the target shape, i.e., the shape that is being rotated. The superscript ^{t} denotes transpose of the matrix.

Once all the configurations had been rotated to the reference shape, the average shape is calculated and designated as the new reference shape. All configurations are then rotated to optimal alignment with this new reference shape.

Figure 6.6 illustrates this process - the input landmarks as shown on the left are scaled, translated and rotated to produce the GPA-registered landmarks shown on the right. The scatter of points at each landmark denotes the variability among the samples.

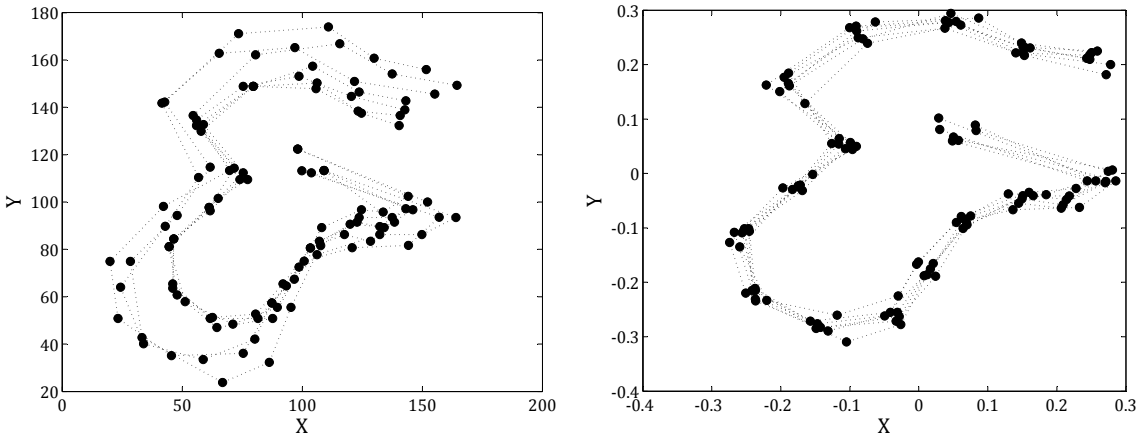

Figure 6.6: Input and GPA-aligned landmarks

6.3.4 Thin Plate Splines

Thin Plate Splines (TPS) help to visualize shape changes over the entire form instead of just the relative changes at landmark positions, as obtained from GPA. The deformation is expressed as a continuous function that maps corresponding points between shapes.

Bookstein (1989) proposed the concept of visualizing the deformation from one shape to another using a uniform and infinitely thin idealized steel plate. The displacements of the landmarks in a two-dimensional plane are visualized as if they were transferred to the third dimension. Thus, the steel plate is bent to conform to the relative displacements at each landmark and the distance between the landmarks in the plane. The bending energy is defined (Bookstein, 1989) as a function of the rate of change in the slope of the bent plate. Large changes in displacements between closely-spaced points lead to an increase in slope, thereby requiring more energy to bend the plate. Hence, minimizing the bending energy minimizes localized variations among the shapes. The D'Arcy Thompson grid (Thompson, 1942) is often used to visualize thin-plate splines (6.7).

The thin-plate spline approximates the deformation between shapes using a smooth interpolating function of a linear combination of components that describe the patterns of relative landmark displacement. The components that describe the non-uniform deformation are called 'partial warps' (Slice et al., 1996). The kernel function used for the thin-plate spline interpolation is given as (Bookstein, 1989; Zelditch et al., 2004):

$$z(x, y) = U(r) = r^2 \ln r^2 \tag{6.7}$$

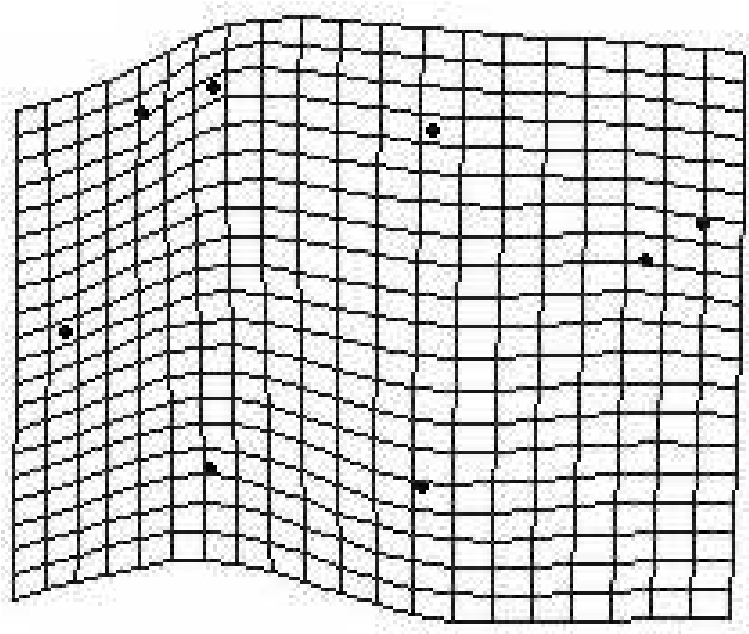

Figure 6.7: Thin Plate Spline sample

for two-dimensions and

$$U(r) = |r| \tag{6.8}$$

for three-dimensional shape analysis; where r is the distance between a pair of landmarks between the reference and target configurations and U is said to be the fundamental solution of the biharmonic equation for the shape of a thin steel plate lifted to a height z(x,y) above the (x,y)-plane.

For a two-dimensional case, the deformation at any point (x, y) in the plane is given by the following linear combination (Bookstein, 1989):

$$f(x, y) = a_1 + a_x x + a_y y + \sum_{i=1}^{K} w_i U(|P_i - (x, y)|) \tag{6.9}$$

where f is the spline function describing the deformation in the target shape with respect to the reference form, the P_i terms denote the landmarks in the reference configuration, the w_i are weights for the U function and the a terms describe the uniform components in the deformation.

The computation of the bending energy matrix and the partial warps and partial warp scores has been described in detail by Bookstein (1989) and Zelditch et al. (2004).

Prediction of three-dimensional shape using thin plate splines for deformation of an average shape grid is described in detail in the next section.

Creating the template using Thin Plate Splines

Generalised Procrustes Analysis (GPA) and Thin Plate Splines (TPS) were combined into a single technique to create the shape template for the proximal femur. GPA was utilised to create an average 3D 'Proximal Femur Training Template' that could be expanded or contracted to suit the size and shape of an individual 2D 'Test' radiographic image. TPS deformation was applied to warp the 2D contour to match the radiographic projection of each input bone. This approach assumes that there is a proportional change in bone depth (z) corresponding to a proportional change in overall size of the bone.

First of all, 3D grids to describe the shape of the bone (see Figure 6.8) were built by merging the offset and depth maps generated as explained in section 6.3.2.

Figure 6.8: 3D grid formed by merging offset and depth maps

The TPS deformation was carried out in two stages. In the first stage, Thin Plate Splines were used to compute the deformation from the landmark configuration for each individual bone to the mean configuration. As discussed above, the thin plate spline approximates the deformation between shapes using a smooth interpolating function of a linear combination of components that describe the patterns of relative landmark displacement. The transformation matrix obtained in the first stage was applied to the offset and depth map for each femur, thus warping it to the mean shape. The resulting images were then averaged to create the average offset and depth maps.

The input dataset was randomly split into a 'Training' and 'Test' set. The shape template was derived from the Training set of CT scans of 23 excised human proximal femora. For each of these, 2D projection maps describing depth and offset from a reference plane, were derived. Defined anatomical landmarks were applied to each projected 2D shape and the mean landmark configuration computed using

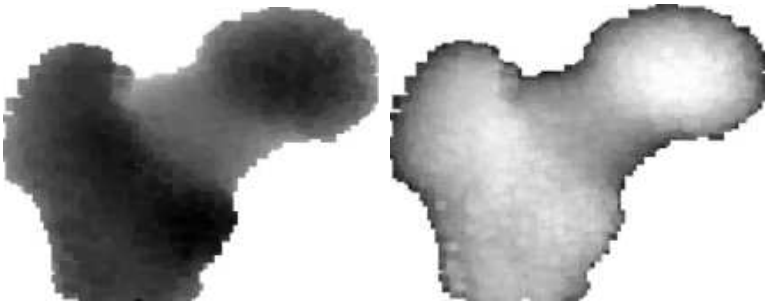

Figure 6.9: Template offset and depth maps

Generalized Procrustes Analysis. 3D grids were derived for each femur by combining the corresponding depth and offset maps. Each 3D grid was then transformed to the mean landmark configuration using Thin Plate Spline deformation. The 3D shape template was calculated as the mean of these transformations. This process of constructing the shape template for the training set is shown in Figure 6.10.

6.3.5 Applying the template

The Test population consisted of 21 femoral CT scans, from which 2D shape projection images were derived and landmarked. For each Test case, the mean landmark configuration was first aligned to the landmark configuration for the Test 2D radiographic image using GPA. The 3D 'Proximal Femur Training Template' was then warped using TPS to reflect the 2D contour deformation from the mean to the Test case, resulting in the creation of 3D model for each Test image. This process is described by Figure 6.11.

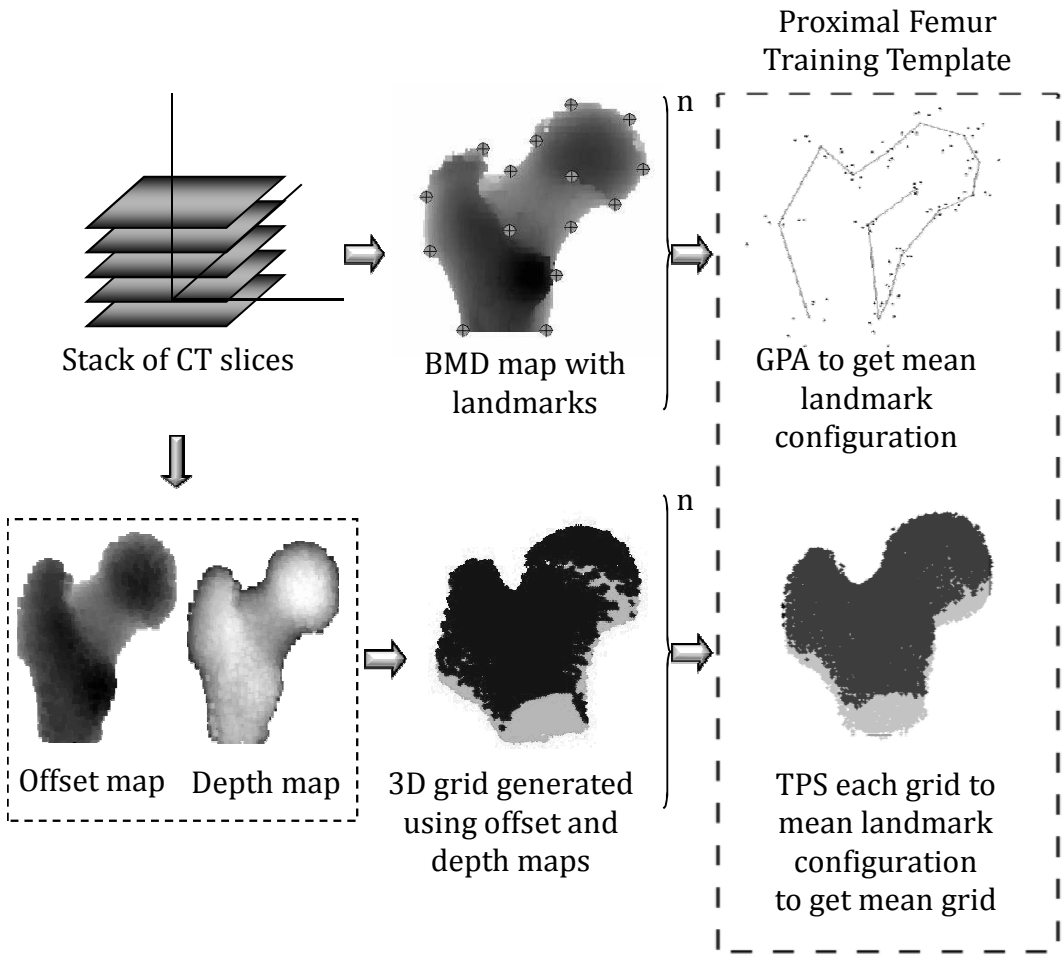

Figure 6.10: Overview of training template creation

6.4 Results & Discussion

Utilising the 2D similarity measure described in section 5.2.2, the shape-template technique was found to have an accuracy of 99.75%. Thus the 2D profile of the reconstructed shape was found to be a near-perfect match to the input radiograph. (See Figure 6.12.)

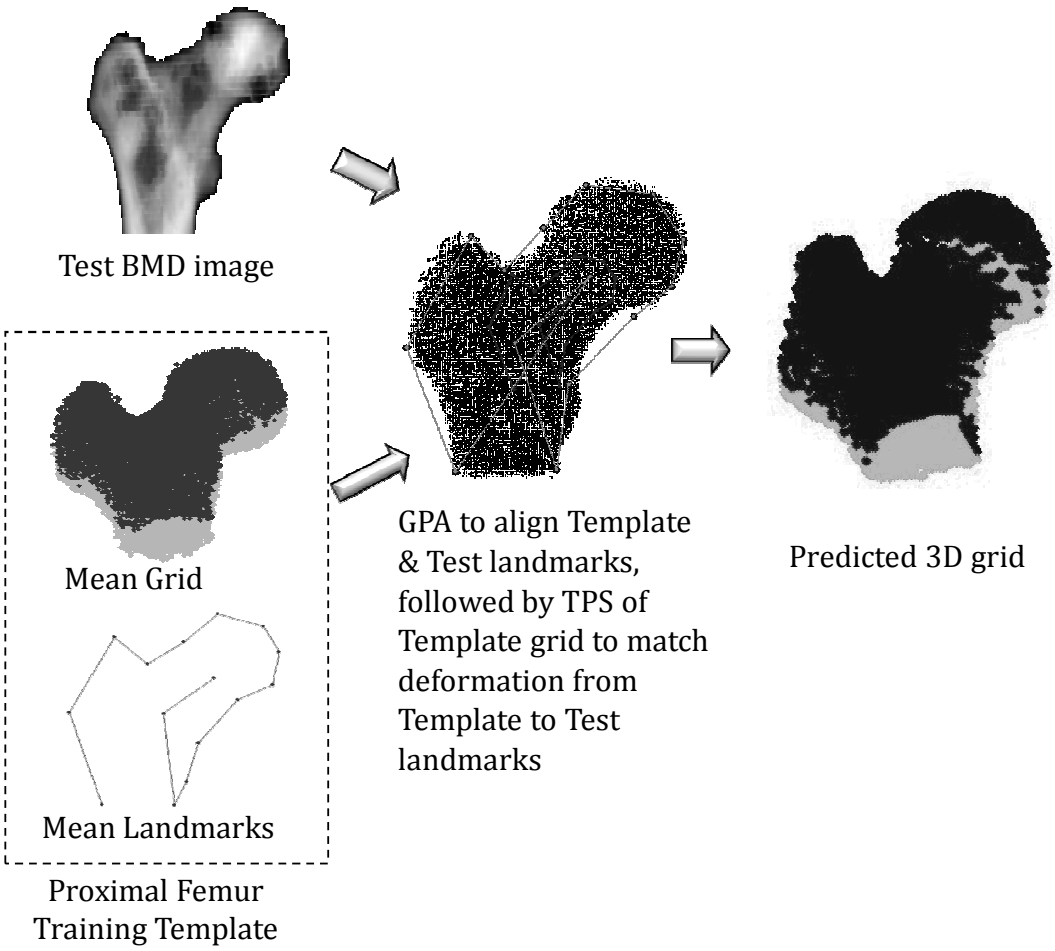

Figure 6.11: Transformation of the 3D Shape Template to an individual 2D radiographic projection to create an individual 3D model.

2D error maps for depth and offset were computed as the per-vertex average of distances in 3D space between the predicted and original maps.

$$E = \frac{1}{p} \left| \begin{pmatrix} x_{i,predicted} \\ y_{i,predicted} \\ z_{i,predicted} \end{pmatrix} - \begin{pmatrix} x_{i,original} \\ y_{i,original} \\ z_{i,original} \end{pmatrix} \right| \tag{6.10}$$

The average depth and offset errors and their respective standard deviations are listed in Table 6.1.

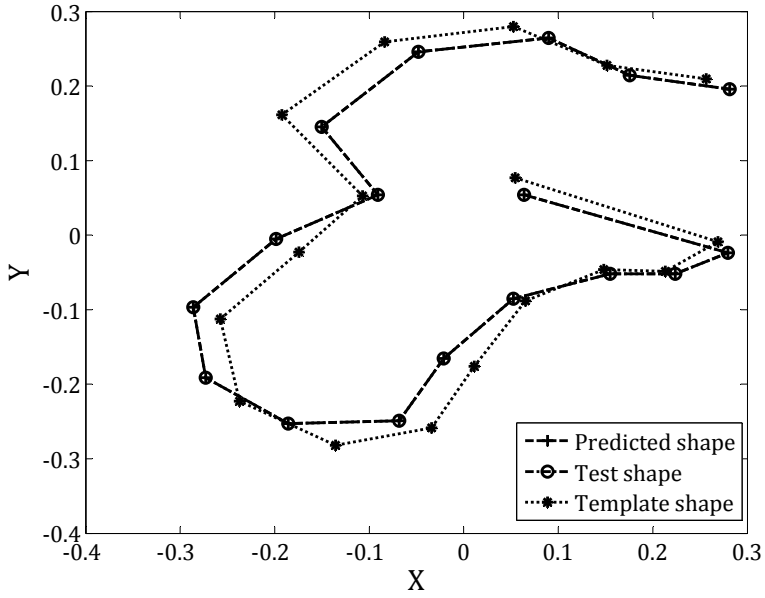

Figure 6.12: Superimposition of 2D landmarks of original and predicted shapes. Dotted line shows the contour of the template shape which was warped to fit the test case.

As seen from the error maps (see Figure 6.13), most of the depth error seems to be along the contour and these edge artefacts in the transformation of the 2D radiographic image to 3D were consistent across all Test cases.

Also, the errors in depth prediction were found to be directly proportional to a change in the ratio of bone length and width to bone depth; however no definite relation could be formulated to compensate for this discrepancy. The errors in offset prediction were attributed to the possible differences in the spatial orientations of the original and predicted shapes. The orientation of the predicted shape was dependent on the averaged grids generated using GPA and TPS on the grids in the Training set.

Table 6.1: Mean and standard deviation values for depth and offset errors for N=25 proximal femurs

	Datasets	
	UCI1 + UCI2	UCSF
Matrix size	512 x 512	320 x 320
Pixel resolution (mm)	0.674	1.08
Mean Depth (mm)	33.84	22.35
SD Depth (mm)	6.37	1.74
Mean Offset error (mm)	1.33	2.97
SD Offset error (mm)	0.53	1.30
Mean Depth error (mm)	1.73	3.40
SD Depth error (mm)	0.51	1.45
Mean Depth error (pixels)	2.56	3.15
SD Depth error (pixels)	0.79	1.34

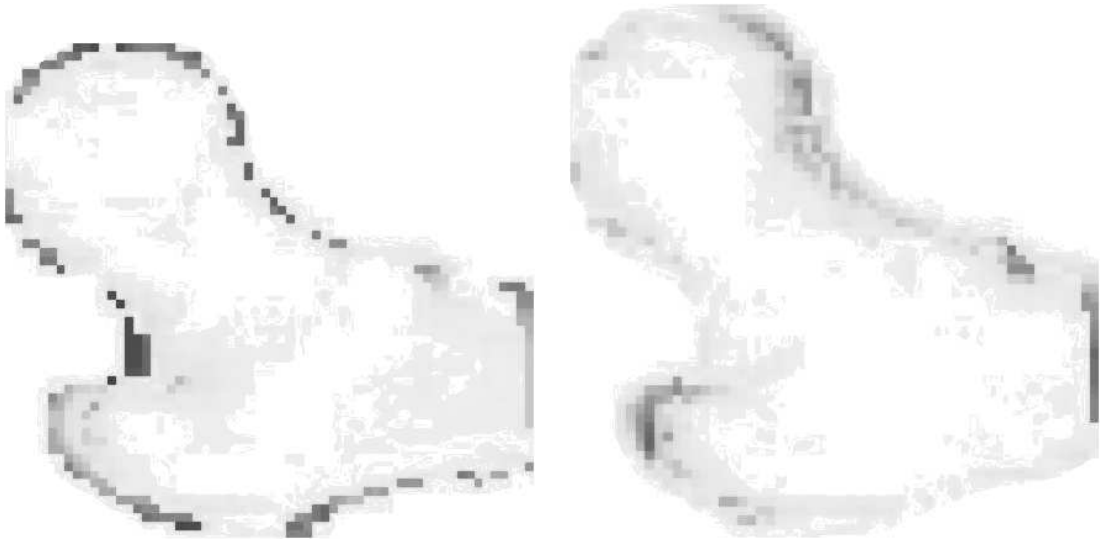

Figure 6.13: Offset and depth error maps - darker shades indicate higher error and vice versa

Figure 6.14 shows a superposition of the 3D shapes from the original CT slices and the one predicted using the shape template.

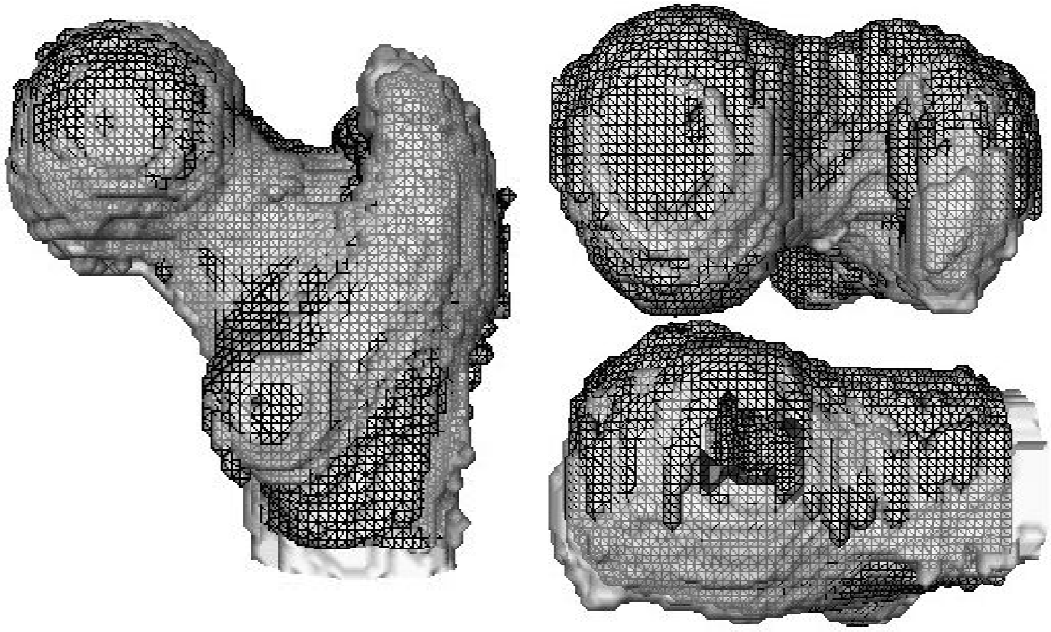

Figure 6.14: Original (light) and Predicted (dark) bones

The advantage of this technique was that the 2D projected contour of the predicted shape was nearly identical to the contour of the input test image. The assumption here was that the change in bone depth corresponds to a proportional change in bone length and breadth. This proved a drawback in the case of small stocky bones and long slender bones at opposite ends of the spectrum. However, for a majority of the cases, the assumption that the bone depth could be predicted from its length and breadth proved reasonable.

This project has demonstrated the potential for creation of a 3D shape model for the proximal femur from a single 2D radiographic image such as a DXA scan image. Applications include derivation of volumetric density from areal bone mineral density

and 3D finite element analysis for prediction of the mechanical integrity of the proximal femur. The next chapter explains how these predicted 3D bone models were used for bone strength assessment using FEXI.

Chapter 7

Shape Atlas Application to FEXI

7.1 Introduction

The preceding chapter discussed the reconstruction of the three-dimensional shape of the human proximal femur from a radiograph of the same. An application of the reconstructed shape for bone stiffness assessment is discussed in this chapter. For this, finite element analysis to simulate compressive mechanical loading was performed with the reconstructed bone to compute bone stiffness.

Cody et al. (1999) used quantitative computed tomography (QCT) for 3D modelling of the femur for finite element analysis to prove that finite element analysis would provide a better prediction of bone strength than conventional DXA. This study used load and gait configurations causing femoral neck fractures and found that finite element analysis provided a better prediction of fracture load and stiffness compared to QCT and DXA.

Lotz et al. (1991) used linear finite element analysis of 3D modelled bones to predict the fracture load for the proximal femur, which was later improved upon by (Keyak, 2001) using non-linear finite element models. Lotz used three-dimensional finite element models of the proximal femur (with geometries and material properties based directly on quantitative computed tomography) to compare predicted stress distributions for one-legged stance and for a fall to the lateral greater trochanter. In Keyak's study, the models were extended to include non-linear material properties for the cortical and trabecular bone.

The FEXI technique (see section 2.4.4) uses finite element analysis to measure the stiffness of bone in the presence of a compressive mechanical force. The initial version of this technique assumed constant tissue depth across the bone and considered the bone as a thin plane stress model. A more accurate model for the finite element analysis, and hence bone stiffness prediction, required modelling the bone with a better understanding of tissue depth across the plane. As described in the previous chapter, a shape atlas was developed for the proximal femur to provide this information about the anatomical structure of the bone.

The following sections describe the application of the FEXI technique to predicted 3D bone models to estimate bone strength and compares the results to mechanical test results as well as computed stiffness data from 3D finite analysis of bone models created from the original CT slices. The first section describes the methodology for FEXI implementation and the following section look sat a comparison study of FEXI with BMD and CT-derived finite element analysis data. The dataset used was the same as that used in the previous chapter and aimed to examine the performance of 3D FEXI applied to the bones constructed using the shape template.

7.2 Methodology

Adopting a fundamentally similar methodology to 2D-FEXI, a finite element model was created from platened x-ray image using a bespoke MATLAB program. The grey level at each pixel was mapped to BMD using regression data from BMD values obtained from a DXA scan of the bone.

7.2.1 Conversion of 2D Grey Level into BMD

The ray casting technique was further applied to the CT scan data in order to provide a 'BMD' mapping. This was performed for each 3D voxel via two-part regression manipulation:

1. Conversion of [KHP] into ash density:

   Volumetric data from the CT scans was converted from Hounsfield Units (HU) to bone density (gcm^{-3} KHP) using values from the calibration phantom (see Section 6.3.1). This KHP density was then converted into bone ash density (gcm^{-3}). The bone ash density gives the mineralized bone non-organic density (Ding, 2000), and is given by ash weight divided by volume of the specimen. The conversion to ash density was utilized to compute the Young's modulus for the bone voxels. The conversion from KHP bone density to ash density was accomplished using the relation described by Les et al. (1994).

   $$\rho_{ash} = 0.0526 + 1.22\rho_{KHP} \tag{7.1}$$

2. Conversion of ash density into QCT density (gcm^{-3}):

The computed ash density was also converted (using the relation specified by Kaneko et al. (2004)) into QCT density to facilitate estimation of BMD for the bone.

$$\rho_{QCT} = 1.1292\rho_{ash} - 83.19 \tag{7.2}$$

The bone mass for each 3D voxel is the product of its QCT density and depth. By dividing the sum of bone masses along the line of voxels normal to each 2D pixel coordinate by the pixel cross-sectional area yields the BMD for that pixel. Averaging the individual pixel BMD values over the corresponding region of interest yields the 'Total Area BMD' for a proximal femur.

7.2.2 3D FEXI

When performing the 3D FEXI analysis, a constant volumetric density (CVD) was allocated to each voxel along the line normal to each 2D pixel coordinate as the value calculated by dividing the pixel BMD by the corresponding bone depth. The Young's modulus for each voxel was again derived via the two-part regression manipulation:

1. Conversion of constant volumetric density (CVD) into ash density: (Kaneko et al., 2004)

$$\rho_{ash}\ (gcm^{-3}) = 69.8 + 0.839 * CVD \tag{7.3}$$

2. Conversion of ash density into Young's modulus: (Keyak et al., 2005)

$$E\ (MPa) = 14900\rho_{ash}^{1.86} \tag{7.4}$$

noting that this equation corresponds to a sample that contains both trabecular and cortical bone.

A constant Poisson's ratio of 0.4 was assumed.

The predicted three-dimensional femur model was stored as a discrete regular 3D voxel map. A bespoke computer program was written in MATLAB (Mathworks Inc., MA) to convert the 3D voxel map into a finite element model that demonstrated the chosen orientation, restraint and loading scenario to be considered. The finite element analysis was performed using ANSYS (ANSYS Inc., PA).

7.2.3 2D FEXI and 2.5D FEXI

2D FEXI derived stiffness was derived in a similar manner to the 3D FEXI analysis, except that a constant bone depth of 25 mm was adopted for all 2D pixel coordinates.

A modified version of 2D FEXI, named 2.5D FEXI, was defined to use bone depth information from the predicted depth map. In this case, the volumetric density at each pixel location (x, y) was computed using the predicted depth at that location.

Volumetric density,

$$\rho = \frac{areal\ BMD}{d}$$

For 2D FEXI: $d = 2.5cm$, and
For 2.5D FEXI: $d = D(x, y)cm$, where D represents the depth map for the bone at location (x,y)

The finite element analysis for 2.5D was using 2D elements rather than 3D. The predicted depth was simply utilised to calculate a volumetric density corresponding to each 2D pixel.

7.3 Comparison of aBMD, 3D FEA and FEXI to predict the experimental failure load of the proximal femur

7.3.1 Samples

The objective of this study was to compare the ability of bone mineral density (BMD) along with 2D, 2.5D and 3D FEXI to accurately predict the stiffness of the proximal femur derived from conventional 3D finite element analysis (FEA).

The source data consisted of CT scans of 18 excised proximal femora from the UCSF dataset described in section 6.3.1. Following CT scanning, they were experimentally compression tested in a 'stance' loading scenario to derive mechanical stiffness and failure load.

Stance loading scenario

The 'stance' loading condition represented a subject in the standing position. The femoral head was loaded with the distal end of the shaft restrained in all directions. The shaft axis of the proximal femur was orientated at an angle of 70^o to the ground. A resin support platen was applied to the base of the shaft portion to apply the restraints. A resin load platen was moulded to match the shape of the femoral head and used to provide uniform loading at the head. The stance loading configuration is shown in figure 7.2. A vertical load of 1kN was applied to the loading platen which was restrained to only allow vertical displacement. Dividing the applied load by the resultant platen displacement yielded the stiffness of the bone ($\mathrm{N}mm^{-1}$).

7.3.2 Mechanical Test

All specimens were thawed and mechanically tested to failure using identical procedures (see Figure 7.1). The distal end of each proximal femur was embedded in a polymethylmethacrylate (PMMA) block that was used to restrain the femur during mechanical testing and served as a fixed reference coordinate system for the FE models. A custom PMMA cup was moulded, but not bonded, to the top of each femoral head. This cup was used during mechanical testing to distribute the applied load. Displacement was applied to the femoral head at 0.5 mm/s using a servo-hydraulic testing machine (MTS 858 Test System; MTS, Eden Prairie, MN). The PMMA cup that was custom moulded to each femoral head was used to distribute the load over a 3cm-diameter circular region.

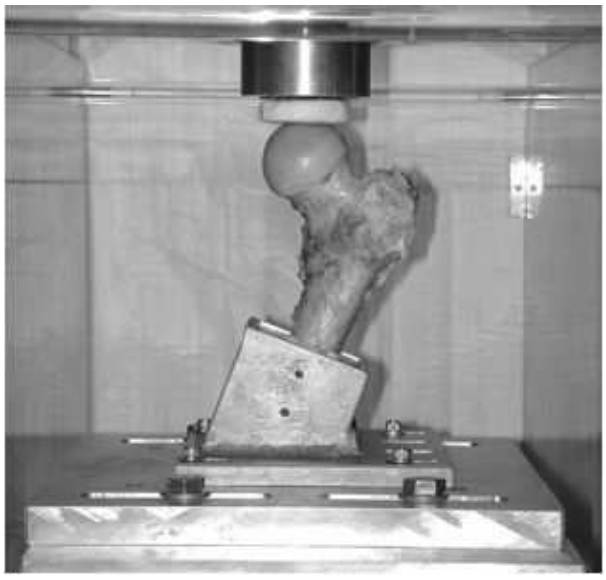

Figure 7.1: The mechanical test setup - *By kind permission of Joyce Keyak, University of California, USA*

7.3.3 3D FEA

Three-dimensional FE models with 3mm linear cube-shaped elements and non-linear isotropic mechanical properties were generated from the CT scan data.

Ash density (ρ_{ash}, gcm^{-3}) of each element was computed from the calibrated CT scan data using the following relationship (Les et al., 1994):

$$\rho_{ash} = 0.0526 + 1.22\rho_{KHP} \tag{7.5}$$

The elastic modulus (E, MPa) of each element was calculated using relationships with ρ_{ash}.

$$E\ (MPa) = 14900\rho_{ash}^{1.86}; \quad for\ trabecular\ and\ cortical \tag{7.6}$$

A constant Poissons ratio of 0.4 was assumed.

The boundary conditions for the FE models represented the conditions that would be applied during mechanical testing, with precise loading conditions derived from the coordinate system of the PMMA block in which the distal end of the specimen was embedded. Displacement was incrementally applied to nodes within a 3cm-diameter region on the femoral head and directed at 20^o to the shaft in the coronal plane; translation perpendicular to this displacement was unconstrained. Elements containing these nodes were assigned an elastic modulus of 20 GPa and a strength of 200 MPa to prevent severe element distortion. Nodes on the distal end of the model were fully restrained. Finite element analysis was done with ABAQUS v6.3.1 (Abaqus, Inc., Pawtucket, RI, USA). For each incremental displacement, reaction forces were computed at the displaced nodes on the femoral head.

7.3.4 FEXI implementation

Finite element analysis for 3D FEXI, 2.5D FEXI and 2D FEXI were implemented in a similar manner to the experimental mechanical test and 3D FEA, namely, the models were orientated such that the femoral shaft was aligned at an angle of 20^o to the coronal plane without anteversion of the femoral neck. An illustration of the 3D FEXI model is shown in Figure 7.2. A simulated steel support platen ($E = 200GPa$, $\nu = 0.3$) was incorporated at the bottom of the femoral shaft and restrained in all three orthogonal directions. A horizontal simulated steel loading platen was incorporated at the top of the femoral head. A resin platen ($E = 7.163GPa$, $\nu = 0.3$) was moulded to the top of the femoral head for uniform distribution of the applied load. The loading platen was restrained such that it could only move within the vertical direction. Within the finite element model, a vertically downwards load of 1kN was applied evenly over the upper surface of the loading platen.

The voxel sizes for the predicted bone models were computed from the CT slice thickness and pixel resolution. Hence for the UCI1 and UCI2 datasets, the voxel sizes were 0.674mm x 0.674mm x 3mm; and for the UCSF dataset, the voxel resolution was 1.08mm x 1.08mm x 3mm. Finite element analysis was carried out using ANSYS which had a finite element node limit of 127000 nodes for the academic licence that the author's university owns. Hence the voxel maps describing the bone models were trimmed and resampled to half the original resolution for the UCI1 and UCI2 datasets and 0.8^{th} of the original resolution for the UCSF dataset. The finite element models were generated from these resampled voxel maps using a bespoke application written in MATLAB.

Figure 7.3 shows the resultant 3D-FEXI finite element solution.

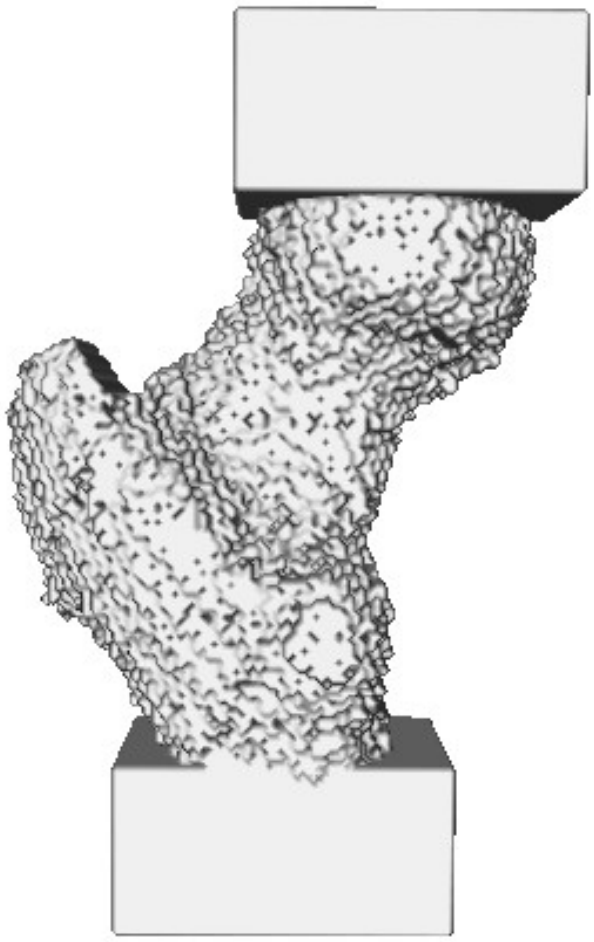

Figure 7.2: The 'Stance' loading condition

Following solution of the finite element analysis of the femoral model, the 3D FEXI derived stiffness (Nmm^{-1}) was calculated as the applied load divided by the vertical displacement of the loading platen.

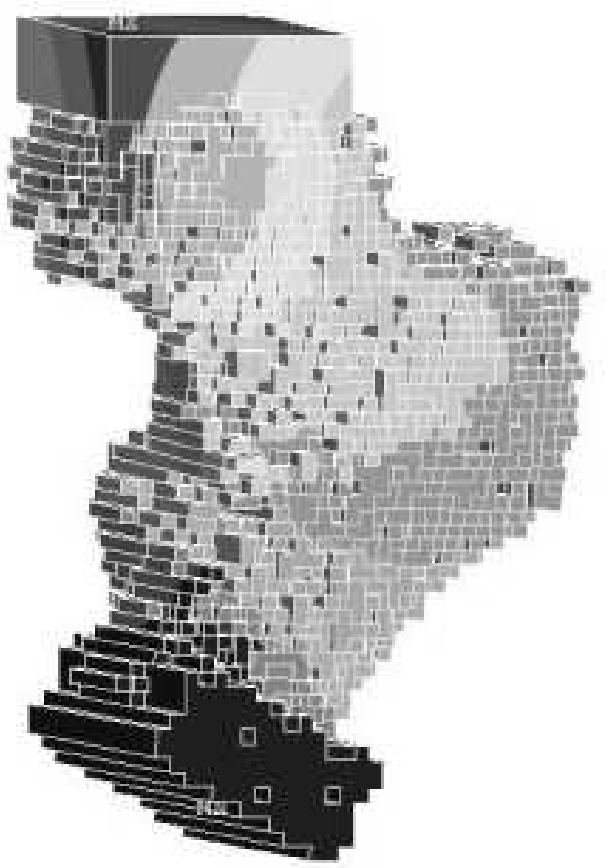

Figure 7.3: Displacement plot for 3D FEXI in stance loading

7.4 Results & Discussion

Regression plots for the prediction by BMD, 3D FEA, and the three FEXI formats of the experimental mechanical failure load of the proximal femur are shown in Figure 7.4.

3D FEXI provided a significantly higher correlation ($R^2 = 0.85$) with conventional CT derived 3D finite element analysis than achieved with BMD ($R^2 = 0.52$), 2D FEXI ($R^2 = 0.44$) and 2.5D FEXI ($R^2 = 0.45$).

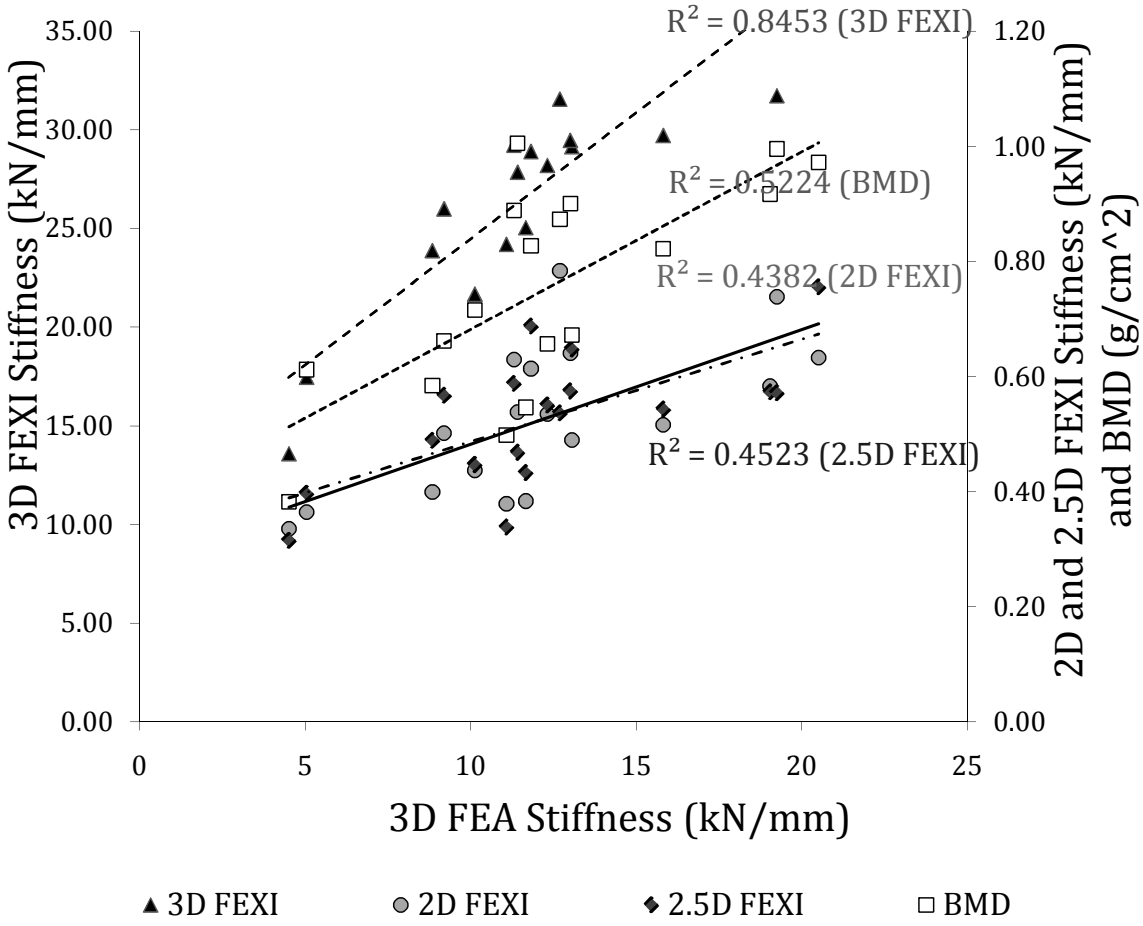

Figure 7.4: Correlation of Stance stiffness for 3D, 2D, 2.5D FEXI, and BMD with stiffness obtained from 3D FEA from CT

The correlation (Figure 7.5) of 3D FEXI with measured mechanical strength (R^2 = 0.80) was marginally better than CT-derived FE stiffness (R^2 = 0.73) but much better than BMD (R^2 = 0.55), 2D FEXI (R^2 = 0.32) and 2.5D FEXI (R^2 = 0.41).

It was argued that the difference in correlation of 3D FEXI-derived stiffness with mechanical test stiffness compared with CT FE-derived stiffness may be explained by the voxel dimensions employed in the two techniques. CT FE assumed each voxel as a cube of size 3mm, whereas 3D FEXI used voxel dimensions derived from the CT

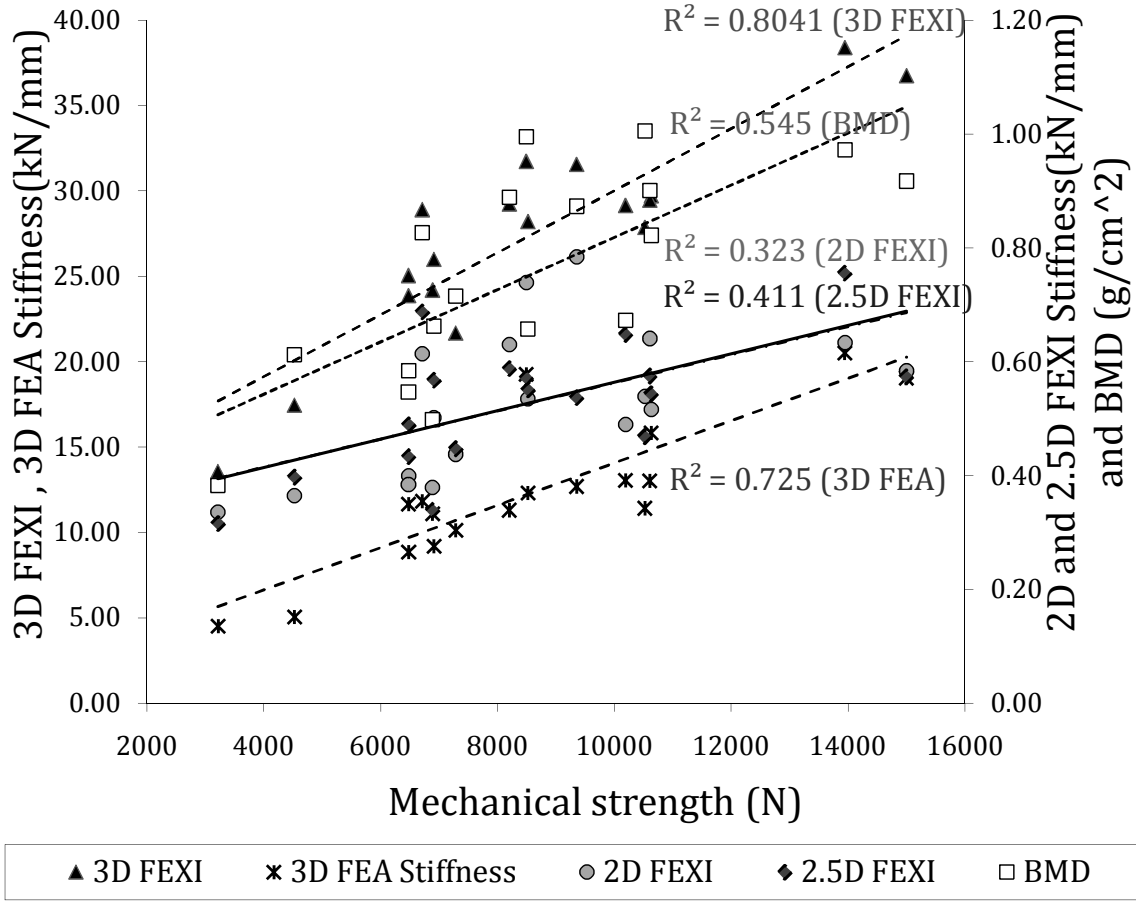

Figure 7.5: Correlation of Stance mechanical strength with stiffness for 3D FEXI, 2D FEXI, 2.5D FEXI, 3D FEA from CT and BMD

scan pixel sizes and slice thickness. Another reason suggested was the difference in shaft lengths considered. The FEXI approach used shaft lengths cut off at the lesser trochanter while the 3D FEA study used shafts of variable length. The correlation between the variation in shaft lengths and stiffness will be looked into as part of future work.

The high correlation of 3D-FEXI stiffness with mechanical stiffness suggested that it might be feasible to better predict bone strength from DXA scans with the

introduction of a shape atlas and applying finite element analysis to a reconstructed 3D bone model.

BMD assessment by DXA is routinely performed on the assumption that it is a reliable surrogate for the mechanical integrity of the bone being measured. Several experimental validation studies have reported on this, with various R^2 values reported including 79% for femoral neck BMC, n=61 (Dalen et al., 1976), 42% for femoral neck BMD, n=58 (Lochmuller et al., 1998), 89% for total hip BMD against pelvic fracture load, n=9 (Beason et al., 2003), 76% and 72% for total femoral BMC and BMD respectively, n = 54 (Eckstein et al., 2004). An enhancement of DXA-derived BMD is Hip Strength Analysis based upon a combination of cross-sectional area and cross-sectional moment of inertia, yielding an improvement in prediction of proximal femur strength from 62% for femoral neck BMD to 79% for HSA in an experimental study of 20 femora (Beck et al., 1990).

A number of studies over a significant number of years have also reported the utility of 3D FEA based upon CT image data to predict the mechanical integrity of the human proximal femur (Keyak et al., 1990, 1998; Keyak and Falkinstein, 2003; Lotz et al., 1991; Cody et al., 2000; Wirtz et al., 2003). With relevance to the current study, it has been demonstrated that in a stance loading configuration, a 3D finite element method derived from CT scan data explained at least 20% more of the variance in strength of the proximal femur than based upon either areal and volumetric density, with R^2 values of 83.7%, 57.4% and 66.1% (Cody et al., 1999).

Several approaches have been previously adopted to derive volumetric density (gcm^{-3}) from a conventional 2D DXA representation of areal bone mineral density (gcm^{-2}), necessitating the derivation of the unknown bone depth (cm). Such

approaches have generally aimed at deriving an average depth across the areal projection rather than creating a formal 3D shape of the bone. More consideration has been given to the lumbar vertebrae than the proximal femur. Few studies have quantified the accuracy of their approach. For example, the lumbar vertebra has been considered to be of cuboid nature, where the depth is calculated simply as the square root of the cross-sectional area (Carter et al., 1992; Jergas et al., 1995) or the mean vertebral width in the orthogonal direction (Duboeuf et al., 1994). Both scientific (Sabin et al., 1995) and clinical (Peel and Eastel, 1994) evaluation of the vertebra considered to be an elliptical cylinder have been performed, although both studies did not report a significant benefit in their volumetric approach. For assessment of the distal radius and ulna, an assumption of cylindrical geometry has been assumed (Boyanov et al., 2002). For the proximal femur, the square root of projected area has also been clinically applied to the femoral neck (Leslie et al., 2001; Hou et al., 2007).

This case study demonstrated that 3D FEXI derived from a single 2D radiographic image such as a DXA scan image with added bone shape information may be used to derive an accurate estimation of the stiffness of the proximal femur and to provide a better prediction of fracture-risk for patients.

Chapter 8

Conclusions

8.1 Summary

Osteoporosis has often been described as the 'silent epidemic' that typically affects the elderly, particularly women, causing debilitating hip and spine fractures. With the current changing demographics showing an increasingly ageing population, osteoporosis-related incapacitations are proving to be a major drain on national health resources. Osteoporosis measurement needs to consider bone quality along with bone quantity for an accurate assessment of fracture-risk for a patient. DXA scans, the current gold-standard for osteoporosis assessment, focus entirely on bone mineral density values. Bone quality measurements should include analysis of bone distribution as well as the shape of the bone.

The finite element analysis approach for testing bone strength has been previously studied and found to be better than BMD at estimating the mechanical strength of bones. However all of these studies had relied on the use of CT scans to create the

three-dimensional model for finite element analysis. The increased radiation dose as well as expense of CT scans make these approaches less likely to be introduced into routine osteoporosis assessment. An easy-to-use routine for assessing bone strength which could be used along with the current norm of DXA scanning was a major motivation behind this research.

Finite Element Analysis of X-ray Images (FEXI) used two-dimensional DXA scan images to build 2D finite element thin plane stress models. This technique considered bone density as well as bone distribution by assigning finite element material properties corresponding to the apparent bone mineral density at each pixel in the DXA image. The major drawback of this approach was the assumption of the bone as an object with constant thickness as also its inability to incorporate the effects of the head anteversion angle in the loading scenario. The shape analysis and reconstruction task was undertaken to add the bone geometry effects into the bone strength assessment computations.

As discussed in Chapter 3, the variation in the sensitivity of FEXI to changes in bone geometry corresponds to the observed variation in bone geometry. This effect is entirely missed by the BMD analysis. Also, the porcine femur study discussed in the afore-mentioned chapter showed that FEXI-derived stiffness correlates well with bone mineral density values. Thus, FEXI using the reconstructed 3D shape was found to incorporate the contributions of both bone mineral density as well bone geometry in the estimation of bone stiffness. Since the finite element material properties were based on the greyscale distribution of the DXA image, it was expected that this provided a good estimation of bone density distribution as well. Hence it was concluded that FEXI using a predicted 3D shape may provide a better assessment of osteoporosis than the conventional BMD analysis approach. The

availability of a shape atlas makes 3D finite element analysis of the bone for strength analysis a feasible and practical option to be evaluated for possible clinical use.

This research has demonstrated the potential for replication of 3D shape from a single 2D projection with applications including 3D finite element analysis for prediction of mechanical integrity of the proximal femur. A similar technique may be applied to generate shape atlases for other objects that can be similarly modelled.

8.2 Limitations & Future Work

The 3D FEXI technique relies on the input DXA image for areal bone density information from which it estimates volumetric bone density based on bone depth at each pixel. Since DXA does not discriminate between cortical and cancellous sections of the bone, this can affect the accuracy of bone strength assessment and hence fracture-risk prediction. Quantitative CT would be required to estimate volumetric density while distinguishing between cortical and trabecular bone. However, its high radiation dose and cost make it unsuitable for routine assessment. A future enhancement to the FEXI technique might look at modelling cortical and cancellous sections for the bone model with a mesh-like structure describing the trabeculae.

Several studies have looked at variation of bone shape between ethnic and gender groups as well as with age. Ward et al. (2007) found that there were differences in bone geometry, BMC and volumetric BMD at the radial diaphysis between South Asian and European women of UK origin which were not explained by differences in body size. They also concluded however, that there was no significant change in polar stress-strain index and hence the difference in bone geometry did not affect

bone strength. Ethnic differences were also found to contribute to bone mass and fracture risk in a study of 197,848 community-dwelling post menopausal women by Barrett-Connor et al. (2005). African-American and Asian women were found to have 50% and 70% lower fracture risk respectively compared to Caucasian, Hispanic and Native American women. They also found markedly higher fracture rates among African-American, Caucasian, and Hispanic women over 80 years of age than women of similar origin in younger age groups; but this effect of age on fracture risk was found to be less obvious among Asian and Native American women.

Meta et al. (2006) showed age-related changes in bone geometry among healthy women in two distinct age groups. Bone mineral content and bone mineral density values were seen to differ significantly between the 28 young and 124 elderly healthy Caucasian women included in the study. Cross-sectional area and volumes at skeletal sites such as the trochanter and femoral neck were also measured using QCT and found to be larger in the elderly than younger subjects although compressive and bending strength were higher among the young. Mayhew et al. (2005) found substantial thinning of the cortical shell at the femoral neck area with ageing. It was found that cortical thickness reduced by 6.4% in women along with a decline in critical stress of 13.2% each decade relative to a mean age of 60. Both cortical thinning and critical stress decline were found to be lesser among men than women. This study considered the distribution of bone from CT scans of the mid-femoral neck of 77 proximal femurs people who died suddenly aged 20 - 95 years.

A collection of ethnicity, gender and age-specific bone shape templates could be used to generate a comprehensive shape atlas. Bone shape reconstruction from a radiographic image could then be derived from the matched shape model, thus producing a more accurate predicted-3D bone for finite element analysis.

The shape reconstruction case study considered was based on a relatively small dataset of 23 femurs for the training set and 20 femurs for the validation set. Moreover, both the training and validation datasets came from people of similar ethnic backgrounds. A wider sampling of femurs, including extreme cases such as small stumpy bones and long slender bones, are required for a more rigorous testing of the shape template technique. The author would also like this technique tested for other bones such as the distal radius and the lumbar region of the vertebra which are the other main regions affected by osteoporosis.

FEXI application in a clinical setting would depend on the quality of the DXA scans in terms of exposure, contrast and orientation. The shape template procedure expects the alignment of the bone processes in the input 2D image to be close to the stored template 2D shape. The shape template application case study was based on a set of just 18 cadaveric femurs. This technique needs to be tested using clinical data including patients with confirmed osteoporosis and age-, sex-, and ethnicity-matched controls. Both DXA and CT scans may be carried out on these subjects and FE analysis performed on reconstructed models from both sets of scans, the former using the shape template. Paired t-test may then be used to compare the abilities of BMD, FEXI and CT-FE in terms of discriminating between the fracture and control groups. However, a clinical validation procedure such as this is quite time-consuming in terms of recruiting patients and requires ethics and research committee approvals. The additional radiation exposure for non-essential CT scans is expected to prove to be a major hurdle in this case.

The author envisions a software module built on this research to be used in conjunction with routine DXA scans in a clinical setting. The DXA scans would provide the bone quantity measurements with the FEXI analysis adding the bone

quality component. Such a system would improve the accuracy of bone stiffness and hence osteoporosis-related fragility fracture risk prediction.

Appendices

Appendix A: Additional FEXI Modules

A.1 Femur contour extraction from hip radiograph

One of the preliminary tasks in the FEXI process is to extract the femur contour from a radiograph of the pelvic area. The extraction of the femur contour required a solution that would accept a hip radiograph as input and deliver the femoral contour as output. A particular problem in this task was the extraction of the femoral head since this was not always clearly outlined in the X-ray images.

Several methods were considered starting from simple gradient-based edge detection to seeded region growing (Adams and Bischof, 1994) and snake-based segmentation algorithms (Kass et al., 1987). These were discarded due either to the poor quality of the results obtained or to too much manual intervention being required.

A template-based approach was finally chosen for this task. An interface was designed to allow the user to define the control points to fit the template contour to the femoral outline in the radiographic image. The template femur outline was

then warped to fit these control points using the polynomial-fit routine provided by MATLAB. The warped template was then used as a mask to filter out the femur from the hip X-ray. This module has been used in various 2D FEXI studies involving

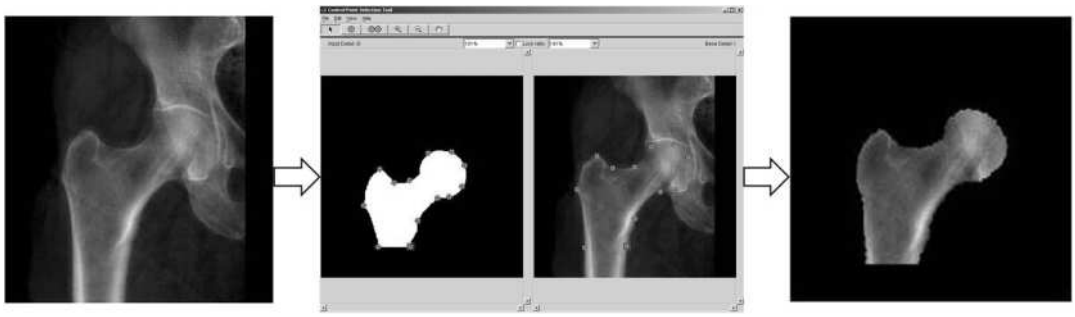

Figure A.1: The contour extraction process

in-vivo samples. The case studies described in this thesis were based on cadaveric femurs and hence the contour extraction module was not required. It is, however, an important component of the FEXI cycle for clinical application.

A.2 Improved BMD assessment

An improved greyscale-BMD regression technique was devised for use with input DXA images. For this, average grey values were computed for the shaft, trochanter and neck regions along with the average of all these three regions. The regions were demarcated similar to the region-boundaries defined by standard DXA software. These regional grey values were then mapped to the corresponding BMD values obtained from the DXA scanning software and the regression equation was determined. This regression was then used to compute the apparent areal BMD from the grey levels in the radiographic image. This BMD mapping approach was

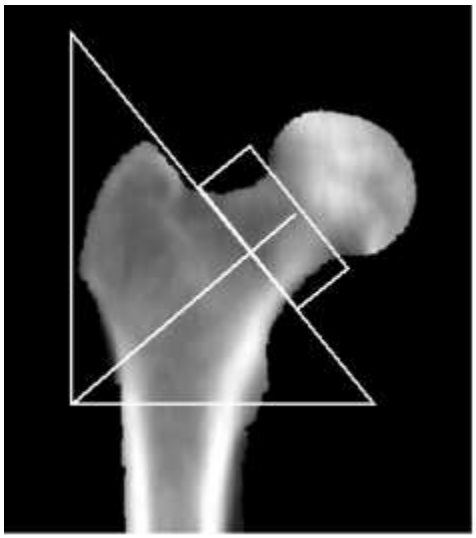

Figure A.2: BMD regions

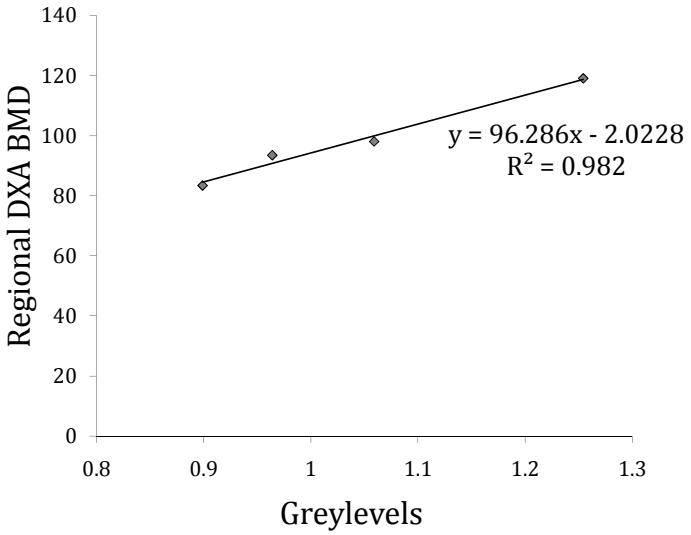

Figure A.3: BMD regression

not utilised for the study described in this document as the input 2D test images used were 2D projections from the CT data and not actual DXA scans.

A.3 Fall loading scenario

The fall loading condition was designed to simulate the scenario of a person falling sideways on their hip. The loading configuration adopted was as defined by Keyak et al. (2005) with the femoral shaft orientated at an angle of 30^o to the ground, pivoted at the junction of the inter-trochanteric line and the shaft axis. A neck anteversion angle of 30^o was also applied as might be seen in an actual fall situation. For the finite element analysis, a platen was attached to the greater trochanter and the bone was loaded at the femoral head, as shown in figure A.4. This loading

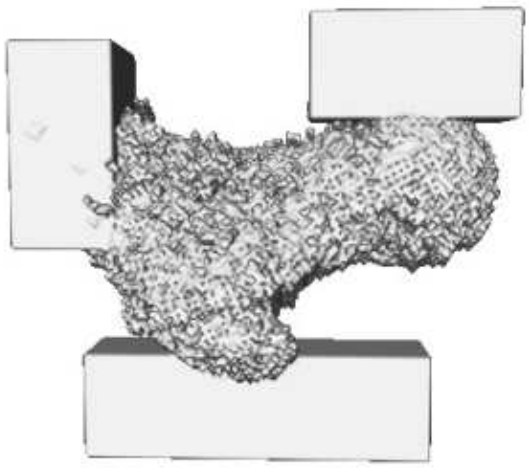

Figure A.4: The 'Fall' loading condition

scenario was omitted from the results discussed in 7 because of unavailability of CT FE and mechanical stiffness results for this loading scenario. However, this loading setup will be used for testing the performance of 3D FEXI in ongoing and future bone strength studies.

Appendix B: Glossary

Table B.1: Glossary of commonly-used terms used in this document

Term	**Description**
Cortex	The thick outer shell of a bone
Cancellous bone	Bone in which the trabeculae form a latticework, with interstices filled with bone marrow
Marrow	The fatty network of connective tissue that fills the cavities of bones
Femur	The longest and thickest bone of the human skeleton; extends from the pelvis to the knee
Proximal femur	the proximal end of the femur - from the lesser trochanter up to the pelvis
Femoral Shaft	The cylindrical mid-section of a long bone (the femur, in this case)
Trochanter	One of the bony prominences developed near the upper extremity of the femur to which muscles are attached
Femoral Neck	The short constricted portion of the femur between the trochanter and the head
Femoral Head	The hemispheric surface at the upper extremity of the femur
Neck-shaft angle	The angle between a line drawn through the shaft of the femur with one passing through the long axis of the femoral neck
Head/ Neck anteversion	The angular displacement of the femoral head such that its axis is directed forward
FEXI	Finite Element Analysis of X-ray Images
FEA	Finite Element Analysis

Continued on next page...

Table B.1 – Continued

Term	**Description**
Stiffness	It is the resistance of an elastic body to deformation by an applied force (unit: N/m)
Strength	The stress at which a material starts deforming plastically (unit: Pa)
Young's modulus	Also known as the modulus of elasticity - is a measure of the stiffness of a given material (unit: Pa)
Poisson's ratio	The ratio of relative contraction strain to relative extension strain for a given material. It describes the tendency of a material to deform along one or more axes corresponding to a deformation in another axis.
BMD	Bone Mineral Density - a measure of the amount of minerals (such as calcium) in the bone
aBMD	Apparent BMD - calculated as the areal BMD based up on the average grey level of the bone pixels within a radiographic image
Bone tissue density	Reflects the mineralized bone tissue (material) density, determined from Archimedes' principle, and calculated as dry weight of the specimen divided by the volume of bone matrix excluding marrow space (unit: gcm^{-3})
Apparent density	Reflects the mineralized bone apparent (structural) density, and calculated as dry weight of the specimen divided by the volume of specimen (unit: gcm^{-3})
Ash density	Reflects the mineralized bone non-organic density, and calculated as ash weight of the specimen divided by the volume of specimen (unit: gcm^{-3})
DXA	Dual-Energy X-ray Absorptiometry - measures BMD in regions of the bone
X-ray, Radiograph	An image produced on a radiosensitive surface such as a photographic film by radiation (x-rays) passing through the object being scanned
Radiographic image	An image created as a substitute for an actual radiograph by taking a 2D axial projection of a given 3D object
CT	Computed Tomography (previously, Computed Axial Tomography, CAT) scans generate 3D models of an object using multiple cross-sectional slices along an axis

Continued on next page...

Table B.1 – Continued

Term	**Description**
MRI	Magnetic Resonance Imaging uses radio frequency signals applied to an object in a magnetic field to create a slice-by-slice view of an object
Landmark	Homologous points on a shape that are in the same plane and can be found repeatedly and reliably
Landmark configuration	The set of landmark co-ordinates for a particular specimen
GPA	Generalised Procrustes Analysis is used to align a set of shapes by removing Euclidean transformations between them
TPS	Thin Plate Spline is an interpolation function used to describe the deformation from one landmark configuration to another
Offset	The number of voxels from the edge of the slice to the first bone voxel in that column
Depth	The number of voxels from the edge of the slice to the last bone voxel along the particular column

References

H. Abdi. *Encyclopedia for research methods for the social sciences.*, chapter PLS-Regression; Multivariate analysis. Thousand Oaks:Sage, 2003.

R. Adams and L. Bischof. Seeded region growing. *IEEE Transactions on PAMI*, 16 (6):641 647, June 1994.

K. Akesson, S. Ljunghall, B. Jonsson, I. Sernbo, l. O. Johnel, l. P. Grdsel, and K. Obrant. Assessment of biochemical markers of bone metabolism in relation to the occurrence of fracture: a retrospective and prospective population-based study of women. *Journal of Bone & Mineral Research*, 10(11):1823–9, November 1995.

C. G. Alonso, M. D. Curiel, F. H. Carranza, R. P. Cano, and A. D. Pacrez. Femoral bone mineral density, neck-shaft angle and mean femoral neck width as predictors of hip fracture in men and women. *Osteoporosis International*, 11(8):714, 2000.

L. Apostol, V. Boudousq, O. Basset, C. Odet, S. Yot, J. Tabary, J. Dinten, E. Boiler, P. Kotzki, and F. Peyrin. Relevance of 2D radiographic texture analysis for the assessment of 3D bone micro-architecture. *Medical physics*, 33(9):3546–56, Sep 2006.

M. Armand, T. J. Beck, M. Boyle, M. Z. Oden, L. Voo, and J. R. Shapiro. A semi-automatic technique for generating parametric FE model of femur from imaging

modalities. In *2003 Summer Bioengineering Conference, June 25-29*, Sonesta Beach Resort in Key Biscayne, Florida, 2003.

E. Barrett-Connor, E. S. Siris, L. E. Wehren, P. D. Miller, T. A. Abbott, M. L. Berger, A. C. Santora, and L. M. Sherwood. Osteoporosis and fracture risk in women of different ethnic groups. *Journal of Bone and Mineral Research*, 20(2): 185–194, 2005.

M. Bastir, A. Rosas, and H. D. Sheets. *The morphological integration of the hominoid skull: a partial least squares and PC analysis with morphogenetic implications for European Mid-Pleistocene mandibles*. New York: Kluwer Academic/Plenum Publishers, 2005.

D. C. Bauer, B. Ettinger, M. C. Nevitt, and K. L. Stone. Risk for fracture in women with low serum levels of thyroid-stimulating hormone. *Annals of Internal Medicine*, 134(7):561–568, April 2001.

D. P. Beason, G. J. Dakin, R. R. Lopez, J. E. Alonso, F. A. Bandak, and A. W. Eberhardt. Bone mineral density correlates with fracture load in experimental side impacts of the pelvis. *Journal of Biomechanics*, 36(2):219–227, Feb. 2003.

T. Beck, F. Mourtada, C. Ruff, W. J. Scott, and G. Kao. Experimental testing of a DEXA-derived curved beam model of the proximal femur. *Journal of orthopaedic research*, 16(3):394–8, May 1998.

T. Beck, C. Ruff, and K. Bissessur. Age-related changes in female femoral neck geometry: implications for bone strength. *Calcified Tissue International*, 53(Suppl 1):S41–6, 1993.

T. Beck, C. Ruff, W. J. Scott, C. Plato, J. Tobin, and C. Quan. Sex differences in

geometry of the femoral neck with aging: a structural analysis of bone mineral data. *Calcified Tissue International*, 50(1):24–9, Jan 1992.

T. Beck, C. Ruff, K. Warden, W. J. Scott, and G. Kao. Predicting femoral neck strength from bone mineral data. A structural approach. *Investigative Radiology*, 25(1):6–18, Jan 1990.

C. Bergot, V. Bousson, A. Meunier, M. Laval-Jeantet, and J. D. Laredo. Hip fracture risk and proximal femur geometry from DXA scans. *Osteoporosis International*, 13(7):542, 2002.

C. A. Bernaards and R. I. Jennrich. Gradient Projection Algorithms and software for arbitrary rotation criteria in factor analysis. *Educational and Psychological Measurement*, 65(5):676–696, 2005.

M. Bessho, I. Ohnishi, J. Matsuyama, T. Matsumoto, K. Imai, and K. Nakamura. Prediction of strength and strain of the proximal femur by a CT-based finite element method. *Journal of Biomechanics*, 40:17451753, 2007.

V. Blanz, A. Mehl, T. Vetter, and H.-P. Seidel. A statistical method for robust 3D surface reconstruction from sparse data. In *3DPVT '04: Proceedings of the 3D Data Processing, Visualization, and Transmission, 2nd International Symposium on (3DPVT'04)*, pages 293–300, Washington, DC, USA, 2004. IEEE Computer Society. ISBN 0-7695-2223-8.

F. L. Bookstein. The Truss: Body form reconstruction in morphometrics. *Systematic Zoology*, 31(2):113–135, 1982.

F. L. Bookstein. Principal warps-thin-plate splines and the decomposition of deformations. *IEEE Transactions on Pattern Analysis and Machine Intelligence*, 11(6):567–585, 1989.

F. L. Bookstein. *Morphometric tools for landmark data: geometry and biology*. Cambridge University Press, Cambridge, 1991.

F. L. Bookstein, B. Chernoff, R. L. Elder, J. M. J. Humphries, G. R. Smith, and R. E. Strauss. *Morphometrics in evolutionary biology*. Number 15. Academy of Natural Sciences Press, Philadelphia, 1985.

M. Bouxsein, A. Courtney, and W. Hayes. Ultrasound and densitometry of the calcaneus correlate with the failure loads of cadaveric femurs. *Calcified Tissue International*, 56(2):99–103, February 1995.

M. L. Bouxsein, B. S. Coan, and S. C. Lee. Prediction of the strength of the elderly proximal femur by bone mineral density and quantitative ultrasound measurements of the heel and tibia. *Bone*, 25(1):49–54, July 1999.

M. L. Bouxsein, P. Szulc, F. Munoz, E. Thrall, E. Sornay-Rendu, and P. D. Delmas. Contribution of trochanteric soft tissues to fall force estimates, the factor of risk, and prediction of hip fracture risk. *Journal of Bone and Mineral Research*, 22(6): 825–831, 2007.

M. Boyanov, P. Popivanov, and G. Gentchev. Assessment of forearm volumetric bone mineral density from standard areal densitometry data. *Journal of Clinical Densitometry*, 5(4):391–402, Dec. 2002. ISSN 1094-6950.

W. A. M. Brekelmans, W. Poort, and T. J. J. H. Slooff. A new method to analyse the mechanical behaviour of skeletal parts. *Acta Orthopaedica Scandinavica*, 43: 301–317, 1972.

H. T. Calis, M. Eryavuz, and M. Calis. Comparison of femoral geometry among cases with and without hip fractures. *Yonsei Medical Journal*, 45(5):901–907, 2004.

L. Caponetti and A. M. Fanelli. 3D bone reconstruction from two X-ray views. In *IEEE Conf. Eng. in Medicine and Biology*, pages 208–210, 1990.

D. Carter, M. Bouxsein, and R. Marcus. New approaches for interpreting projected bone densitometry data. *Journal of Bone and Mineral Research*, 7(2):137–45, 1992.

X. G. Cheng, P. H. F. Nicholson, S. Boonen, P. Brys, G. Lowet, J. Nijs, and J. Dequeker. Effects of anteversion on femoral bone mineral density and geometry measured by dual energy X-ray absorptiometry: A cadaver study. *Bone*, 21(1): 113, 1997.

C. H. Chesnut, N. H. Bell, G. S. Clark, B. L. Drinkwater, S. C. English, C. C. Johnston, M. Notelovitz, C. Rosen, D. F. Cain, K. A. Flessland, and N. J. S. Mallinak. Hormone Replacement Therapy in postmenopausal women: Urinary N-telopeptide of type I collagen monitors therapeutic effect and predicts response of Bone Mineral Density. *The American Journal of Medicine*, 102(1):29–37, Jan. 1997.

J. Choi, J. W. Harvey, and M. H. Conklin. Use of multi-parameter sensitivity analysis to determine relative importance of factors influencing natural attenuation of mining contaminants. In *U.S. Geological Survey Toxic Substances Hydrology Program-Technical Meeting*, volume 1(C), pages 185–192, Charleston, South Carolina, March 8-12 1999.

D. D. Cody, G. J. Gross, F. J. Hou, H. J. Spencer, S. A. Goldstein, and D. P. Fyhrie. Femoral strength is better predicted by finite element models than QCT and DXA. *Journal of Biomechanics*, Oct.32(10):1013–20, 1999.

D. D. Cody, F. J. Hou, and G. Divine. Femoral structure and stiffness in patients with femoral neck fracture. *Journal of Orthopaedic Research*, 18(3):443–448, 2000.

Consensus Development Conference. Prophylaxis and treatment of osteoporosis. *Osteoporosis International*, 1(2):114–7, 1991.

T. F. Cootes and C. J. Taylor. Statistical models of appearance for computer vision. Technical report, Imaging Science and Biomedical Engineering, University of Manchester, 2004.

S. C. Cowin, editor. *Bone Mechanics Handbook*. CRC Press LLC, 2nd edition, 2001.

N. J. Crabtree, H. Kroger, A. Martin, H. A. P. Pols, R. Lorenc, J. Nijs, J. J. Stepan, J. A. Falch, T. Miazgowski, S. Grazio, P. Raptou, J. Adams, A. Collings, K. T. Khaw, N. Rushton, M. Lunt, A. K. Dixon, and J. Reeve. Improving risk assessment: Hip geometry, bone mineral distribution and bone strength in hip fracture cases and controls. The EPOS Study. *Osteoporosis International*, 13(1): 48, 2002.

S. Cummings, D. Black, M. Nevitt, W. Browner, J. Cauley, K. Ensrud, H. Genant, L. Palermo, J. Scott, and T. Vogt. Bone density at various sites for prediction of hip fractures. The Study of Osteoporotic Fractures Research Group. *Lancet*, 341 (8837):72–75, Jan 1993.

S. R. Cummings, D. Bates, and D. M. Black. Clinical use of bone densitometry. *Scientific Review and Clinical Applications*, 288(15):1889–97, 2002.

E. E. Cureton and R. B. D'Agostino. *Factor analysis: an applied approach*. Lawrence Erlbaum Associates, Hillsdale, NJ, 1983.

J. D. Currey. *Bones: structure and mechanics*. Princeton University Press, 2002.

N. Dalen, L. G. Hellstrom, and B. Jacobson. Bone mineral content and mechanical strength of the femoral neck. *Acta Orthopaedica Scandinavica*, 47:503–508, 1976.

J. Damilakis, G. Papadokostakis, K. Perisinakis, T. Maris, P. Dimitriou, A. Hadjipavlou, and N. Gourtsoyiannis. Discrimination of hip fractures by quantitative ultrasound of the phalanges and the calcaneus and dual X-ray absorptiometry. *European Journal of Radiology*, 50(3):268–72, June 2004.

S. Delorme, Y. Petit, C.-E. Aubin, J. Dansereau, H. Labelle, C. Landry, and J. de Guise. Three-dimensional modelling and rendering of the human skeletal trunk from 2D radiographic images. *3dim*, 00:0497, 1999.

J. W. T. Dickerson. The effect of development on the composition of a long bone of the pig, rat and fowl. *The Biochemical Journal*, 82:47–55, 1962.

M. Ding. Age variations in the properties of human tibial trabecular bone and cartilage. *Acta Orthopaedica Scandinavica*, 71((Suppl 292)):1–45, June 2000.

I. L. Dryden and K. V. Mardia. *Statistical shape analysis*. John Wiley & Sons, New York, 1998.

F. Duboeuf, R. Pommet, P. Meunier, and P. Delmas. Dual-energy X-ray absorptiometry of the spine in anteroposterior and lateral projections. *Osteoporos International*, 4(2):110–6, 1994.

F. Eckstein, C. Wunderer, H. Boehm, V. Kuhn, M. Priemel, T. M. Link, and E.-M. Lochmuller. Reproducibility and side differences of mechanical tests for determining the structural strength of the proximal femur. *Journal of Bone and Mineral Research*, 19(3):379–385, 2004.

S. El-Kaissi, J. A. Pasco, M. J. Henry, S. Panahi, J. G. Nicholson, G. C. Nicholson, and M. A. Kotowicz. Femoral neck geometry and hip fracture risk: the Geelong osteoporosis study. *Osteoporos International*, 16:12991303, 2005.

Encyclopdia Britannica. Procrustes. Encyclopdia Britannica Online, 2007. URL `http://www.britannica.com/eb/article-9061475`.

K. G. Faulkner. Hip axis length and osteoporotic fractures. *Journal of Bone & Mineral Research*, 10(3):506–508, 1995.

K. G. Faulkner, S. R. Cummings, D. Black, L. Palermo, C. Gluer, and G. H K. Simple measurement of femoral geometry predicts hip fracture: the study of osteoporotic fractures. *Journal of Bone & Mineral Research*, 8(10):1211–7, Oct 1993.

I. Fogelman, J. Adams, J. McCrea, S. A. Steel, and G. M. Blake. Position statement on the reporting of dual energy x-ray absorptiometry (DXA) bone mineral density scans. Technical report, National Osteoporosis Society, August 2002.

J. D. Foley, A. V. Dam, S. K. Feiner, and J. F. Hughes. *Computer Graphics: Principles and Practice*. Addison-Wesley, 2nd edition, 1990.

P. Garnero, E. Hausherr, M. Chapuy, C. Marcelli, H. Grandjean, C. Muller, C. Cormier, G. Brart, P. Meunier, and P. Delmas. Markers of bone resorption predict hip fracture in elderly women: the EPIDOS Prospective Study. *Journal of Bone & Mineral Research*, 11(10):1531–8, October 1996.

P. Garnero, E. Sornay-Rendu, B. Claustrat, and P. Delmas. Biochemical markers of bone turnover, endogenous hormones and the risk of fractures in postmenopausal women: the OFELY study. *Journal of Bone & Mineral Research*, 15(8):1526–36, August 2000.

H. K. Genant, K. Engelke, T. Fuerst, C.-C. Gluer, S. Grampp, S. T. Harris, M. Jergas, T. Land, Y. Lu, S. Majumdar, A. Mathur, and M. Takada. Noninvasive

assessment of bone mineral and structure: State of the art. *Journal of Bone & Mineral Research*, 11:707–730, 1996.

C. C. Gluer, S. R. Cummings, A. Pressman, J. Li, K. Gluer, K. G. Faulkner, S. Grampp, and H. K. Genant. Prediction of hip fractures from pelvic radiographs: the study of osteoporotic fractures. The Study of Osteoporotic Fractures Research Group. *Journal of Bone & Mineral Research*, 9(5):671–7, May 1994.

S. Gnudi, C. Ripamonti, G. Gualtieri, and N. Malavolta. Geometry of proximal femur in the prediction of hip fracture in osteoporotic women. *British Journal of Radiology*, 72(860):729–733, August 1, 1999 1999.

P. Golland. *Statistical shape analysis of anatomical structures*. PhD thesis, Massachusetts Institute of Technology, 2001.

J. K. Gong, J. S. Arnold, and S. H. Cohn. Composition of trabecular and cortical bone. *The Anatomical Record*, 149(3):325–331, 1964.

H. Gray. *Anatomy of the Human Body*. Lea & Febiger, Philadelphia, 20 edition, 2000.

J. S. Gregory, D. Testi, A. Stewart, P. E. Undrill, D. M. Reid, and R. M. Aspden. A method for assessment of the shape of the proximal femur and its relationship to osteoporotic hip fracture. *Osteoporosis International*, 15(1):5, 2004.

Y. He, B. Fan, D. Hans, J. Li, C. Wu, C. Njeh, S. Zhao, Y. Lu, E. Tsuda-Futami, T. Fuerst, and H. Genant. Assessment of a new quantitative ultrasound calcaneus measurement: precision and discrimination of hip fractures in elderly women compared with dual X-ray absorptiometry. *Osteoporos Int.*, 11(4):354–60, 2000.

K. H. Hohne, M. Bomans, A. Pommert, M. Riemer, C. Schiers, U. Tiede, and

G. Wiebecke. 3D-visualization of tomographic volume data using the generalized voxel-model. In *CH Volume Visualization Workshop*, 1989.

C. J. Hosiet, D. A. Smith, A. D. Deacon, and C. M. Langton. Comparison of broadband ultrasonic attenuation of the os calcis and quantitative computed tomography of the distal radius. *Clinical Physics and Physiological Measurement*, 8(4):303–308, 1987.

Y.-L. Hou, X.-P. Wu, X.-H. Luo, H. Zhang, X.-Z. Cao, Y.-B. Jiang, and E.-Y. Liao. Differences in age-related bone mass of proximal femur between Chinese women and different ethnic women in the United States. *Journal of Bone and Mineral Metabolism*, 25(4):243–252, July 2007.

S. L. Hui, C. W. Slemenda, and J. C. Conrad Johnston. Age and bone mass as predictors of fracture in a prospective study. *Journal of Clinical Investigation*, 81: 1804–1809, 1988.

International Osteoporosis Foundation. New study shows that osteoporosis accounts for significant burden of disease worldwide. *Osteoporosis Action*, 10(3):2, 2006.

S. Jackson. *Cross-Sectional Imaging Made Easy*. Churchill Livingstone, 2004.

M. Jergas, M. Breitenseher, C. Gler, W. Yu, and H. Genant. Estimates of volumetric bone density from projectional measurements improve the discriminatory capability of dual X-ray absorptiometry. *Journal of Bone & Mineral Research*, 10 (7):1101–10, 1995.

S. Kadoury, F. Cheriet, C. Laporte, and H. Labelle. A versatile 3D reconstruction system of the spine and pelvis for clinical assessment of spinal deformities. *Medical & Biological Engineering & Computing*, 45(6):p591 – 602, 2007.

H. Kaiser. The varimax criterion for analytic rotation in factor analysis. *Psychometrika*, 23(3):187–200, Sept. 1958.

T. S. Kaneko, J. S. Bell, M. R. Pejcic, J. Tehranzadeh, and J. H. Keyak. Mechanical properties, density and quantitative CT scan data of trabecular bone with and without metastases. *Journal of Biomechanics*, 37:523–530, 2004.

T. S. Kaneko, M. R. Pejcic, J. Tehranzadeh, and J. H. Keyak. Relationships between material properties and CT scan data of cortical bone with and without metastatic lesions. *Medical Engineering & Physics*, 25:445–454, 2003.

K. M. Karlsson, I. Sernbo, K. J. Obrant, I. Redlund-Johnell, and O. Johnell. Femoral neck geometry and radiographic signs of osteoporosis as predictors of hip fracture. *Bone*, 18(4):327, 1996.

M. Kass, A. Witkin, and D. Terzopoulos. Snakes: Active contour models. *International Journal of Computer Vision*, 1(4):321331, 1987.

M. J. Keenan, M. Hegsted, K. L. Jones, J. P. Delany, J. C. Kime, L. E. Melancon, R. T. Tulley, and K. D. Hong. Comparison of bone density measurement techniques: DXA and Archimedes principle. *Journal of Bone & Mineral Research*, 12(11):1903–7, Nov 1997.

D. Kendall. The diffusion of shape. *Advances in Applied Probability*, 9:428–430, 1977.

D. G. Kendall, D. Barden, T. K. Carne, and H. Le. *Shape and Shape Theory*. John Wiley & Sons, Ltd., Chichester, UK, 1999.

J. H. Keyak. Improved prediction of proximal femoral fracture load using nonlinear finite element models. *Medical Engineering & Physics*, Apr. 23(3):165–73, 2001.

J. H. Keyak and Y. Falkinstein. Comparison of in situ and in vitro CT scan-based finite element model predictions of proximal femoral fracture load. *Medical Engineering & Physics*, 25(9):781–787, Nov. 2003.

J. H. Keyak, T. S. Kaneko, J. Tehranzadeh, and H. B. Skinner. Predicting proximal femoral strength using structural engineering models. *Clinical Orthopaedics & Related Research*, 437:219–228, 2005.

J. H. Keyak, J. M. Meagher, H. B. Skinner, and C. D. J. Mote. Automated three-dimensional finite element modelling of bone: a new method. *Journal of Biomedical Engineering*, 12(5):389–97, 1990.

J. H. Keyak, S. A. Rossi, K. A. Jones, and H. B. Skinner. Prediction of femoral fracture load using automated finite element modeling. *Journal of Biomechanics*, 31:125–133, 1998.

M. Kleerekoper, A. R. Villanueva, J. Stanciu, D. S. Rao, and A. M. Parfitt. The role of three-dimensional trabecular microstructure in the pathogenesis of vertebral compression fractures. *Calcified Tissue International*, 37(6):594–597, November 1985.

S. Kolta, A. Le Bras, D. Mitton, V. Bousson, J. A. de Guise, J. Fechtenbaum, J. D. Laredo, C. Roux, and W. Skalli. Three-dimensional X-ray absorptiometry (3D-XA): a method for reconstruction of human bones using a dual X-ray absorptiometry device. *Osteoporosis International*, 16(8):969–976, 2004.

H. Lamecker, T. H. Wenckebach, and H.-C. Hege. Atlas-based 3D-shape reconstruction from X-ray images. In *ICPR '06: Proceedings of the 18th International Conference on Pattern Recognition*, pages 371–374, Washington, DC, USA, 2006.

P. Lang, P. Steiger, K. Faulkner, C. Gleuer, and H. K. Genant. Osteoporosis: Current techniques and recent developments in quantitative bone densitometry. *Radiologic clinics of North America*, 29:49–76, 1991.

C. M. Langton. *Measurement of broadband ultrasonic attenuation in cancellous bone*. PhD thesis, University of Hull, 1984.

C. M. Langton and C. F. Njeh, editors. *The Physical Measurement of Bone*. Institute of Physics Press; Bristol, UK, 2004.

C. M. Langton, C. F. Njeh, R. Hodgskinson, and C. J. D. Prediction of mechanical properties of the human calcaneus by broadband ultrasonic attenuation. *Bone*, 18:495–503, 1996.

C. M. Langton, J. A. Thorpe, and M. J. Fagan. Finite element analysis of DXA images (FEXI) for the prediction of osteoporotic fractures - Experimental validation. *Journal of Bone and Mineral Research*, 19(Suppl. 1):S365, 2004.

C. M. Langton, J. A. Thorpe, S. Pisharody, D. K. Langton, S. A. Steel, and S. Das. Discrimination of BMD-matched recent hip fracture subjects by FEXI (Finite Element Analysis of X-ray images). *Journal of Bone and Mineral Research*, 20 (7):1300, 2005.

S. Laporte, W. Skalli, D. G. J. A, F. Lavaste, and D. Mitton. A biplanar reconstruction method based on 2D and 3D contours - Application to the distal femur. *Computer Methods in Biomechanics and Biomedical Engineering*, 6(1):16, 2003.

C. M. Les, J. H. Keyak, S. M. Stover, K. T. Taylor, and A. J. Kaneps. Estimation of material properties in the equine metacarpus with use of quantitative computed tomography. *Journal of Orthopedic Research*, 12:822–833, 1994.

W. D. Leslie, G. DeVos, J. O. Dupont, and A. E. Peterdy. Reproducibility of volume-adjusted Bone Mineral Density of spine and hip from Dual X-ray Absorptiometry. *Journal of Clinical Densitometry*, 4(4):307–312, Dec. 2001.

E. Lochmuller, J. Zeller, D. Kaiser, F. Eckstein, J. Landgraf, R. Putz, and R. Steldinger. Correlation of femoral and lumbar DXA and calcaneal ultrasound, measured in situ with intact soft tissues, with the in vitro failure loads of the proximal femur. *Osteoporosis International*, 8(6):591–598, Nov. 1998.

A. Looker, D. Bauer, C. Chesnut, C. Gundberg, M. Hochberg, G. Klee, M. Kleerekoper, N. Watts, and B. NH. Clinical use of biochemical markers of bone remodeling: Current status and future directions. *Osteoporosis International*, 11 (6):467–80, 2000.

A. Looker, T. Beck, and E. Orwoll. Does body size account for gender differences in femur bone density and geometry? *Journal of Bone & Mineral Research*, 16 (7):1291–9, July 2001.

W. E. Lorensen and H. E. Cline. Marching cubes- A high resolution 3D surface construction algorithm. *Computer Graphics*, 21(4):163–169, 1987.

J. C. Lotz, E. J. Cheal, and W. C. Hayes. Fracture prediction for the proximal femur using finite element models. *Journal of Biomechanical Engineering*, 113(4): 353–60, 1991.

B. F. J. Manly. *Multivariate Statistical Methods.* Chapman & Hall / CRC, 2nd edition, 2000.

L. F. Marcus. Traditional morphometrics. In F. Rohlf and F. L. Bookstein, editors, *Proceedings of the Michigan morphometrics workshop*, number 2, pages 77–122, University of Michigan Museum of Zoology, Ann Arbor, 1990.

P. M. Mayhew, C. D. Thomas, J. G. Clement, N. Loveridge, T. J. Beck, W. Bonfield, C. J. Burgoyne, and J. Reeve. Relation between age, femoral neck cortical stability and hip fracture risk. *Lancet*, 366:12935, 2005.

M. Meta, Y. Lua, J. H. Keyak, and T. Lang. Young-elderly differences in bone density, geometry and strength indices depend on proximal femur sub-region: A cross sectional study in Caucasian-American women. *Bone*, 36:152–158, 2006.

J. Michelotti and J. Clark. Femoral neck length and hip fracture risk. *Journal of Bone & Mineral Research*, 14(10):1714–20, 1999.

D. Mitton, C. Landry, S. Veron, W. Skalli, F. Lavaste, and J. A. De Guise. 3D reconstruction method from biplanar radiography using non-stereocorresponding points and elastic deformable meshes. *Medical & Biological Engineering & Computing*, 38(2):133–9, 2000.

A. Mitulescu, W. Skalli, D. Mitton, and D. G. J. A. Three-dimensional surface rendering reconstruction of scoliotic vertebrae using a non stereo-corresponding points technique. *European Spine Journal*, 11:344352, 2002.

M. E. Muller, C. E. Webber, and M. L. Bouxsein. Predicting the failure load of the distal radius. *Osteoporosis International*, 14(4):345–352, June 2003.

T. Nakamura, C. Turner, T. Yoshikawa, C. Slemenda, M. Peacock, D. Burr, Y. Mizuno, H. Orimo, Y. Ouchi, and C. J. Johnston. Do variations in hip geometry explain differences in hip fracture risk between Japanese and white Americans? *Journal of Bone & Mineral Research*, 9(7):1071–6, July 1994.

National Institute of Health. Osteoporosis Prevention, Diagnosis and Therapy. NIH Consensus Statement, 2000.

National Institute of Health. National Institute of Health Osteoporosis and Related Bone Diseases. Osteoporosis Fact Sheet, 2003. URL `http://www.osteo.org/`.

National Osteoporosis Society. Osteoporosis facts and figures. Booklet, January 2006. URL `http://www.nos.org.uk`.

B. Nikkhade-Dehkordi, M. Bro-Nielsen, T. Darvann, C. Gramkow, N. Egund, and K. Hermann. 3D reconstruction of the femoral bone using two X-ray images from orthogonal views. In *Computer Assisted Radiology (CAR'96)*, page 1015, Paris, France, June 26-29 1996 1996.

C. Njeh, C. Boivin, and C. Langton. The role of ultrasound in the assessment of osteoporosis: a review. *Osteoporos International*, 7(1):7–22, 1997a.

C. Njeh, C. Kuo, C. Langton, H. Atrah, and C. Boivin. Prediction of human femoral bone strength using ultrasound velocity and BMD: an in vitro study. *Osteoporos International*, 7(5):471–7, 1997b.

C. F. Njeh, T. Fuerst, D. Hans, G. M. Blake, and H. K. Genant. Radiation exposure in bone mineral density assessment. *Applied Radiation and Isotopes*, 50:215–236, 1999.

J. Novosad, F. Cheriet, Y. Petit, and H. Labelle. Three-dimensional (3-D) reconstruction of the spine from a single X-ray image and prior vertebra models. *IEEE Trans Biomed Eng.*, 51(9):1628–39, Sep 2004.

T. Ohkubo. Bone measurement method and apparatus. United States Patent 6449502, September 2002.

Y. C. Pao. *A first course in Finite Element Analysis*. Allyn and Bacon Inc., 1986.

A. M. Parfitt. Bone age, mineral density, and fatigue damage. *Calcified Tissue International*, 53(Supplement - 1):S82–S86, February 1993.

J. Partanen, T. Jamsa, and P. Jalovaara. Influence of the upper femur and pelvic geometry on the risk and type of hip fractures. *Journal of Bone & Mineral Research*, 16(8):1540, August 2001.

M. Peacock, C. H. Turner, G. Liu, A. K. Manatunga, and C. C. J. Timmerman, L Jr. Better discrimination of hip fracture using bone density, geometry and architecture. *Osteoporosis International*, 5(3):167–73, May 1995.

K. Pearse and M. McCarthy. Generation of three dimensional finite element bone models from CT scan datasets. In *International Postgraduate Research Student Conference*, Dublin Institute of Technology, November 1998.

N. Peel and l. R. Eastel. Diagnostic value of estimated volumetric bone mineral density of the lumbar spine in osteoporosis. *Journal of Bone & Mineral Research*, 9(3):317–20, 1994.

K. A. Peter Ebeling. Role of biochemical markers in the management of osteoporosis. *Best Practice & Research Clinical Rheumatology*, 15(3):385–400, 2001.

M. Puddephat. Principles of Magnetic Resonance Imaging. Website, December 2002. URL `http://www.easymeasure.co.uk/principlesmri.aspx`.

P. Pulkkinen, J. Partanen, P. Jalovaara, and T. Jamsa. Combination of bone mineral density and upper femur geometry improves the prediction of hip fracture. *Osteoporosis International*, 15(4):274, 2004.

J. Reeve, J. M. Zanelli, N. Garrahan, J. N. Bradbeer, J. S. Wand, S. T. Moyes, J.-P. Roux, and T. Smith. Bone remodeling in hip fracture. *Calcified Tissue International*, 53(Supplement - 1):S108–S112, February 1993.

R. A. Robinson and S. R. Elliott. The water content of bone. *Journal of Bone and Joint Surgery*, 39:167–188, 1957.

F. J. Rohlf. Rotational fit (Procrustes) methods. In F. J. Rohlf and F. L. Bookstein, editors, *Proceedings of the Michigan Morphometrics Workshop*, number 2, University of Michigan, Museum of Zoology, 1990.

F. J. Rohlf and M. Corti. Use of two-block Partial Least-Squares to study covariation in shape. *Systematic Biology*, 49(4):740–753, dec 2000. ISSN 1063-5157.

F. J. Rohlf and L. F. Marcus. A revolution in morphometrics. *Trends in Ecology and Evolution*, 8:129–132, 1993.

M. Sabin, G. Blake, S. MacLaughlin-Black, and I. Fogelman. The accuracy of volumetric bone density measurements in dual x-ray absorptiometry. *Calcif Tissue Int.*, 56(3):210–4, 1995.

L. V. Safont and E. M. Marroqun. 3D Reconstruction of Third Proximal Femur (31-) with Active Contours. In *Proceedings of the 10th International Conference on Image Analysis and Processing*, 1999.

M. Sato, T. A. Grese, J. A. Dodge, H. U. Bryant, and C. H. Turner. Emerging therapies for the prevention or treatment of postmenopausal Osteoporosis. *Journal of Medical Chemistry*, 42(1):1–24, January 1999.

E. Seeman. The structural basis of bone fragility in men. *Bone*, 25:143–147(5), July 1999.

E. Seeman. Invited review: Pathogenesis of osteoporosis. *Journal of Applied Physiology*, 95(5):2142–2151, 2003.

M. J. Seibel. Biochemical markers of bone turnover part II: Clinical applications in the management of Osteoporosis. *The Clinical Biochemist Reviews*, 27(3): 123–38, Aug 2006.

R. S. Siffert, G. M. Luo, S. C. Cowin, and J. J. Kaufman. Dynamic relationships of trabecular bone density, architecture, and strength in a computational model of osteopenia. *Bone*, 18(2):197–206, February 1996.

D. E. Slice, F. L. Bookstein, L. F. Marcus, and F. J. Rohlf. *Advances in Morphometrics*, chapter Appendix I: A glossary for geometric morphometrics, pages 531–551. Plenum Press, 1996.

L. I. Smith. A tutorial on Principal Components Analysis. Website, 2002. URL `http://www.cs.otago.ac.nz/cosc453/student_tutorials/principal_components.pdf`.

M. Sramek and A. E. Kaufman. vxt: A class library for object voxelization. In *IEEE conference on Visualization*, pages 191–198, 1999.

M. R. Stytz, G. Frieder, and O. Frieder. Three-dimensional medical imaging: algorithms and computer systems. *ACM Comput. Surv.*, 23(4):421–499, 1991. ISSN 0360-0300.

G. Subsol, J.-P. Thirion, and N. Ayache. First steps towards automatic building of anatomical atlas. Technical report, Institut National de Recherche en Informatique et Automatique, 1994.

Y. Sun, I. Liu, and J. K. Grady. Reconstruction of 3D tree-like structures from three mutually orthogonal projections. *IEEE Transactions on Pattern Analysis and Machine Intelligence*, 16:241–248, 1994.

F. Taddei, S. Martelli, B. Reggiani, L. Cristofolini, and M. Viceconti. Finite-element modeling of bones from CT data: Sensitivity to geometry and material uncertainties. *IEEE Transactions on Biomedical Engineering*, 53(11):2194–2200, 2006.

T. S. Y. Tang and R. E. Ellis. 2D/3D deformable registration using a hybrid atlas. In *MICCAI (2)*, pages 223–230, 2005.

D. Testi, A. Cappello, F. Sgallari, M. Rumpf, and M. Viceconti. A new software for prediction of femoral neck fractures. *Computer Methods and Programs in Biomedicine*, 75:141–145, 2004.

D. W. Thompson. *On Growth and Form*. Cambridge [Eng.] : The University Press, 2nd edition, 1942.

F. Trochu. A contouring program based on dual kriging interpolation. *Engineering with Computers*, 9(3):160–177, Sept. 1993.

A. Vesterby. Star volume in bone research: A histomorphometric analysis of trabecular bone structure using vertical sections. *The Anatomical Record*, 235: 325–334, 1993.

K. A. Ward, D. K. Roy, S. R. Pye, T. W. O'Neill, J. L. Berry, C. M. Swarbrick, A. J. Silman, and A. J. E. Forearm bone geometry and mineral content in UK women of European and South-Asian origin. *Bone*, 41(1):117–21, 2007.

R. Wasnich, P. Ross, J. Davis, and J. Vogel. A comparison of single and multi-site BMC measurements for assessment of spine fracture probability. *Journal of Nuclear Medicine*, 30(7):1166–71, July 1989.

WHO Study Group. Assessment of fracture risk and its applications to screening for postmenopausal osteoporosis. WHO Technical Report Series 843, WHO, Geneva, 1994.

D. Wirtz, T. Pandorf, F. Portheine, K. Radermacher, N. Schiffers, A. Prescher, D. Weichert, and F. Niethard. Concept and development of an orthotropic FE model of the proximal femur. *Journal of Biomechanics*, 36(2):289–293, 2003.

H. Wold. *Research Papers in Statistics*, chapter Non-linear estimation by iterative least-squares procedures. Wiley, New York., 1966.

S. Wold, L. Eriksson, J. Trygg, and N. Kettaneh. The PLS method – partial least squares projections to latent structures – and its applications in industrial RDP (research, development, and production). In *Proceedings volume of CompStat 2004 conference*, Prague, Czech Republic, 2004.

S. Wold, N. Kettaneh-Wold, and B. Skagerberg. Nonlinear PLS modeling. *Chemometrics and Intelligent Laboratory Systems*, 7(1-2):53–65, Dec. 1989.

T. Yoshikawa, C. Turner, M. Peacock, C. Slemenda, C. Weaver, D. Teegarden, P. Markwardt, and D. Burr. Geometric structure of the femoral neck measured using dual-energy x-ray absorptiometry. *Journal of Bone & Mineral Research*, 9 (7):1053–64, July 1994.

M. L. Zelditch, D. L. Swiderski, H. D. Sheets, and W. L. Fink. *Geometric Morphometrics for Biologists - A Primer*. Elsevier Academic Press, 2004.

X. Zhao, F. Qi, H. Huang, and J. Zhan. 3-D Deformable models for femur shape recovery from volumetric images. In *Proceedings of the Fourth International Conference/Exhibition on High Performance Computing in Asia-Pacific Region*, 2000.

G. Zheng, M. Ballester, M. Styner, and L. Nolte. Reconstruction of patient-specific 3D bone surface from 2D calibrated fluoroscopic images and point distribution model. In *International Conference on Medical Image Computing and Computer-Assisted Intervention*, volume 9 of *1*, pages 25–32, 2006.

Publications

C. M. Langton, J. A. Thorpe, S. Pisharody, D. K. Langton, S. A. Steel, and S. Das. Discrimination of BMD-matched recent hip fracture subjects by FEXI. In *Proceedings of the ASBMR Bone Quality meeting*, Washington, USA, 2005a.

C. M. Langton, J. A. Thorpe, S. Pisharody, D. K. Langton, S. A. Steel, and S. Das. Discrimination of BMD-matched recent hip fracture subjects by FEXI. In *Proceedings of the Bone & Tooth Society Annual Meeting*, Birmingham, UK, 2005b.

S. Pisharody, P. S. Ganney, R. Phillips, and C. M. Langton. Extraction of femur contour from hip radiographs for osteoporotic fracture-risk prediction by FEXI. In *Proceedings of the IPEM Annual Scientific Meeting*, York, UK, Sep 6-8, 2004 2004a.

S. Pisharody, C. M. Langton, and R. Phillips. Sensitivity of proximal femoral stiffness and areal bone mineral density to changes in bone geometry and density. *Journal of Engineering in Medicine*, Accepted for publication.

S. Pisharody, R. Phillips, and C. Langton. 3D reconstruction from a single X-ray: In search of the missing dimension. In *Proceedings of the IPEM Annual Scientific Meeting*, Cardiff, UK, September 2007.

S. Pisharody, R. Phillips, J. A. Thorpe, and C. M. Langton. Sensitivity of FEXI to anatomical variations of the proximal femur - a simulation approach. In *Proceedings of the Tenth NOS Conference*, page S38, Harrogate, UK, Nov 29-Dec 1, 2004 2004b.

S. Pisharody, R. Phillips, J. A. Thorpe, and C. M. Langton. Sensitivity of FEXI to anatomical variations of the proximal femur - a simulation approach. In *Proceedings of the ASBMR Bone Quality meeting*, Washington, USA, 2005a.

S. Pisharody, R. Phillips, J. A. Thorpe, and C. M. Langton. Sensitivity of FEXI to anatomical variations of the proximal femur - a simulation approach. In *Proceedings of the Bone & Tooth Society Annual Meeting*, Birmingham, UK, 2005b.